

4. SITE 1072¹

Shipboard Scientific Party²

HOLE 1072A

Position: 39°21.9370'N, 72°41.6750'W
Start hole: 1400 hr, 29 June 1997
End hole: 1500 hr, 2 July 1997
Time on hole: 73 hr (3.04 days)
Seafloor (drill pipe measurement from rig floor, mbrf): 109.5
Total depth (drill pipe measurement from rig floor, mbrf): 416.3
Distance between rig floor and sea level (m): 11
Water depth (drill pipe measurement from sea level, m): 98.1
Penetration (mbsf): 306.8
Coring totals:
Type: RCB
Number: 56
Cored: 306.8 m
Recovered: 151.87 m (49.5%)

Lithology:

Unit I: 0–152.13 mbsf; Holocene(?), Pleistocene to Pliocene
Dark gray to greenish gray silty clay, clayey silt, and clay with thin interbeds of olive gray sandy mud, sandy silt, clayey sand, and muddy sand

Unit II: 152.13–274.38 mbsf; early Pliocene to late Miocene
Olive gray micaceous sandy silt, dark gray silty clay, dark gray micaceous muddy sand, and dark greenish gray glauconitic sandy silts and sandstones

HOLE 1072B

Position: 39°21.9305'N, 72°41.6647'W
Start hole: 2340 hr, 2 July 1997
End hole: 1610 hr, 5 July 1997
Time on hole: 64.5 hr (2.69 days)
Seafloor (drill pipe measurement from rig floor, mbrf): 109.5
Total depth (drill pipe measurement from rig floor, mbrf): 468.1
Distance between rig floor and sea level (m): 11.5
Water depth (drill pipe measurement from sea level, m): 98.0
Penetration (mbsf): 358.6
Coring totals:
Type: RCB
Number: 6
Cored: 51.8 m
Recovered: 0.03 m (0.05%)

HOLE 1072C

Position: 39°21.921'N, 72°41.644'W
Start hole: 2030 hr, 5 July 1997
End hole: 0335 hr, 6 July 1997
Time on hole: 7.08 hr
Seafloor (drill pipe measurement from rig floor, mbrf): 111
Total depth (drill pipe measurement from rig floor, mbrf): 217.9
Distance between rig floor and sea level (m): 11.5
Water depth (drill pipe measurement from sea level, m): 99.5
Penetration (mbsf): 106.9
Comments: Logging while drilling (LWD); no coring attempted.

HOLE 1072D

Position: 39°21.9256'N, 72°41.6523'W
Start hole: 1030 hr, 6 July 1997
End hole: 1825 hr, 7 July 1997
Time on hole: 31.92 hr (1.33 days)
Seafloor (drill pipe measurement from rig floor, mbrf): 111
Total depth (drill pipe measurement from rig floor, mbrf): 466.9
Distance between rig floor and sea level (m): 11.5
Water depth (drill pipe measurement from sea level, m): 99.5
Penetration (mbsf): 355.9
Comments: Logging while drilling (LWD); no coring attempted.

Principal results: Site 1072 is the second of two sites approved for *JOIDES Resolution* drilling on the New Jersey continental shelf; together with Site 1071, it forms part of a transect of holes from the slope (Ocean Drilling Program [ODP] Leg 150) to coastal outcrops (Legs 150X and 174AX) that constitute the Mid-Atlantic Sea-level Transect. The primary goals of the transect are to: (1) date sequence boundaries of Oligocene to Holocene age and compare this stratigraphic record with the timing of glacial-eustatic changes inferred from deep-sea $\delta^{18}\text{O}$ variations; (2) place constraints on the amplitudes and rates of sea-level change that may have been responsible for unconformity development; (3) assess the relationships between depositional facies and sequence architecture; and (4) provide a baseline for future scientific ocean drilling that will address the effects and timing of sea-level changes on this and other passive margins. Site 1072 is ~3.5 km seaward of Site 1071 and coincides with the rollover or breakpoint in sequence boundary m0.5(s). This site provides information primarily about upper Miocene and younger strata and permits a comparison, in the direction of progradation, with the succession at Site 1071.

As at Site 1071, the upper Miocene to Pleistocene succession is divisible into three unconformity-bounded sequences. The sequence boundaries are characterized by well-developed seismic offlap and are informally designated pp3(s), pp4(s), and m0.5(s). The “s” designation following the “pp” (provisionally Pliocene–Pleistocene) and “m” (provi-

¹Austin, J.A., Jr., Christie-Blick, N., Malone, M.J., et al., 1998. *Proc. ODP, Init. Repts.*, 174A: College Station, TX (Ocean Drilling Program).

²Shipboard Scientific Party is given in the list preceding the Table of Contents.

sionally Miocene) sequence boundary identifications is meant to distinguish the shelf sequence boundaries, targeted for sampling and logging by Leg 174A, from similarly labeled surfaces recognized on the slope by Leg 150 (Mountain, Miller, Blum, et al., 1994). Surface pp5(s), a seismic surface tentatively interpreted as a sequence boundary at the beginning of the leg, is now regarded as part of an interval of upward deepening and is clearly of late Miocene age, which is older than originally expected. Revised ages for the remaining sequence boundaries are as follows: pp3(s) = late Pleistocene (<0.78 Ma); pp4(s) = early Pleistocene to late Miocene (1.4–7.4 Ma), and most likely of Pliocene–Pleistocene age. Surface pp5(s) is dated as 5.9–7.4 Ma. Surface m0.5(s) is poorly constrained at Site 1072 as >5.9 Ma. Coring and logging suggest that the sandy lower intervals above sequence boundaries m0.5(s) and pp4(s) thin in a seaward direction. Each of these units is composite, including seismically imbricated intervals 10–25 m thick that shoal upward. Coarsening upward and possible shoaling (from benthic foraminifers) beneath surface pp4(s) are consistent with a larger scale transition from transgressive (dominant) to highstand (minor) sedimentation.

The sedimentologic column at Site 1072 is divided into two units on the basis of accessory components: glauconite, carbonate, and pyrite nodules. Unit I extends from 0 to 152.13 mbsf, and Unit II extends from 152.13 to 274.38 mbsf. These units are considered close genetic equivalents to Units I and II at Site 1071, and the contact between them corresponds approximately to surface pp4(s). Thick intervals of nonrecovery in both units and downhole logs suggest that sands are present in these sections. Unit I is characterized by intervals of dark gray to dark greenish gray silty clays, clayey silts, and clays interbedded with olive gray sandy mud, sandy silt, clayey sand, and/or muddy sand. Slumping/microfaulting is common at the top and bottom of the unit. Bioturbation is associated with intervals where clays are interbedded with coarser sediments. The lower boundary of the unit is rich in glauconite, shells, granules, and pebbles.

Glauconite is generally present toward the top of Unit II in olive gray sandy silts with scattered granules, shells, and wood fragments. Carbonate and pyrite nodules, wood fragments, and discrete burrows are associated with dark gray to olive gray silty clay from the middle to the base of Unit II. Cemented intervals of poorly sorted, glauconitic, pebbly, medium to coarse-grained quartz sandstone are present at the base of this unit.

Similar to Site 1071, biostratigraphic resolution at Site 1072 is limited for calcareous microfossils because of strong carbonate dissolution and shallow water depths that were unfavorable to these planktonic organisms. Nannofossils provide relatively useful zonations for the Pleistocene and early Pliocene to late Miocene. Planktonic foraminifers have limited use for biostratigraphic zonation at Site 1072, although it was possible to identify late Miocene, late Pliocene, and younger ages on the basis of the presence/absence of rare taxa.

Pleistocene benthic foraminiferal faunas vary from assemblages dominated almost exclusively by *Elphidium excavatum* to more diverse assemblages, probably reflecting changing paleodepths or substrates of diverse grain size, perhaps related to glacial/interglacial cycles. Benthic foraminiferal species abundances indicate that paleodepths were slightly deeper at Site 1072 than at Site 1071 during the Pleistocene, ranging from inner neritic (0–50 m) to upper middle neritic (~50–65 m) at Site 1072. Miocene biofacies are characterized by *Buliminella gracilis* and *Uvigerina juncea*, indicating middle neritic paleodepths (50–100 m).

Organic microfossils are common to abundant in most samples studied, particularly in pre-Pleistocene sediments. Dinocysts are relatively more abundant in pre-Pleistocene sediments as well, whereas terrestrial palynomorphs (pollen and spores) dominate Pleistocene sediments. Re-working is clearly evident in many samples. In addition, it is possible that some well-preserved organic microfossils are indistinguishable from in situ fossils. Stratigraphic discontinuity pp4(s) can be recognized in a condensed interval of Pliocene–early Pleistocene age.

Several magnetic polarity boundaries are recorded in sediments recovered from Hole 1072A. The Brunhes/Matuyama (B/M) boundary was found at 62.3 mbsf within a clayey silt (Subunit IC), which was confirmed by a calcareous nannofossil datum from Sample 174A-1072A-9R-CC (0.4–0.9 Ma). This boundary coincides with a marked increase both in

magnetization intensity and susceptibility downhole. This evidence suggests that the sedimentary environment, which supplied magnetic minerals, changed across the boundary, or that the boundary is instead a diagenetic front during the Brunhes Chron associated with the sedimentation above. For Subunit IC below the assumed B/M boundary, magnetic polarity is reversed down to pp4(s) (~141–155 mbsf), although a normal polarity zone is located at 141.8–144 mbsf. This normal polarity interval is associated with slump and sand layers and intervals of low recovery. Below pp4(s), within the upper silty clay layer of Subunit IIA, magnetic polarity is dominantly normal with thin reverse zones at 177–182 mbsf, 206–208 mbsf, and 215–218 mbsf. For the lower muddy sands of Subunit IIA, near surface pp5(s) (~225–249 mbsf), magnetic polarity is normal throughout; magnetization intensity and susceptibility in this interval become lower than in the overlying upper silty clay layer.

Downhole profiles of interstitial water at Site 1072 are complex, but somewhat similar to those at Site 1071. Pore waters are significantly fresher than seawater (Cl^- to 469 mM, a 16% decrease) at <150 mbsf. The salinity minimum is a nonequilibrium feature caused by oscillations in the salinity of overlying water, perhaps a proxy for the rise and fall of sea level. Freshwater has access to the sediment column during presumed glacial stages, whereas seawater covers the sediment column during interglacial stages. The salinity minimum at Site 1072 is less pronounced and ~30 m deeper than the minimum at Site 1071. These differences may reflect an elevation offset between the two locations during the last transgression.

Decreases in sulfate, with corresponding increases in alkalinity, ammonia, and phosphate, occur at two distinct intervals of the sediment column: at 30 mbsf near the shallow salinity minimum and below 150 mbsf. Upper and lower zones of significant organic-matter diagenesis were also observed at similar depths at Site 1071. However, changes in pore-water concentrations are more pronounced at Site 1072, suggesting higher overall rates of organic-matter diagenesis there. In particular, sulfate drops to ~1 mM in the upper zone at Site 1072, but only to ~6 mM at Site 1071.

Hydrocarbon gases were monitored by headspace sampling for every core recovered at Site 1072. As at Site 1071, hydrocarbon gases generally are at or near detection limit (methane < 5 parts per million by volume [ppmv]). Exceptions are three samples near 30 mbsf, where methane (C_1) rises to 1056 ppmv. The presence of C_1 at a depth where interstitial water sulfate approaches zero suggests a thin zone of bacterial methanogenesis at Site 1072, unlike at Site 1071.

A comprehensive set of physical properties measurements was acquired on cores from Hole 1072A, with the exception that the *P*-wave logger (PWL) component of the multisensor track (MST) was not employed because of the presence of incompletely filled core liners. The natural gamma-ray (NGR) component of the MST reached a local maximum at 57.1 mbsf; this maximum is located immediately above the boundary between lithostratigraphic Subunits IA/IB and IC and is at the approximate level of sequence boundary pp3(s) (49–53 mbsf). The overall maximum NGR value is at 151.6 mbsf; this depth is immediately above the boundary between lithostratigraphic Subunits IC and IIA and is within the inferred depth range of sequence boundary pp4(s). In recovered intervals, the overall shape of the NGR curve obtained from physical properties measurements is in good agreement with that derived from logging. Index properties measurements were obtained at ~75-cm spacing in recovered cores. Wet bulk-density values for Hole 1072A average 2.00–2.10 g/cm³, with little variation. The maximum values in wet-bulk density are found just above the boundary between lithostratigraphic Subunits IC and IIA (147–151 mbsf; near pp4[s]) and from the well-cemented sandstone recovered at 268.79 mbsf. The shape of the physical properties wet bulk-density curve is in good agreement with that obtained from logging in Hole 1072D, although logging-derived values are consistently somewhat higher. Discrete *P*-wave velocity measurements, taken transverse to the core axis, were made with the same frequency as index properties. Velocities are generally between 1600 and 1800 m/s, with exceptions noted below. Velocities >5000 m/s are associated with well-cemented sandstones recovered at 165.35 and 268.79 mbsf. Other high-velocity intervals (>2000 m/s) are located at ~36.6 mbsf and between ~147 and 151 mbsf; the latter interval corresponds approximately to the lithostratigraphic Subunit IC/IIA boundary and is within the inferred depth range of pp4(s). In

addition, this higher velocity interval appears to be of sufficient thickness and density contrast to be seismically resolvable. Conversely, the highest-velocity intervals associated with recovered indurated sandstones may be too thin to be seismically resolvable. Resistivity measurements were taken at least once per recovered section; trends in physical properties and logging resistivity data are consistent overall, although physical properties resistivity values are on average ~20%–25% lower. The highest resistivity value measured in recovered cores was 3.23 Ωm at 147.54 mbsf; this is just above the Subunit IC/IIA [pp4(s)] lithostratigraphic/sequence boundary. Other measurements were made, including porosity, shear strength, thermal conductivity, and magnetic susceptibility. Physical properties data appear to be consistent with logging data and will prove useful in refining velocity models for seismic data in the vicinity of Sites 1071 and 1072.

Hole 1072A was logged almost to total depth (TD; 300 mbsf) with the triple combo logging string (dual induction resistivity, neutron porosity, and density tools), plus the spectral gamma-ray and the LDEO temperature tools. Log data are of good quality, except for washed-out intervals near the bottom of the hole. A repeat run from 110 mbsf to the bottom of the drill pipe (61 mbsf) confirmed the log responses of the main run. The pipe became stuck while rigging down; this forced the severing of the pipe and continuation of logging in Hole 1072B.

Hole 1072B was washed to 306.8 mbsf and logged in four wireline runs. The first run was an induction-sonic string (measuring resistivity and sound velocity, with a spectral gamma-ray tool for correlation to other log runs) that failed to pass a bridge at ~90 mbsf. The tool string was pulled out, the hole was reamed, and a repeat run was made with the long-spaced sonic tool (LSS) in place of the sonic digital tool (SDT). Despite difficulties in passing several bridges on the way down, a successful run was logged from TD up to the pipe at 43 mbsf. Good velocity data were collected, with cycle skipping observed only in two thin intervals of rapid velocity changes corresponding to indurated sandstone. Overall, the LSS tool, despite its lack of a receiver array, performed better than the SDT in the variable diameter, sandy conditions found in Hole 1072B. The third wireline run, from ~307 to 50 mbsf, utilized the Formation MicroScanner-sonic (FMS-sonic) tool. Roughly 20% of the hole was washed out beyond the maximum opening of the caliper, but images of the remaining 80% provided good detail of bedding features in intervals of poor core recovery. The final logging operation was a vertical seismic profile (VSP) using the well seismic tool (WST) tool. These data provide interval velocities that compare well with the shipboard *P*-wave measurements on discrete samples from Hole 1072A and yield a time-depth conversion that give seismic-core-log correlations a high degree of precision.

Hole 1072B demonstrated the ability to drill these sand-prone formations, and LWD was conducted in Holes 1072C and 1072D to ~100 and ~356 mbsf, respectively. Measurements included resistivity, spectral gamma ray (SGR), porosity, density, and photoelectric effect (PEF). In addition, borehole diameter was statistically derived from the density measurements. Log data were recorded in the upper 100 mbsf of both holes, providing replicate measurements and thus quality control for these sets of data.

A preliminary integration of logs and core data has been useful, both in assessing the character of unrecovered intervals and for calibrating the log measurements. Log data quality are generally good to excellent, except where sand-rich, washed-out intervals are encountered. These unconsolidated, sand-rich layers correlate to zones of low resistivity, velocity, and gamma-ray values. Intermediate resistivity, velocity, and gamma-ray data correspond to silty intervals; clay-rich intervals show high resistivity, velocity, and gamma-ray values. The SGR, as well as the PEF, identify high glauconite concentrations in the upper ~155 m (Pliocene–Pleistocene). Of particular note is an incompletely recovered, glauconite-rich sand that logs show has variable thickness in each of the three holes in which it was penetrated (149.5–157 mbsf in Hole 1072A; 149.5–151.4 mbsf in Hole 1072B; 149–155 mbsf in Hole 1072D). These holes were a total of ~40 m apart; the glauconite sand appears to rest directly on, or a few meters above, a regionally significant offlap surface (pp4[s]). Two intervals of well-cemented glauconitic quartz sandstone can be detected by especially high resistivity, density, and velocity; one is at the offlap sur-

face near 150 mbsf, and the other is at 275–278 mbsf. Throughout most of Hole 1072B, FMS-sonic images delineate bed boundaries and internal structures such as slumping. High, as well as low, resistivity spots in these images indicate various kinds of nodules, clasts, and burrows.

BACKGROUND AND OBJECTIVES

Site 1072 is the second of two sites on the outer continental shelf of the New Jersey margin that were chosen specifically for the interpretation and dating of surface m1(s). Site 1072 was located down dip from Site 1071 at the approximate toe-of-clinoform position for surface m1(s). The site also intersects sequence boundary m0.5(s) close to its rollover/breakpoint, and therefore occupies a position with respect to m0.5(s) analogous to the relation between Site 1071 and the m1(s) rollover/breakpoint (see “Seismic Stratigraphy” section, this chapter). Site 1072 is located at the intersection of *Oceanus* 270 MCS Profiles 147 and 908, at a water depth of 98 m ~3.5 km (1.9 nmi) southeast of Holes 1071A–1071E and 2.6 km (1.4 nmi) southeast of Holes 1071F and 1071G. The geological context of this site, and a description of geophysical data supporting its selection, are described in the “Introduction” chapter (this volume).

Coring and logging at Site 1072 were undertaken after completion of operations at Holes 1071A–1071C, but before a renewed attempt to core and log Holes 1071D–1071G (see “Site 1071” chapter, this volume). Initial work at Site 1071 confirmed the interpretation of surfaces pp3(s) and pp4(s) as sequence boundaries and placed broad constraints on their ages. A surface below pp4(s), initially interpreted as a sequence boundary on the basis of apparent onlap and informally named pp5(s), was reinterpreted as a flooding surface. Hole stability problems at Site 1071 at first prevented penetration below surface m0.5(s), as well as both wireline logging and logging while drilling. A priority at Site 1072 was therefore to attempt to core and log to a deeper stratigraphic level.

The primary goals of Site 1072 are (1) to sample sequence boundaries where they have been traced to a more seaward position to evaluate ideas about how facies are related to sequence geometry; (2) to improve the calibration of sequence boundaries, mainly m1(s) and deeper; and (3) to place constraints on amplitudes and rates of sea-level change that may have been responsible for unconformity development.

OPERATIONS

Hole 1072A

The ship was moved in dynamic positioning (DP) mode 1.9 nmi along the trend of site-specific seismic lines bearing ~125° from Site 1071, Holes 1071A–1071E, to the dGPS coordinates for proposed site MAT-9B1 (Fig. 1). Observations of the tethered beacon vs. the beacon held upright in a stand at Site 1071 suggested that the beacon signal problem was related to beacon offset distance and not current disturbance of beacon attitude. Tethers 2 m long were used again because they were successful at Site 1071; historically, shorter tethers have caused the beacons to collide with the anchoring weights on impact. The ship was positioned with the moonpool over Hole 1072A for both beacon drops. The first beacon (15.0 kHz) was dropped at 0723 hr on 29 June and moved 10 m at 161° before settling. A second beacon (17.0 kHz) was dropped at 0750 hr on 29 June and moved 23 m at 187°. The single working dGPS unit aboard ship was more stable than regular GPS; nevertheless, it experienced periods when it drifted despite efforts to stabilize it. Shore-based assistance was sought to get the other dGPS unit to work. The occasional drift in dGPS (± 4 m) may have made the beacon drift appear larger than it actually was. A TV and sonar survey was conducted on a 6-m square pattern centered on the site coordinates, with no bottom obstructions observed. One of the beacons experienced a signal loss when the first hole was spudded (~3 m away), and periodically thereafter during

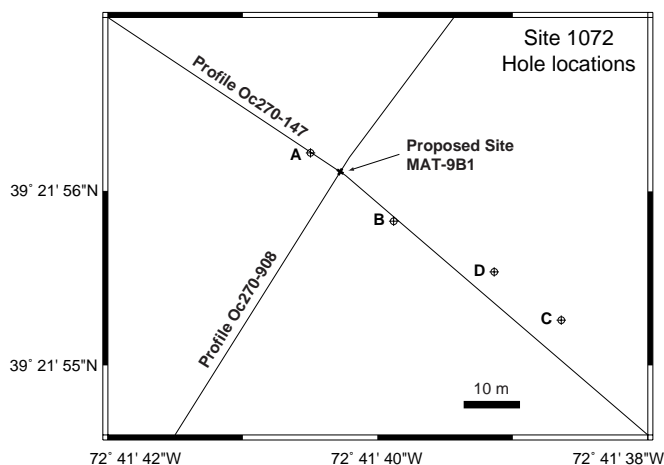


Figure 1. Locations of Holes 1072A–1072D with respect to originally proposed site location MAT-9B1 and site survey seismic data (Cruise Oc270, Profiles 147 and 908; see “Seismic Stratigraphy” section, this chapter).

wireline operations; this suggested that, ideally, beacons should be offset ~7 m from the hole to avoid such acoustic interference.

The rotary core barrel (RCB) coring system was selected over advanced hydraulic piston corer (APC)/extended core barrel (XCB) to determine if the anticipated increase in rate of penetration (ROP) and the smaller RCB bit diameter might produce both a more stable hole and achieve better recovery than at Site 1071. The seafloor was tagged at 98.1 mbsl (109.5 mbrf), and Hole 1072A was spudded at 1400 hr on 29 June (Table 1). RCB Cores 174A–1072A-1R through 51R were recovered from 0 to 282.8 mbsf. Half-cores (5-m advances) were taken with the intent of improving recovery. Mud sweeps were required to keep the hole clean after nearly every core (and sometimes every half core) over the entire interval; 920 bbl of sepiolite mud were used in Hole 1072A (four times normal usage). After Core 51R, increasing pump pressures and torque indicated possible hole sloughing, but mud sweeps cleared the hole. Coring continued with RCB Cores 174A-1072A-52R through 55R from 282.8 to 301.8 mbsf. Again, torque and pressure indicated continuing hole problems; therefore, a wiper trip was made to 229.6 mbsf. Core 56R was recovered from 301.8 to 306.8 mbsf; hole problems persisted despite additional mud sweeps.

Another wiper trip was made to 214 mbsf, and the hole was displaced with sepiolite mud in an effort to stabilize the sands for logging. The pipe was pulled up to the ship with heavy backflow to 91 mbsf. The seafloor was then surveyed with the VIT-TV and sonar; a 4-m diameter, slightly irregular crater at the seafloor was observed. The closer beacon was noted to be on the edge of this crater. The hole appeared to be backflowing water and sand, possibly from being overpressured during drilling (see “Operations” section, “Site 1071” chapter, this volume). A wiper trip was made to 296 mbsf, and 20 m of fill was tagged at the bottom of the hole. The hole was displaced with sepiolite mud again, and the RCB bit was pulled up to the ship to prepare for logging.

The open hole was reentered with sonar because the crater was obscured by what appeared to be flowing sand and water. The bit was stopped at 63 mbsf for logging. The triple combo string (density-positivity-resistivity) was run to 300 mbsf (9 m off bottom) in 2.75 hr. While preparing for the next logging run, the drill pipe began to stand up out of the elevators, indicating that the pipe was stuck. An unsuccessful effort was made to free the pipe by working it in gradually increasing increments from 20 to 200,000 lb overpull, and by circulating through the hose at pump pressures from 500 to 2500 psi at 300–1000 gpm; it was not possible to pick up the top drive or break the connection. A string shot was fired below the bit in hopes that the sand bridge could be knocked loose; however, the pipe remained

Table 1. Site 1072 coring summary.

Core	Date (1997)	Time (EST)	Depth (mbsf)	Length cored (m)	Length recovered (m)	Recovery (%)
174A-1072A-						
1R	29 June	1515	0-7.5	7.5	2.27	30.3
2R	29 June	1610	7.5-17	9.5	2.14	22.5
3R	29 June	1645	17-26.7	9.7	2.65	27.3
4R	29 June	1815	26.7-36.3	9.6	4.16	43.3
5R	29 June	1910	36.3-46	9.7	0.88	9.1
6R	29 June	2005	46-51	5.0	0.13	2.6
7R	29 June	2045	51-56	5.0	2.32	46.4
8R	29 June	2120	56-61	5.0	1.84	36.8
9R	29 June	2145	61-65.7	4.7	4.08	86.8
10R	29 June	2210	65.7-70.7	5.0	4.60	92.0
11R	29 June	2245	70.7-75.2	4.5	0.50	11.1
12R	29 June	2310	75.2-80.2	5.0	0.03	0.6
13R	29 June	2335	80.2-84.7	4.5	0.00	0.0
14R	29 June	2355	84.7-89.7	5.0	0.03	0.6
15R	30 June	0035	89.7-94	4.3	0.91	21.2
16R	30 June	0115	94-99	5.0	1.22	24.4
17R	30 June	0205	99-103.4	4.4	3.03	68.9
18R	30 June	0300	103.4-108.4	5.0	2.01	40.2
19R	30 June	0333	108.4-112.9	4.5	3.98	88.4
20R	30 June	0435	112.9-122.4	9.5	3.98	41.9
21R	30 June	0515	122.4-127.4	5.0	3.73	74.6
22R	30 June	0550	127.4-131.9	4.5	3.48	77.3
23R	30 June	0635	131.9-136.9	5.0	3.60	72.0
24R	30 June	0717	136.9-141.3	4.4	2.57	58.4
25R	30 June	0800	141.3-146.3	5.0	4.11	82.2
26R	30 June	0840	146.3-150.9	4.6	1.40	30.4
27R	30 June	1012	150.9-155.9	5.0	1.23	24.6
28R	30 June	1046	155.9-160.3	4.4	0.08	1.8
29R	30 June	1130	160.3-165.3	5.0	2.92	58.4
30R	30 June	1205	165.3-169.8	4.5	0.14	3.1
31R	30 June	1245	169.8-174.8	5.0	5.03	100.6
32R	30 June	1310	174.8-179.3	4.5	3.57	79.3
33R	30 June	1340	179.3-184.3	5.0	5.69	113.8
34R	30 June	1405	184.3-188.6	4.3	4.37	101.6
35R	30 June	1435	188.6-193.6	5.0	5.49	109.8
36R	30 June	1510	193.6-197.9	4.3	4.02	93.5
37R	30 June	1540	197.9-202.9	5.0	5.54	110.8
38R	30 June	1610	202.9-207.3	4.4	4.28	97.3
39R	30 June	1640	207.3-212.3	5.0	6.60	132.0
40R	30 June	1705	212.3-216.7	4.4	3.70	84.1
41R	30 June	1740	216.7-221.7	5.0	5.88	117.6
42R	30 June	1815	221.7-226.1	4.4	4.81	109.3
43R	30 June	1840	226.1-231.1	5.0	5.24	104.8
44R	30 June	1905	231.1-235.5	4.4	4.47	101.6
45R	30 June	1930	235.5-244.7	9.2	9.00	97.8
46R	30 June	1955	244.7-254.2	9.5	8.36	88.0
47R	30 June	2020	254.2-263.7	9.5	0.55	5.8
48R	30 June	2100	263.7-268.7	5.0	0.15	3.0
49R	30 June	2130	268.7-273.3	4.6	0.10	2.2
50R	30 June	2225	273.3-278.3	5.0	1.08	20.0
51R	01 July	0117	278.3-282.8	4.5	0.00	0.0
52R	01 July	0204	282.8-287.8	5.0	0.00	0.0
53R	01 July	0245	287.8-292.2	4.4	0.00	0.0
54R	01 July	0325	292.2-297.2	5.0	0.00	0.0
55R	01 July	0405	297.2-301.8	4.6	0.00	0.0
56R	01 July	0710	301.8-306.8	5.0	0.00	0.0
Coring totals:				306.8	151.87	49.50
174A-1072B-						
*****Drilled from 0.0 to 306.8 mbsf*****						
1R	05 July	0620	306.8-311.7	4.9	0.00	0.0
2R	05 July	0720	311.7-321.0	9.3	0.00	0.0
3R	05 July	0805	321.0-330.4	9.4	0.03	0.3
4R	05 July	0857	330.4-339.7	9.3	0.00	0.0
5R	05 July	0945	339.7-349.1	9.4	0.00	0.0
6R	05 July	1035	349.1-358.6	9.5	0.00	0.0
Coring totals:				51.8	0.03	0.05
Drilled:				306.8		
Total:				358.6		
174A-1072C-						
*****Drilled from 0.0 to 106.9 mbsf*****						
Total:				106.9		
174A-1072D-						
*****Drilled from 0.0 to 355.9 mbsf*****						
Total:				355.9		

Notes: An expanded version of this coring summary table that includes lengths and depths of sections, location of whole-round samples, and comments on sample disturbance is included on the CD-ROM in the back pocket of this volume. EST = U.S. Eastern Standard Time.

stuck. Therefore, the pipe was severed with an explosive charge at the top of the tapered drill collar at 23.5 mbsf and was pulled free with 100,000 lb overpull. The pipe cleared the rotary table at 1500 hr on 2 July, ending Hole 1072A.

Hole 1072B

Subsequent discussions concluded that hole instability within sandy intervals in Hole 1072A was aggravated by time spent coring and circulating. The conclusion was that a smaller, dedicated logging hole could be drilled and logged quickly, thereby maintaining better hole conditions. Therefore, the ship was moved in DP mode ~20 m southeast along a seismic line bearing 125° from Hole 1072A (Fig. 1). Observations of the beacon farther from Hole 1072A proved that the signal was not adequate for positioning at the new hole; therefore, the beacon was released and recovered. The ship was positioned with the moonpool over the intended spud point, and a new beacon (15.0 kHz, 193 dB) was dropped at 1530 hr on 2 July. However, the beacon moved 10 m at 304°, apparently because of current. The initial operational plan was to drill a LWD hole to 300 mbsf, and possibly also run wireline logs in the same hole; however, a decision was made to drill the hole for wireline logs first, then further evaluate formation stability before attempting a LWD run. Hole 1072B was spudded at 2340 hr on 2 July and drilled to 306.8 mbsf at 20.1 m/hr with sepiolite mud sweeps every other connection (19 m) (Table 1). A wiper trip was made to 71 mbsf, with 10,000 lb maximum overpull and drag, flow-back pressure to 90 mbsf, and 10-m fill. A second wiper trip was made to 250 mbsf, and the hole was filled with sepiolite again.

The persistent hole problems may have been caused by weak and unstable silty sands at 30–40 mbsf, which sloughed and enlarged the hole diameter, and/or unconsolidated, permeable intervals that resulted in lost circulation. Both effects eventually result in reduced annular fluid velocity, which might have caused cuttings to collect in the upper hole rather than to circulate out to the seafloor. These cuttings could have eventually formed a bridge, impeded vertical flow, increased annular pressure (and lost circulation), and packed off the hole, causing the pipe to stick.

The seafloor was surveyed with the VIT-TV and sonar on the trip for the logging bit. The open hole was obscured by a boiling cloud (suggesting possible flow-back from drilling operations), but it was reentered in 1 hr using sonar. The bit was positioned at 45 mbsf, because lateral motion there would be confined by unusually stiff clays near the seafloor. The sonic-resistivity tool string was run, but it would not pass 90 mbsf. A wiper trip was made from 30 to 102 mbsf with circulation and light reaming. The hole was displaced with sepiolite mud, and the pipe was positioned again at 45 mbsf. The sonic-resistivity and FMS tool strings were run successfully to 295.5 mbsf (11.3 m off bottom) in 4 hr. A VSP was run to the same depth with the WST in 3 hr. The reentry/logging bit cleared the rotary at 2100 hr on 4 July.

The RCB bottom-hole assembly (BHA) was rerun, and Hole 1072B was reentered. The bit took weight at 17 mbsf, indicating persistent closure of the upper hole from 20 to 60 mbsf. The hole was reamed through five tight spots and 8.5-m fill to 306.8 mbsf (previous TD). RCB Cores 174A-1072B-1R through 6R were cut from 306.8 to 358.6 mbsf (Table 1); however, coring was terminated after penetrating nearly 100 m of presumed unconsolidated sand with negligible recovery. Continued penetration of these sands could have endangered another BHA without any significant scientific return, so it was judged prudent by all parties to cease operations. The pipe was pulled at 1610 hr on 5 July, ending Hole 1072B.

Hole 1072C

The successful drilling and logging operations conducted in Hole 1072B indicated that a nearly identical hole could safely be drilled using LWD tools. The ship was moved ~30 m at 125° heading from

Hole 1072B to assure the best possible hole conditions and to avoid any disturbance from lost circulation at the previously drilled holes. A beacon (15.0 kHz, 193 dB) was deployed through the moonpool at 1650 hr on 5 July, which moved 4.3 m at 310°. Another beacon (15.0 kHz, 193 dB) was deployed through the moonpool at 1700 hr and moved 21 m at 265°. The ship was moved another ~5 m at 125° heading to maintain offset distance from the first beacon (Fig. 1).

The initial LWD plan called for drilling to 125 mbsf without the jars (to avoid flexing the jars above the seafloor), pulling out of the hole and picking up the jars, and then reentering and wiping through the upper hole before continuing. The bit tagged bottom at 99.5 mbsl (111.0 mbrf), and Hole 1072C was spudded at 2030 hr on 5 July and drilled to 106.9 mbsf in 6 hr (Table 1). The ROP was controlled to 25 m/hr to optimize LWD data collection. The bit was pulled above the seafloor to add the jars; an overpull of 30,000 lb up to 91 mbsf and 10,000 lb up to 29 mbsf was noted, indicating that the upper hole was closing in or packing off. The jars were added to the BHA, and the VIT was deployed for reentry; however, an electrical short was noted in the TV cable. The VIT repair was estimated to take 18 hr; therefore, a decision was made to continue LWD logging, either with a blind reentry into Hole 1072C or by spudding a new hole. The seafloor crater for Hole 1072C was located by offsetting the ship a few feet and feeling for bottom with the bit, but efforts to make a blind reentry were not successful. Hole 1072C officially ended at 0335 hr on 6 July when the bit cleared the seafloor.

Hole 1072D

The ship was moved ~15 m at a heading of 305° from Hole 1072C, back toward Hole 1072B (Fig. 1). The LWD BHA was reconfigured by taking out two drill collars, so the jars could be run at spud-in; no reentry was required. The seafloor was tagged at 99.5 mbsl (111.0 mbrf), and Hole 1072D was spudded at 1030 hr on 6 July (Table 1). The LWD hole was drilled from 0 to 110.4 m. Previous hole problems dictated that extra precautions be taken with the LWD tools, jars, and BHA. Soft clays from 0 to 30 mbsf had been squeezing into the annulus and packing off previous holes; therefore, a precautionary wiper trip was made with the top drive to 32.8 mbsf, and the BHA was run back to bottom with 10,000 lb maximum drag and 4 m of fill. Drilling continued in the LWD hole from 110.4 to 233.4 mbsf. A second precautionary wiper trip was made with the top drive to 32.8 mbsf with 10,000 lb maximum overpull, and the BHA was run back to bottom with 5000-lb maximum drag and 18 m of fill. Drilling continued in the LWD hole from 233.4 to 355.9 mbsf. The LWD BHA was pulled and successfully cleared the rotary at 1825 hr on 7 July, officially ending Hole 1072D and Site 1072.

LITHOSTRATIGRAPHY

Introduction

A primary goal of drilling at Site 1072 was to sample the upper middle Miocene sequence boundary m1(s) seaward of Site 1071, at a location that penetrated the toes of the set of clinofolds directly beneath m1(s). Secondary objectives were to sample updip, condensed, shallow-water portions of younger sequences and downdip, deeper water portions of older sequences (see “Introduction” chapter, this volume, and “Background and Objectives” section, this chapter). As was the case at Site 1071 (Holes 1071A–1071E), operational problems caused by unconsolidated sands prevented drilling to the m1(s) target depths, and only Pleistocene through upper Miocene sediments were recovered.

The sedimentologic column at Site 1072 is divided into two units on the basis of accessory components: glauconite, carbonate, and pyrite nodules (Figs. 2, 3; Table 2). These units are considered close genetic equivalents to Units I and II at Site 1071, although subunit delineation differs between Sites 1071 and 1072. Subunit IC is recog-

nized at both sites. However, unlike at Site 1071, the overlying sediments at Site 1072 cannot be easily differentiated into Subunits IA and IB; therefore, this interval is referred to as Subunit IA/IB. Subunit IIA at Site 1072 is considerably thicker than Subunit IIA at Site 1071. At both sites, the cored successions apparently contain Subunit IIB, but drilling at Site 1072 did not recover, and perhaps did not encounter, Subunit IIC.

Description of Lithologic Units

Unit I

Interval: 174A-1072A-1R-1, 0 cm, to 27R-CC, 5 cm
 Depth: 0–152.13 mbsf
 Age: Holocene (?), Pleistocene, possibly through early Pliocene (?)

Subunit IA/IB

Interval: 174A-1072A-1R-1, 0 cm, to 8R-1, 150 cm
 Depth: 0–57.50 mbsf

Core recovery near the top of Hole 1072A was relatively poor (~28%; Figs. 2, 3). Only eight intervals of muddy sediment, each <4 m thick, were recovered in the upper 57.84 m of the hole. The intervening unrecovered intervals are presumed to be composed of sand, on the basis of geophysical log evidence from Site 1072 (see “Downhole Logging” section, this chapter). Subunit IA/IB consists roughly of seven mud-sand intervals. Recovered sediments are dominated by silty clays and clays containing scattered bivalve fragments and very rare pebbles. At some levels, these clays are thinly interbedded with olive gray sandy mud, sandy silt, clayey sand, and/or muddy sand (i.e., intervals 174A-1072A-5R-1, 0 cm, to 5R-CC, 5 cm; and 174A-1072A-8R-1, 0 cm, to 8R-CC, 34 cm). Silty clays are typically dark gray to dark greenish gray, but range to black near the top of the hole (interval 174A-1072A-1R-2, 0–63 cm) because of hydrotroilite staining. Dark reddish gray silty clay is present in interval 174A-1072A-7R-1, 0 cm, to 7R-CC, 17 cm. Deformed sediments (e.g., Fig. 4) with inclined beds and/or thin laminae are present locally in intervals 174A-1072A-1R-2, 5–18 cm, 4R-1, 23–25 cm, 4R-1, 105–150 cm, 5R-1, 14–21 cm, and 8R-1, 69–113 cm, and are interpreted as slumps. However, recovered sediments are generally homogeneous, which presumably reflects complete bioturbation. Discrete, but unidentified burrows, are restricted to intervals in which clays are interbedded with coarser sediments. The apparent absence of discrete burrows in silty clays on the whole may be related to original substrate soupliness, which could have precluded formation of discrete burrows, and/or lack of textural or compositional contrast between burrow fills and surrounding sediment. The base of Subunit IA/IB is close to seismic surface pp3(s) (Fig. 3B; see “Seismic Stratigraphy” and “Summary and Conclusions” sections, this chapter).

Subunit IC

Interval: 174A-1072A-8R-1, 150 cm, to 27R-CC, 5 cm
 Depth: 57.50–152.13 mbsf

Subunit IC is characterized by poor core recovery (37%) and is represented by 16 cored intervals of variable thickness (Figs. 2, 3). The top three intervals in the subunit are referred to as Subunit IC₁ (interval 174A-1072A-8R-1, 150 cm, to 11R-CC, 8 cm) and are dominated by greenish gray, pyritic clayey silt (intervals 174A-1072A-9R-1, 0 cm, to 9R-CC, 8 cm; and 10R-1, 0 cm, to 10R-CC, 8 cm) and, less commonly, silty clay (interval 174A-1072A-11R-1, 0 cm, to 11R-CC, 8 cm). Log data suggest that these muds are separated by sandier units (unrecovered intervals). The clayey silt and silty clay of interval 174A-1072A-10R-2, 0–150 cm, exhibit deformation and microfaults indicative of slumping. Sediments of IC₁ appear to be completely bioturbated, and ichnofabrics are dominated by diffuse burrow mottling, although discrete burrows, including structures allied with *Chondrites*, small *Planolites*, *Palaeophycus*, *Zoophycos*(?), and

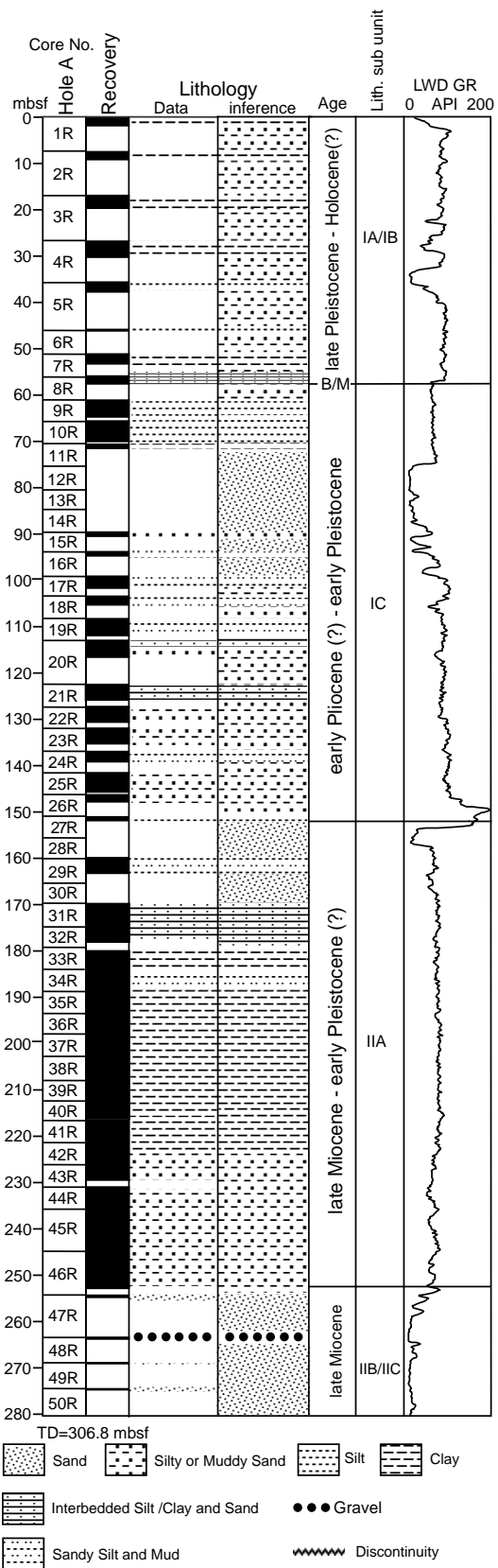


Figure 2. Generalized summary for Hole 1072A showing core recovery, lithology, age, and lithologic subunits. The columns show the lithology on the basis of recovered cores (data) and for intervals of nonrecovery (inference), on the basis of geophysical evidence from logs from Site 1072 (see “Downhole Logging” section, this chapter). B/M = Brunhes/Matuyama boundary. No core was recovered in the interval below 274.38 mbsf. LWD natural gamma-ray (LWD GR) data are from Hole 1072D.

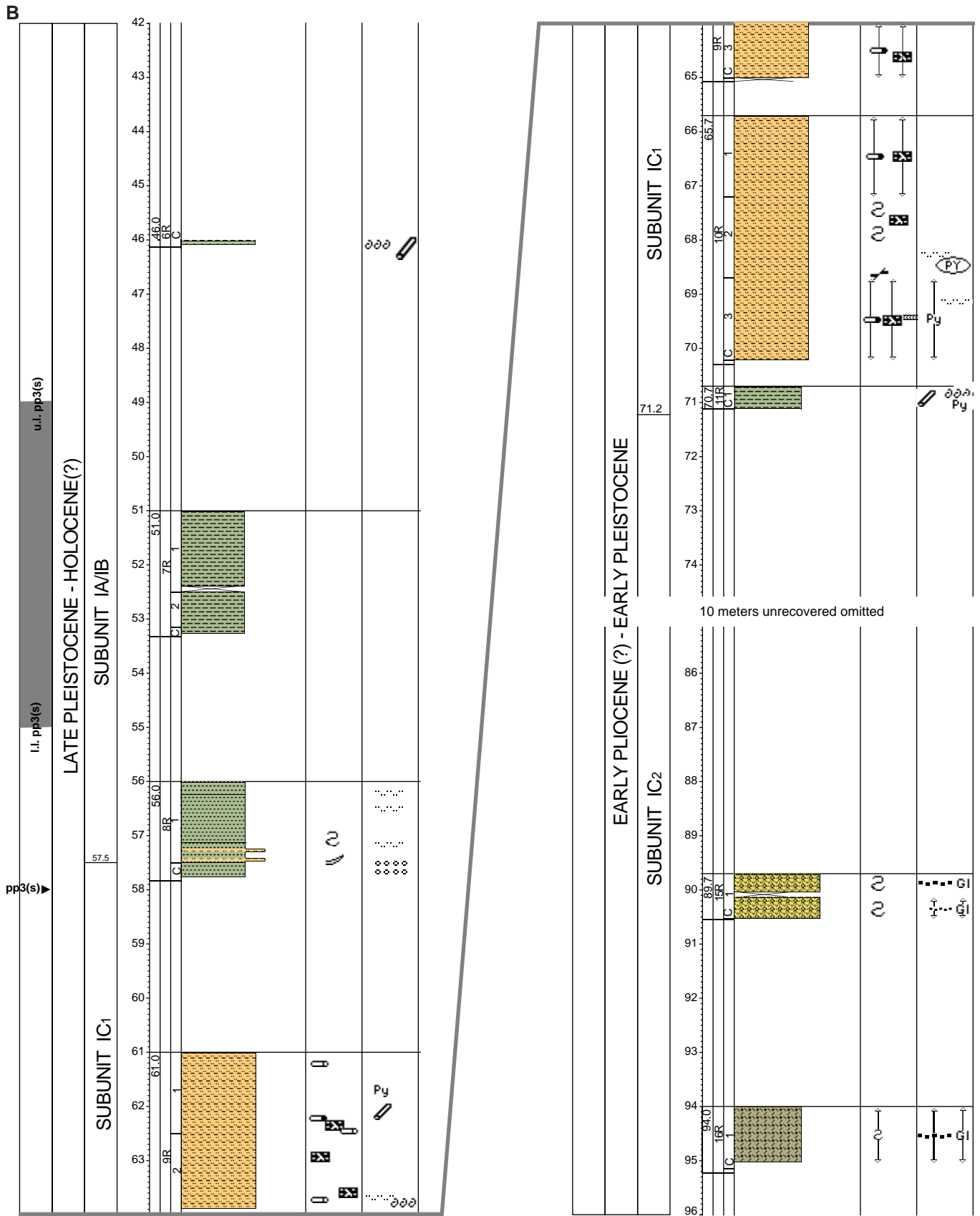
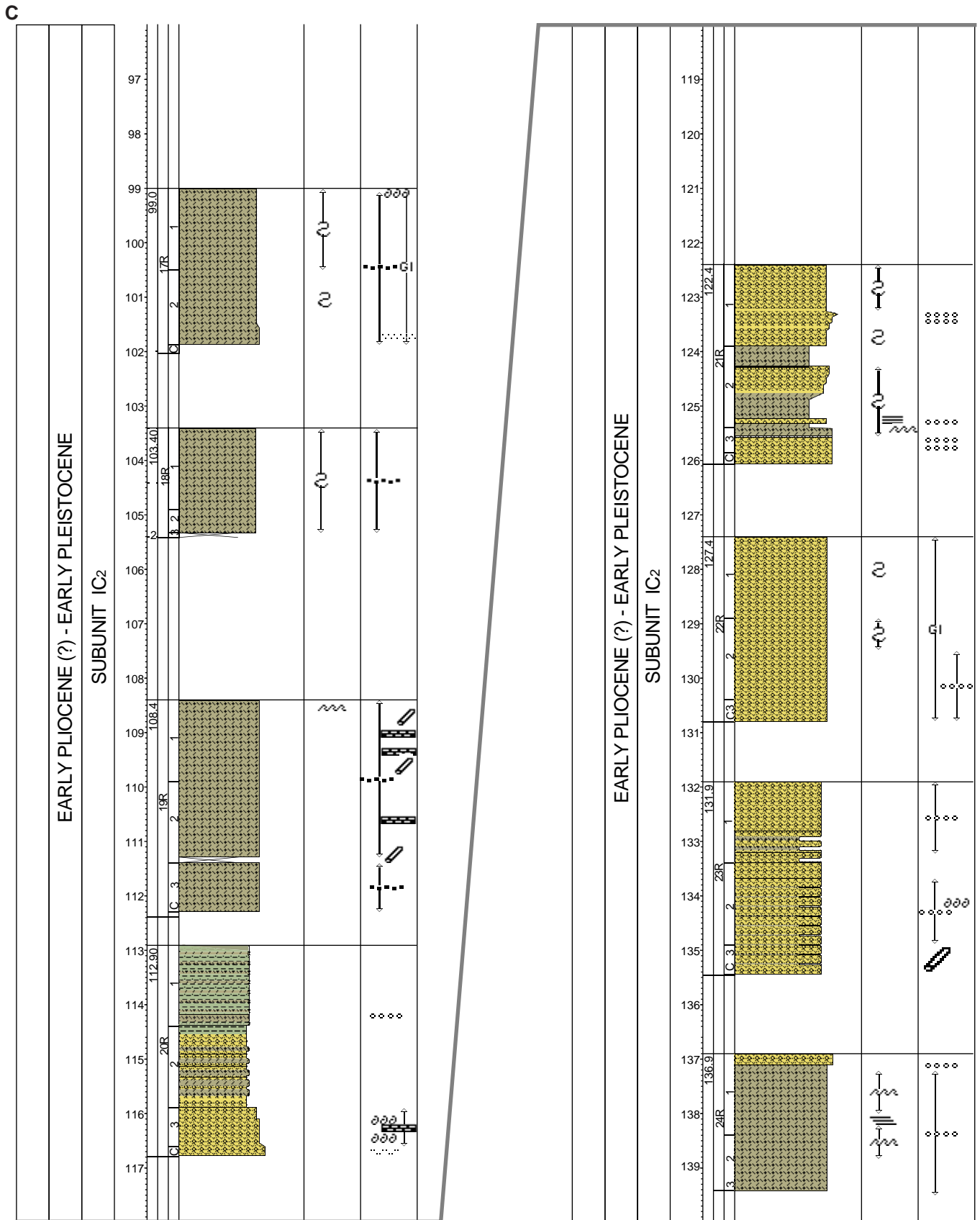


Figure 3 (continued).



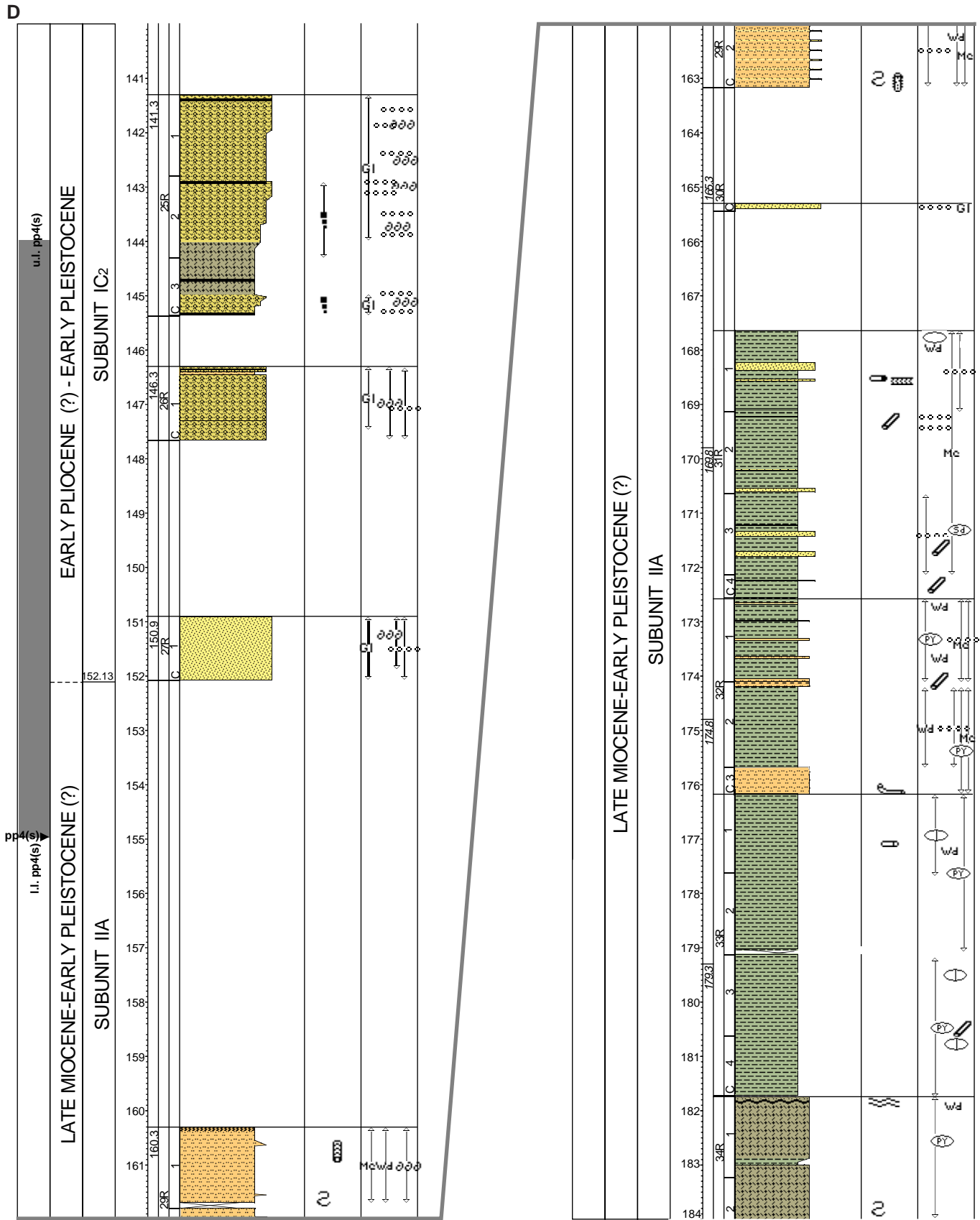


Figure 3 (continued).

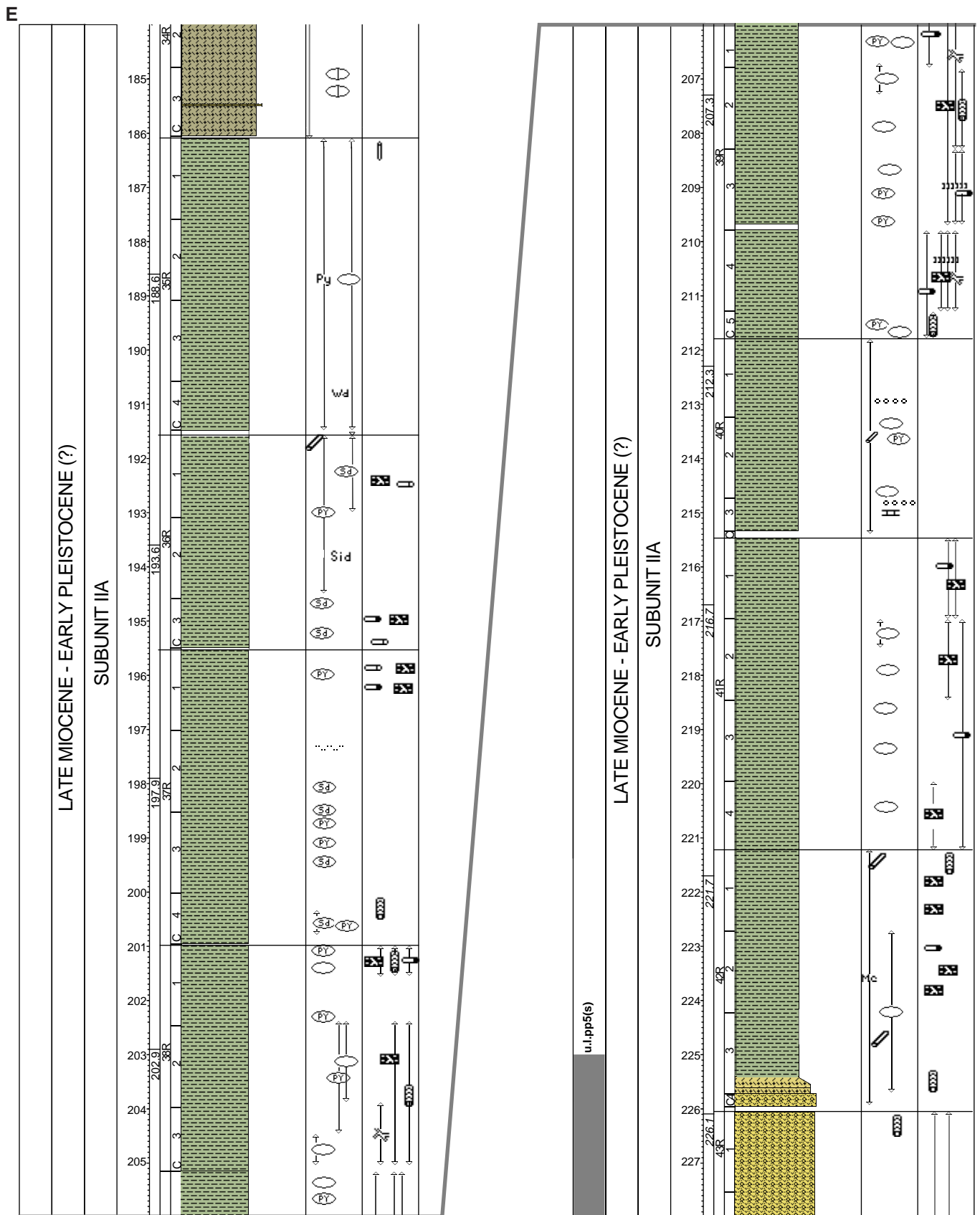


Figure 3 (continued).

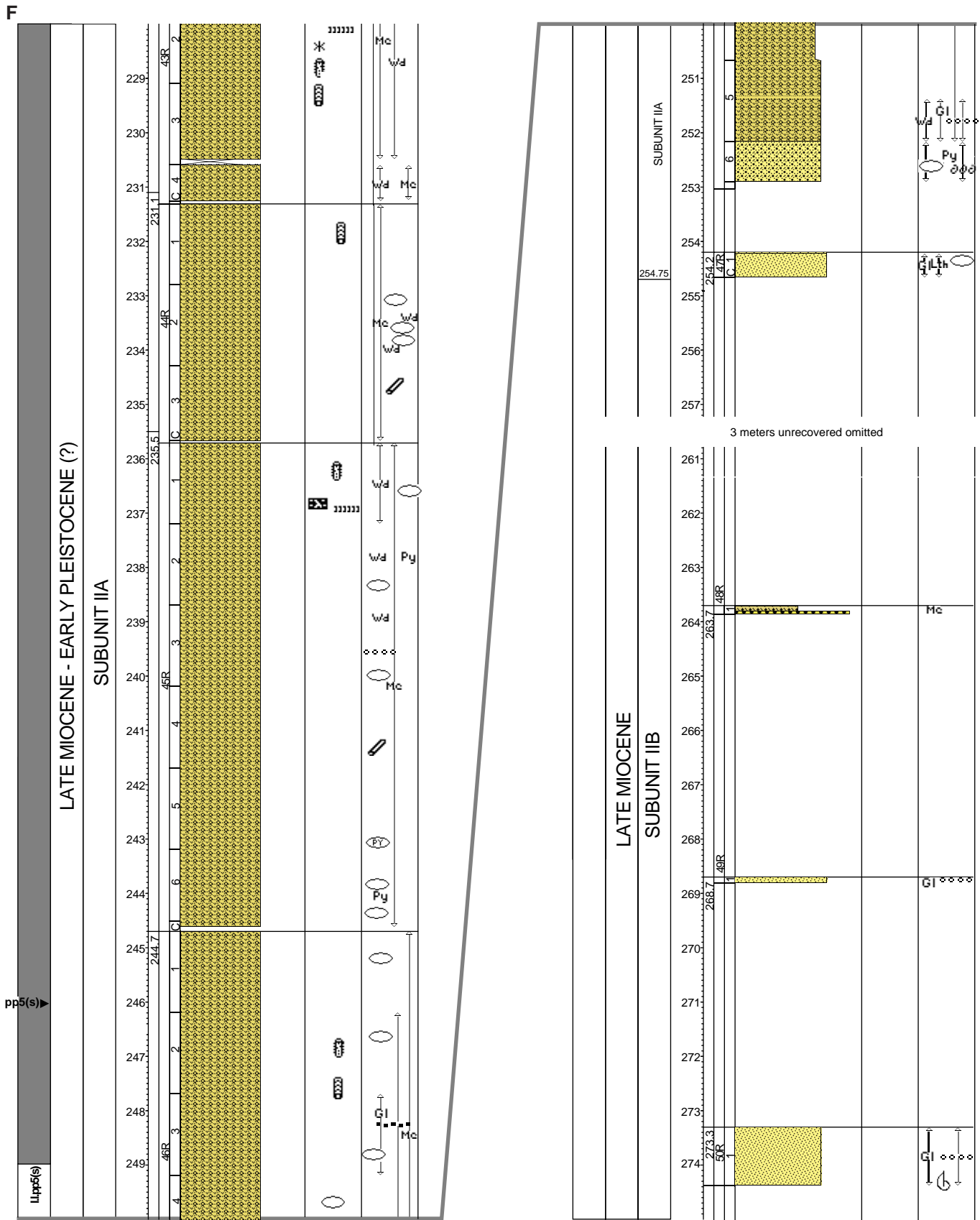


Figure 3 (continued).

Table 2. Lithostratigraphic summary of Hole 1072A.

Subunit	Series	Core, section, interval (mbsf)	Lithology
IA/IB	Holocene(?)—upper Pleistocene	174A-1072A-1R-1, 0 cm, to 8R-1, 150 cm (0-57.5)	Silty clays and clays interbedded with sandy clays, sandy silts, and sands. It is assumed that intervals of no recovery contained sands.
IC	lower Pleistocene—lower Pliocene(?)	8R-1, 150 cm, to 27R-CC, 5 cm (57.5-152.13)	Intervals of clayey silt and silty clay separated by silty sand and (presumably) sand (unrecovered sections). Slumped intervals associated with pebbles, granules, and shell fragments are present from 54 to 128 mbsf. Basal glauconite bed.
IIA	lower Pleistocene(?)—upper Miocene	27R-CC, 5 cm, to 47R-CC, 10 cm (152.13-254.75)	Sandy silt and pebbly, glauconitic, quartz sandstone at top. Silty clay interbedded with sand and sandy silt contains pyrite and siderite nodules, scattered granules, and woody fragments. Glauconitic silty sand at base.
IIB	upper Miocene	47R-CC, 10 cm, to 50R-1, 108 cm (254.75-274.38)	Sandy clay, silt, and gravel at top. Poorly sorted, fine- to coarse-grained, glauconitic, quartz sandstone at base.

large, concentrically laminated structures (*Taenidium?* *Asterosoma?*) are relatively common.

The clayey silt and silty clay of the top of Subunit IC₁ are underlain by a thick interval of nonrecovery that, on the basis of downhole logs from Hole 1072A (see “Downhole Logging” section, this chapter), is dominated by relatively clean sand (interval 174A-1072A-11R-CC, 8 cm, to 15R-1, 0 cm). Below this interval, 13 cored segments of variable thickness were recovered and are defined as Subunit IC₂. These sediments are dominated by dark gray, very dark gray, olive gray, and dark greenish gray, micaceous muddy sand (e.g., intervals 174A-1072A-15R-1, 0–84 cm; 22R-1, 0 cm, to 22R-CC, 8 cm); dark gray, dark greenish gray, and dark grayish brown sandy mud (e.g., intervals 174A-1072A-16R-1, 0–104 cm; 17R-1, 0 cm, to 17R-CC, 15 cm; 18R-1, 0 cm, to 18R-CC, 8 cm; and 19R-1, 0 cm, to 19R-CC, 8 cm); or interbeds of both. Deformed beds (Fig. 5) are pervasive from 89.7 to 105.3 mbsf (e.g., interval 174A-1072A-15R, 0 cm, to 18R-CC, 8 cm) and from 122.4 to 125.6 mbsf (interval 174A-1072A-21R-1, 0 cm, to 21R-3, 20 cm), and appear to represent slumps. Where slumping is not evident, sediments are homogeneous and completely bioturbated, although they generally lack well-defined burrows. The upper intervals of muddy sand and sandy mud contain abundant fine-grained woody plant detritus, much of which appears to be charcoal (interval 174A-1072A-15R-1, 0 cm, to 20R-CC, 27 cm; 89.7–116.8 mbsf). Glauconite, shells, granules, and pebbles increase progressively toward the base of the subunit (Fig. 6). The basal bed (interval 174A-1072A-27R-1, 0 cm, to 27R-CC, 5 cm) is dusky green and greenish black, poorly sorted, fine- to coarse-grained glauconite sand. The lower boundary of Subunit IC₂ is close to seismic surface pp4(s) (Fig. 3D; see “Seismic Stratigraphy” and “Summary and Conclusions” sections, this chapter).

Unit II

Interval: 174A-1072A-27R-CC, 5 cm, to 50R-1, 108 cm
Depth: 152.13–274.38 mbsf
Age: early Pleistocene(?) to late Miocene

Subunit IIA

Interval: 174A-1072A-27R-CC, 5 cm, to 47R-CC, 10 cm
Depth: 152.13–254.75 mbsf

Subunit IIA is characterized by very good recovery (86%; Figs. 2, 3). Most of the unrecovered section is at the top of the subunit in the depth range from 152.13 to 169.8 mbsf. Downhole logs indicate that unrecovered sediments are probably sands (see “Downhole Logging” section, this chapter). Within this depth range, only two cored intervals were recovered. The first is an olive gray, micaceous sandy silt (interval 174A-1072A-29R-1, 0 cm, to 29R-2, 137 cm). This bioturbated sandy silt contains scattered granules as well as shell and wood fragments. Rare discrete burrows are allied with *Teichichnus* (Fig. 7) and, possibly, *Ophiomorpha*. The second is a very thin, gray, poorly sorted, glauconitic, pebbly, medium- to coarse-grained sandstone (interval 174A-1072A-30R-CC, 0–14 cm; Fig. 8). Thin-section exami-

nation (Sample 174A-1072A-30R-CC, 0–10 cm) of the indurated sandstone indicates that it is a glauconitic quartz arenite. Quartz grains are well rounded to subrounded, but are locally corroded and/or replaced by carbonate cement. Glauconite grains are commonly well rounded and represent nascent through evolved glauconitization stages (McCracken et al., 1996). Oxidation apparently has resulted in the partial limonitization of some glauconite grains. Ancillary components of the sandstone include feldspars (partially replaced by carbonate), lithic grains (polycrystalline quartz, chert, metamorphic rock fragments), and phosphatic grains. Two phases of cementation are indicated. The first occurred before significant compaction (on the basis of visually estimated minus-cement porosities of ~30%) and was characterized by precipitation of circumgranular, isopachous, micritic siderite. The later phase involved precipitation of sparry siderite and, subsequently, ankerite cement in remaining pore space.

Below 169.8 mbsf, core recovery in Subunit IIA was virtually complete. Six lithologic assemblages (1–6) are recognized and described in descending order below. Assemblage 1 (interval 174A-1072A-31R-1, 0 cm, to 32R-3, 48 cm) consists of bioturbated, dark gray to olive gray silty clay with thin interbeds of very fine- to fine-grained sand and sandy silt, and scattered granules and pebbles, pyrite and carbonate (siderite?) nodules, and woody fragments. Rare discrete burrows include *Teichichnus*, *Zoophycos*(?), and *Terebellina*(?). Assemblage 2 is a dark gray, bioturbated silty clay (interval 174A-1072A-33R-1, 0 cm, to 33R-4, 109 cm) containing pyrite and incipient carbonate (siderite?) nodules (Fig. 9) and disseminated organic detritus. Some burrows in Assemblage 2 have been identified as *Palaeophycus*, although discrete burrows are rare and difficult to identify because of biscuiting. Assemblage 3 (interval 174A-1072A-34R-1, 0 cm, to 34R-3, 127 cm) is characterized by dark gray sandy mud with interbeds of silty clay and muddy sand, scattered small pyrite and carbonate nodules, and isolated concentrations of organic detritus. Sediments are thoroughly bioturbated, but discrete burrows are rare and difficult to identify because of biscuiting. Assemblage 4 (interval 174A-1072A-35R-1, 0 cm, to 42R-3, 49 cm) is dominated by color-banded (dark gray to olive gray), micaceous silty clay with common carbonate (siderite?) and pyrite nodules. Diffuse color banding may be a product of carbonate diagenesis. Bioturbation is thorough, and discrete burrows are rare to common. Although biscuiting commonly precludes positive identification of ichnofossils, discrete burrows tentatively identified include *Chondrites*, small *Planolites*, *Palaeophycus*, *Teichichnus*, *Thalassinoides*, and *Taenidium*. Assemblage 5 (interval 174A-1072A-42R-3, 49 cm, to 46R-5, 15018 cm) is dark gray, thoroughly bioturbated, micaceous, very fine-grained muddy sand with scattered organic detritus and siderite (and/or phosphatic) nodules. Pyrite nodules and glauconite are common in the basal part. Ichnofossils recognized despite common biscuiting include *Taenidium*, *Asterosoma*, *Teichichnus*, large mud and/or pellet-lined burrows (*Ophiomorpha*?), pellet-filled burrows, and rare *Chondrites*-like structure. Assemblage 6, the basal beds of Subunit IIA (interval 174A-1072A-46R-6, 0 cm, to 47R-1, 0 cm), is a dark greenish gray, very poorly sorted, glauconitic silty sand with sideritic and phosphatic(?) nodules.

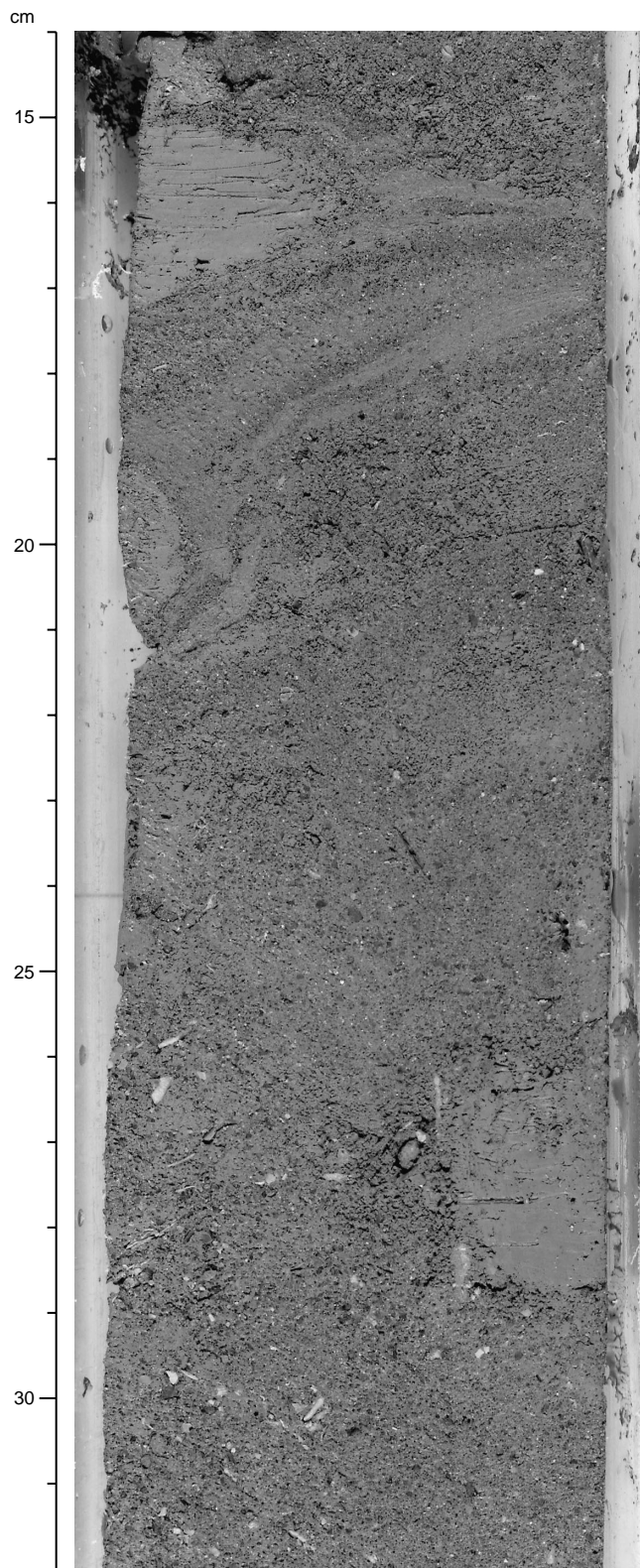


Figure 4. Deformed layers of olive gray sandy mud common at the top and bottom of Subunit IA/IB, which are interpreted as slumps. Note the mud clast at 26–29 cm (interval 174A-1072A-5R-1, 14–32 cm).

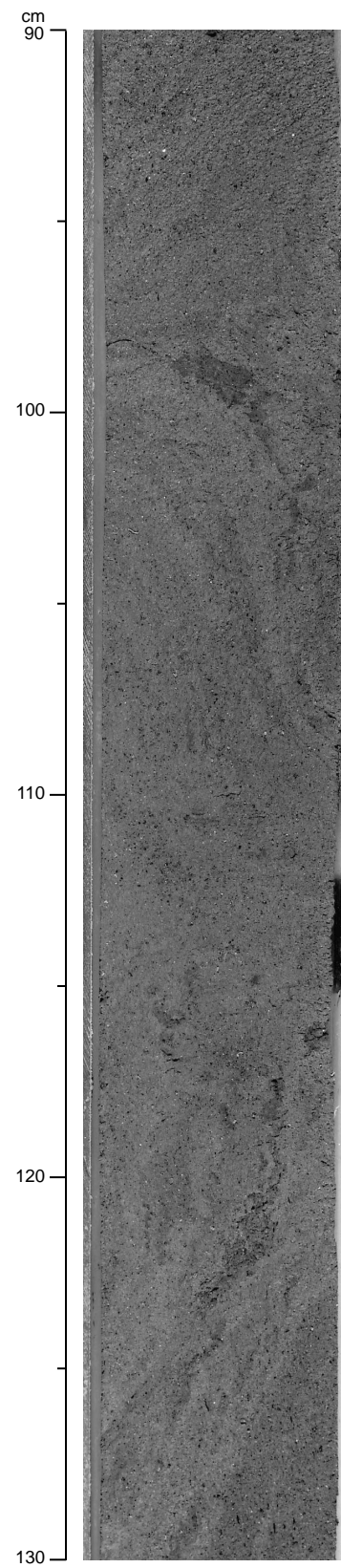


Figure 5. Steeply dipping, discordant, and deformed layers in sandy mud of Subunit IC₂ (interval 174A-1072A-18R-1, 90–130 cm), which are interpreted as slumps. This facies corresponds to the hummocky seismic facies around 220–240 ms TWTT, below surface pp3(s) (see “Seismic Stratigraphy” section, this chapter).

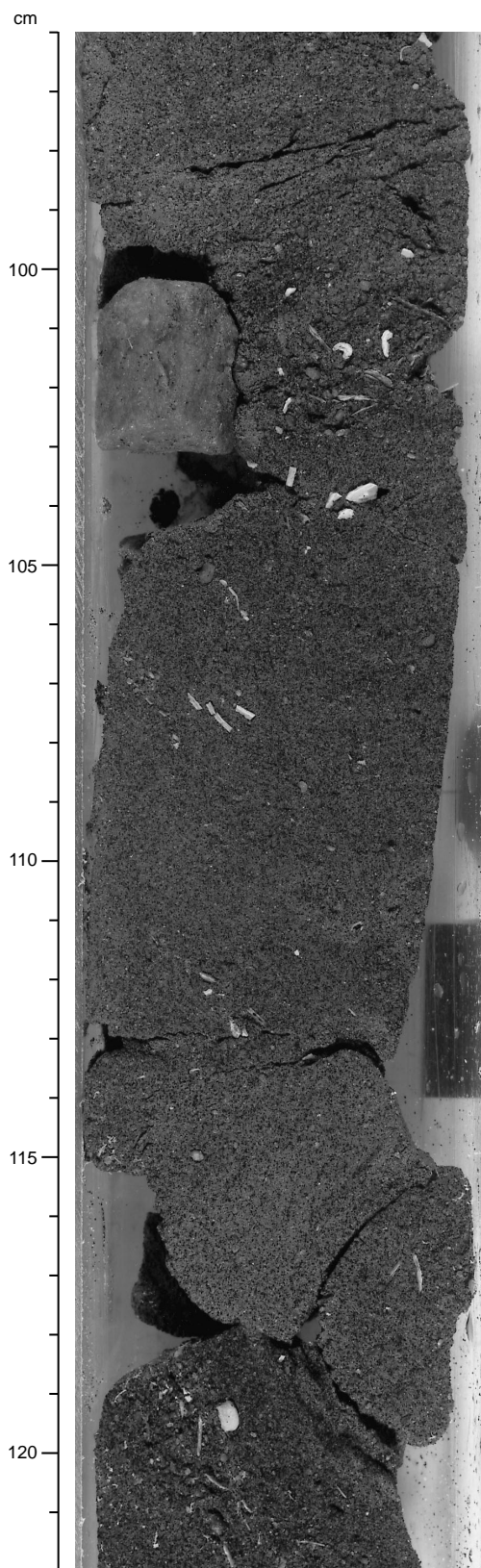


Figure 6. Muddy glauconitic sand with shell fragments and pebbles (at 100–103 cm) at the base of Subunit IC₂ (interval 174A-1072A-26R-1, 96–122 cm). This facies corresponds to the high gamma-ray peak around 150 mbsf (see “Downhole Logging” section, this chapter), or near seismic surface pp4(s).

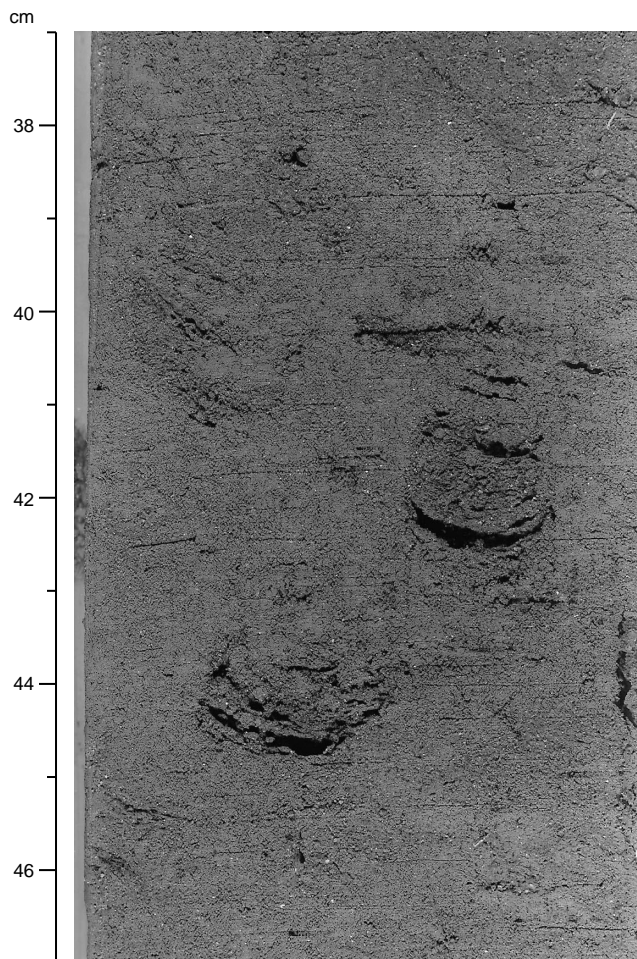


Figure 7. *Teichichnus* burrows in sandy silt of Subunit IIA (interval 174A-1072A-29R-1, 37–47 cm).

Subunit IIB (or IIB/IIC?)

Interval: 174A-1072A-47R-CC, 10 cm, to 50R-1, 108 cm
Depth: 254.75–274.38 mbsf

Subunit IIB is characterized by extremely poor recovery, presumably reflecting the predominance of clean sands (Figs. 2, 3). Only three short (1 m or less) cores were recovered within this interval. With increasing depth, these are (1) dark greenish gray, poorly sorted, micaceous sandy mud and gravel (interval 174A-1072A-48R-CC, 0–15 cm); (2) dark greenish gray, very poorly sorted, medium- to coarse-grained glauconitic sandstone (interval 174A-1072A-49R-CC, 0–10 cm); and (3) dark gray, very fine- to fine-grained, moderately sorted, glauconitic pebbly sandstone (interval 174A-1072A-50R-1, 1–108 cm; Fig. 10). Petrographic examination of the middle core (Sample 174A-1072A-49R-1, 7–10 cm) reveals that framework composition and cementation history are virtually identical to that for the sandstone described in Subunit IIA. Glauconite, however, appears to be more evolved overall (Odin and Matter, 1981) and is locally replaced by pyrite.

Mineralogy

Mineralogical assemblages observed in smear slides and in X-ray diffraction (XRD) analyses from Site 1072 samples are similar to those of Site 1071 (Figs. 11, 12; Table 3). Quartz, feldspars, glauconite, micas (muscovite, biotite, and chlorite), clays, carbonate,

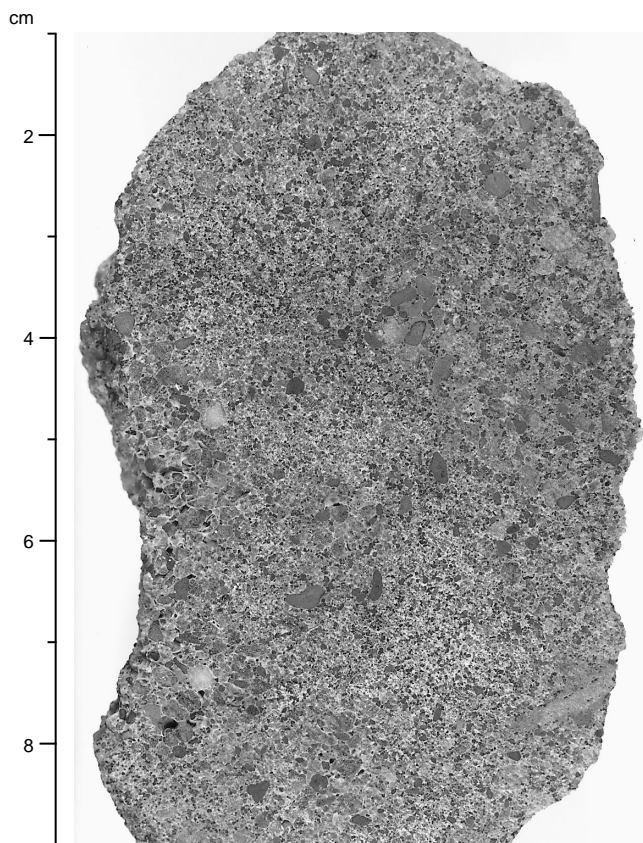


Figure 8. Glauconitic, pebbly, medium- to coarse-grained sandstone in Subunit IIA (interval 174A-1072A-30R-CC, 1–9 cm).

opaque minerals, Fe-oxide, and accessory minerals (e.g., amphibole, rutile) are observed in smear slides. In addition, XRD analyses permit identification of calcite, dolomite, amphibole, siderite, and pyrite. The sediment contains no biogenic components except in smear-slide Sample 174A-1072A-23R-1, 80 cm (132.7 mbsf; Subunit IC), where foraminifers are observed (1%). Generally, quartz content observed from XRD analyses increases from the top to the base of each hole and shows no major correlation with grain-size variations (Fig. 11).

Overall, smear-slide data reflect lithologic trends (Fig. 12). For example, glauconite and mica contents are greatest in sandy intervals. Percentages of carbonate show the same patterns as calcite and dolomite contents derived from XRD analyses, as well as CaCO_3 contents derived from organic geochemistry analyses (see “Organic Geochemistry” section, this chapter).

Subunit IA/IB

The percentage of glauconite seems to increase from the top to the base of Subunit IA/IB, whereas carbonate and clay contents show the opposite trend. This could be explained by the coarsening of the grain size from silty clay at the top of this subunit to sandy silt and clayey sand at the bottom. On the basis of smear-slide analyses, the other minerals do not show any clear compositional trend. However, where the content of feldspars decreases, clay percentage increases and vice versa. This suggests that weathering of feldspars contributed to the clay abundance, because feldspar is the first mineral to break down into clays. As at Site 1071, XRD analyses show that calcite and dolomite are abundant at the top of Hole 1072A. Total calcium carbonate content and smear-slide analyses show a similar pattern (see “Organic Geochemistry” section, this chapter).

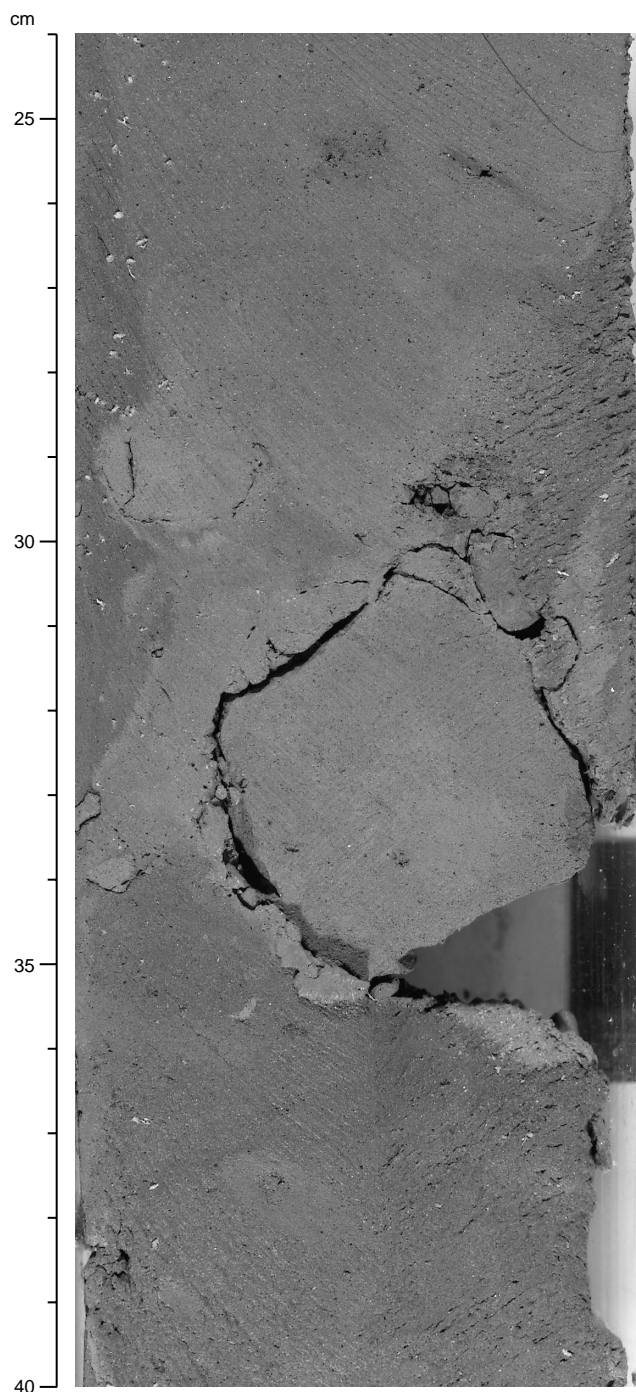


Figure 9. Grayish brown carbonate (siderite?) nodule in dark gray silty clay. Such nodules are common accessories in Subunit IIA (interval 174A-1072A-33R-3, 24–40 cm).

Subunit IC

Overall, the sediment of Subunit IC is coarse-grained ($>250 \mu\text{m}$) when compared with Subunits IA/IB and IIC. Also, mica and glauconite percentages in smear slides are higher than in Subunit IA/IB. Carbonate content is high in the top of this subunit, but decreases abruptly below ~ 70 mbsf (starting from Section 174A-1072A-15R-1; Fig. 11). Generally, the percentages of amphibole and feldspars are similar through Subunits IC and IIA (Fig. 11). When compared with

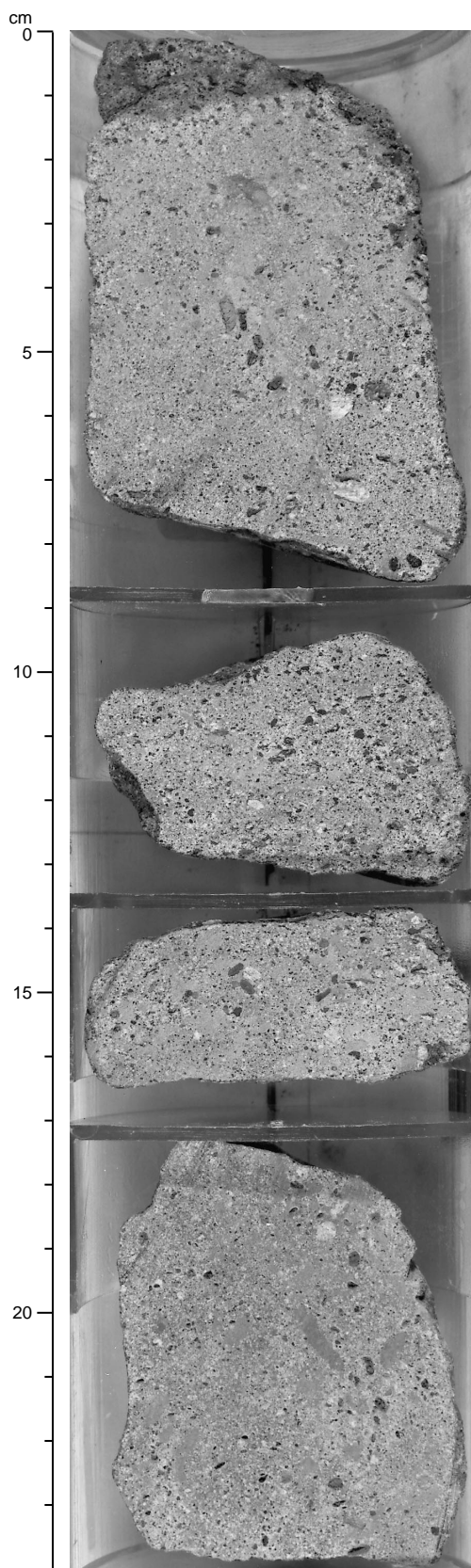


Figure 10. Dark gray, very fine- to fine-grained glauconitic pebbly sandstone (interval 174A-1072A-50R-1, 0–24 cm).

the grain-size data, amphibole and feldspars show a good correlation with the coarse-grained fraction ($>250\ \mu\text{m}$), especially at the top of Subunit IC. There are also good correlations between the abundances of feldspars, amphibole, calcite, dolomite, and sand-sized grains ($>250\ \mu\text{m}$) at 70 mbsf, below the level of seismic surface pp3(s) (Fig. 11; see “Seismic Stratigraphy” section, this chapter). The relationships among mineralogy, grain size, and inorganic geochemistry (see “Inorganic Geochemistry” section, this chapter, and Shipboard Scientific Party, 1994) suggest that calcite and dolomite at this depth (70 mbsf) are detrital in origin. Clay mineral abundance correlates to the percentage of very fine sand ($63\text{--}150\ \mu\text{m}$) measured from 60 mbsf to the bottom of Hole 1072A.

Subunit IIA

Lower percentages in smear slides of quartz + feldspars, glauconite, and mica in the upper part of Subunit IIA reflect the dominance of silt- and clay-sized sediments. From 220 mbsf to the base of the subunit, quartz + feldspars, glauconite, and mica content increase, whereas the clay content decreases, which reflects coarser sediments. XRD analyses show that, except for a peak at ~ 230 mbsf, feldspars and amphibole are poorly represented in this subunit (Fig. 11).

The siderite and pyrite at the bottom of Subunit IIA are considered diagenetic (see “Inorganic Geochemistry” section, this chapter); as at Site 1071, the percentage of siderite and pyrite increases down to 220 mbsf. From 220 mbsf to the bottom of the hole, XRD analyses show that the percentage of pyrite increases, whereas the abundance of siderite decreases (Fig. 11).

BIOSTRATIGRAPHY

As at Site 1071, biostratigraphic resolution at Site 1072 is limited for calcareous planktonic microfossils because of strong carbonate dissolution and shallow water depths that were unfavorable to these organisms. Nannofossils provide relatively useful zonation for the Pleistocene and early Pliocene to late Miocene. Planktonic foraminifers have limited use for biostratigraphic zonation at Site 1072, although it was possible to identify late Miocene and late Pliocene ages on the basis of the presence/absence of rare taxa.

Pleistocene benthic foraminiferal faunas vary from assemblages dominated almost exclusively by *Elphidium excavatum* to more diverse assemblages, probably reflecting changing paleodepths or substrates related to glacial/interglacial cycles and/or changes in sediment input. Benthic foraminiferal species abundances indicate that paleodepths in the Pleistocene fluctuated from inner neritic (0–50 m) to upper middle neritic ($\sim 50\text{--}65$ m). Pliocene–Miocene biofacies are characterized by *Buliminella gracilis* and *Uvigerina juncea*, indicating middle neritic paleodepths (50–100 m).

Organic microfossils are common to abundant in most samples studied, particularly in pre-Pleistocene sediments. Although terrestrial palynomorphs (pollen and spores) dominate all samples, dinocysts are relatively more abundant in pre-Pleistocene sediments. Reworking is evident in many samples, and it is possible that some well-preserved reworked organic microfossils cannot be differentiated from in situ fossils, making age determinations difficult. Stratigraphic discontinuity pp4(s) can be recognized in a sequence of early Pliocene/late Miocene–early Pleistocene age.

The biostratigraphy of Site 1072 is summarized in Figure 13. An age-depth plot showing the age ranges interpreted from microfossil assemblages is shown in Figure 14.

Calcareous Nannofossils

Similar to Site 1071, nannofossils are generally rare or absent in the sediments recovered from Site 1072. The identification of age-

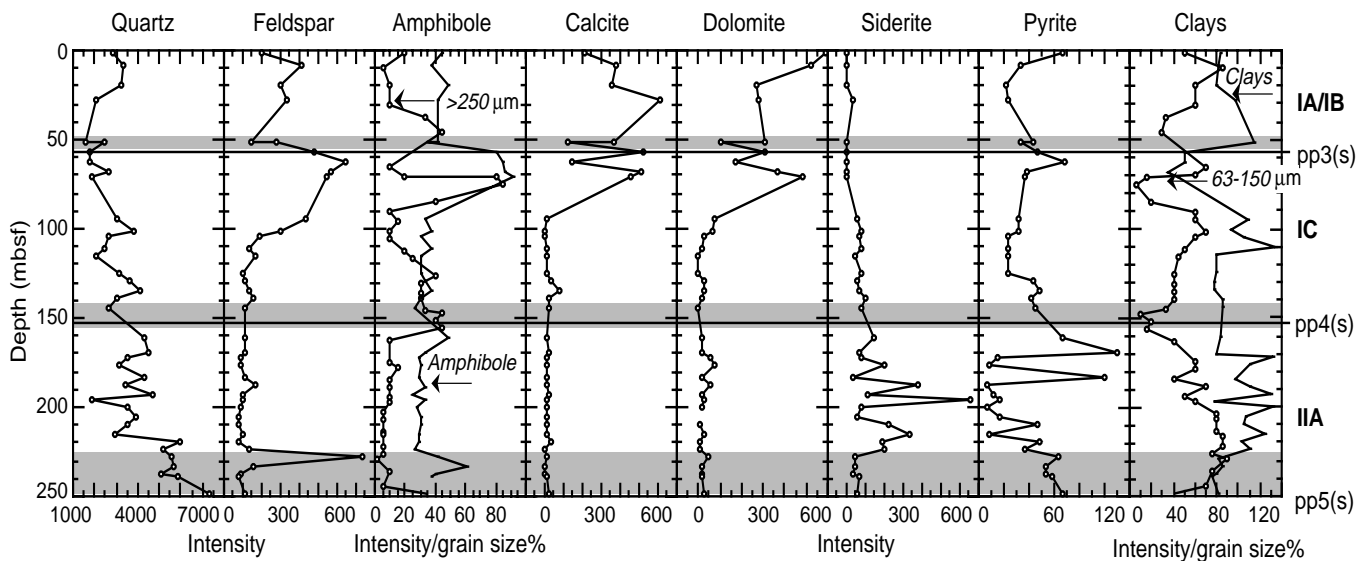


Figure 11. Relative intensity vs. depth in XRD analyses of common minerals in Hole 1072A. Amphibole and clays are also compared downhole with estimated grain-size percentages (>250 μm and 63–150 μm, respectively). Grain sizes were determined by estimating the percent fractions recovered after sieving the core-catcher sediment through 63- to 150-μm, 150- to 250-μm, and >250-μm meshes. Lithostratigraphic Subunits IA/IB, IC, IIA, IIB/IIC, and approximate locations of seismic discontinuities pp3(s), pp4(s), and pp5(s) are noted on right vertical axis. Gray shaded areas show depths of seismic surfaces calculated using the velocity curve derived from Oc270 (see “Seismic Stratigraphy” section, this chapter).

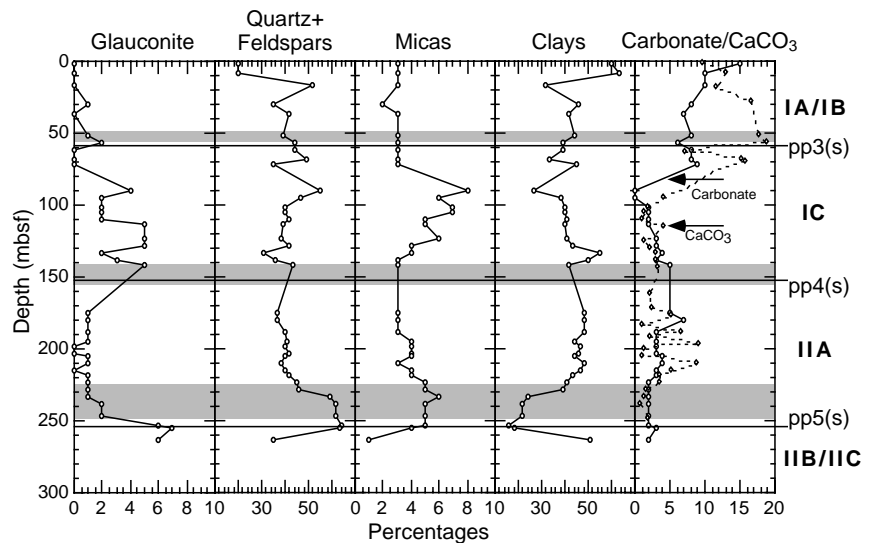


Figure 12. Percentages of glauconite, quartz + feldspars, micas, clays, carbonate (from smear slides), and CaCO₃ content (measured) vs. depth for Hole 1072A. Gray shaded areas show depth ranges of seismic surfaces calculated using the velocity curve derived from Oc270 (see Table 22, “Seismic Stratigraphy” section, this chapter).

diagnostic species in a few samples provides some useful biostratigraphic information.

Samples 174A-1072A-1R-CC through 3R-CC (2.22–19.60 mbsf) are barren of nanofossils. Rare specimens of reworked Paleogene nanofossils were found in Sample 174A-1072A-2R-CC (9.59 mbsf). Samples 174A-1072A-4R-CC (30.81 mbsf) and 5R-CC (37.13 mbsf) contain rare specimens of *Gephyrocapsa* spp. (small), which generally range from the Pliocene through the Holocene. Samples 174A-1072A-6R-CC (46.08 mbsf) and 7R-CC (53.27 mbsf) are barren of nanofossils. Sample 174A-1072A-8R-CC (57.79 mbsf) yields common *Gephyrocapsa* spp. (small) and rare *Gephyrocapsa parallela*. The presence of the latter species and the absence of *Emiliana huxleyi* suggest an age within Zone CN14 (0.25–0.9 Ma). Samples 174A-1072A-9R-CC (65.00 mbsf) through 12R-CC (75.20 mbsf) contain few to common *Gephyrocapsa* spp. (small) and rare *Gephyrocapsa parallela* and *Pseudoemiliana lacunosa*. The co-oc-

currence of the latter two species defines Subzone CN14a (0.46–0.9 Ma).

Samples 174A-1072A-14R-CC through 17R-1, 79 cm (84.70–99.79 mbsf), yield only rare specimens of *Gephyrocapsa* spp. (small). Samples 174A-1072A-17R-CC through 25R-CC (101.96–145.36 mbsf) are barren of in situ nanofossils. Reworked Cretaceous and Paleogene nanofossils were found in Samples 174A-1072A-21R-CC (126.05 mbsf) and 24R-CC (139.42 mbsf). Sample 174A-1072A-26R-CC (147.65 mbsf) contains rare *Gephyrocapsa* spp. (small), *Calcidiscus leptoporus*, *Gephyrocapsa caribbeanica*, and *Pseudoemiliana lacunosa*. The presence of the latter two species suggests an age within Subzone CN13b (0.9–1.7 Ma). Samples 174A-1072A-27R-CC through 30R-CC (152.08–165.40 mbsf) are barren of nanofossils.

Rare specimens of *Reticulofenestra pseudumbilicus* and/or *Sphenolithus* spp. occur sporadically from Samples 174A-1072A-

Table 3. Relative intensity of main X-ray diffraction peaks for minerals in representative samples from Hole 1072A.

Depth (mbsf)	Quartz	Feldspar	Amphibole	Calcite	Dolomite	Siderite	Pyrite	Clays
1.87	2818	197	44	217	591	0	67	84
8.19	3360	417	38	375	518	0	33	82
19.22	3195	300	49	358	270	0	22	79
28.25	2032	331	41	611	278	29	23	97
51.68	1559	140	42	370	308	0	44	115
51.80	2427	282	35	123	102	0	33	115
57.54	1770	476	80	527	306	0	46	51
63.18	1764	643	85	144	177	0	68	51
68.00	2648	564	86	507	369	0	39	36
70.84	1881	544	92	458	487	0	37	45
94.37	3050	432	33	13	77	55	32	108
101.30	3806	300	37	0	63	83	32	93
104.26	2691	190	31	0	23	72	24	105
110.70	2438	139	38	7	21	82	23	134
115.11	2074	166	30	15	0	44	24	79
124.70	3111	105	31	10	0	80	23	80
129.63	3584	114	34	30	22	60	43	78
134.14	4080	130	37	80	25	64	49	78
139.16	3042	157	31	24	19	100	42	86
144.15	2704	115	27	22	0	75	45	86
161.21	4287	115	49	16	17	149	67	84
169.86	4472	110	33	23	15	64	110	80
172.18	3521	87	29	15	54	82	15	132
176.50	3098	93	30	14	73	201	9	110
183.99	4294	109	29	7	19	39	100	97
188.22	3392	165	33	6	57	378	6	110
192.53	4696	98	25	22	18	108	12	130
196.45	1901	99	33	11	26	659	16	78
200.20	3556	84	28	14	13	74	7	132
205.20	3934	83	30	8		58	17	107
209.65	3556	83	31	11	10	219	47	106
214.67	2996	95	29	11	27	339	9	125
219.02	5989	82	29	33	12	191	48	103
223.91	5223	133	26	4	11	202	36	110
228.40	5608	730	41	6	45	41	64	82
233.42	5649	156	61	0	15	41	54	86
237.82	5041	91	40	0	18	32	53	80
238.93	5850	83	38	11	20	65	59	75
249.13	7365	113		22	22	58	67	81

Note: See also Figure 11.

31R-1, 79 cm, through 47R-CC (170.59–254.65 mbsf). These species indicate an age of early Pliocene or older (Zones CN11–CN5b, >3.8 Ma). The absence of *Cyclicargolithus floridanus*, a generally ubiquitous species in middle Miocene to Eocene marine sediments, constrains the stratigraphic interval to be late Miocene or younger. No nannofossils were found in Sample 174A-1072A-48R-CC (263.78 mbsf). Only one sample was available from Hole 1072B; this sample (174A-1072B-3R-CC; 330.40 mbsf) is barren of nannofossils.

Planktonic Foraminifers

Planktonic foraminifers are absent from Samples 174A-1072A-1R-CC through 3R-CC (2.22–19.60 mbsf). In the interval 30.81–75.20 mbsf (Samples 174A-1072A-4R-CC through 12R-CC), planktonic foraminifer abundances range from rare to common, and their preservation is generally very good. The presence of *Globorotalia inflata* and *Neogloboquadrina dutertrei* in this interval suggests an age range of Holocene to late Pliocene, and the occurrence of *Globorotalia truncatulinoides* in Samples 174A-1072A-9R-CC (65.00 mbsf) and 11R-CC (71.12 mbsf) indicates an age of <2.0 Ma. The most abundant taxa in the interval from 30.81 to 75.20 mbsf are *Globigerina quinqueloba*, *Globigerinella pseudobesa*, *Globorotalia inflata*, and *Neogloboquadrina pachyderma*. Additional taxa that occur in this interval include *Globigerina bulloides*, *Globigerinoides immaturus*, *Globigerinoides obliquus*, *Globigerinoides ruber*, *Globigerinoides sacculifer*, *Globigerinoides quadrilobatus*, *Globigerinita glutinata*, *Globorotalia scitula*, and *Orbulina suturalis*.

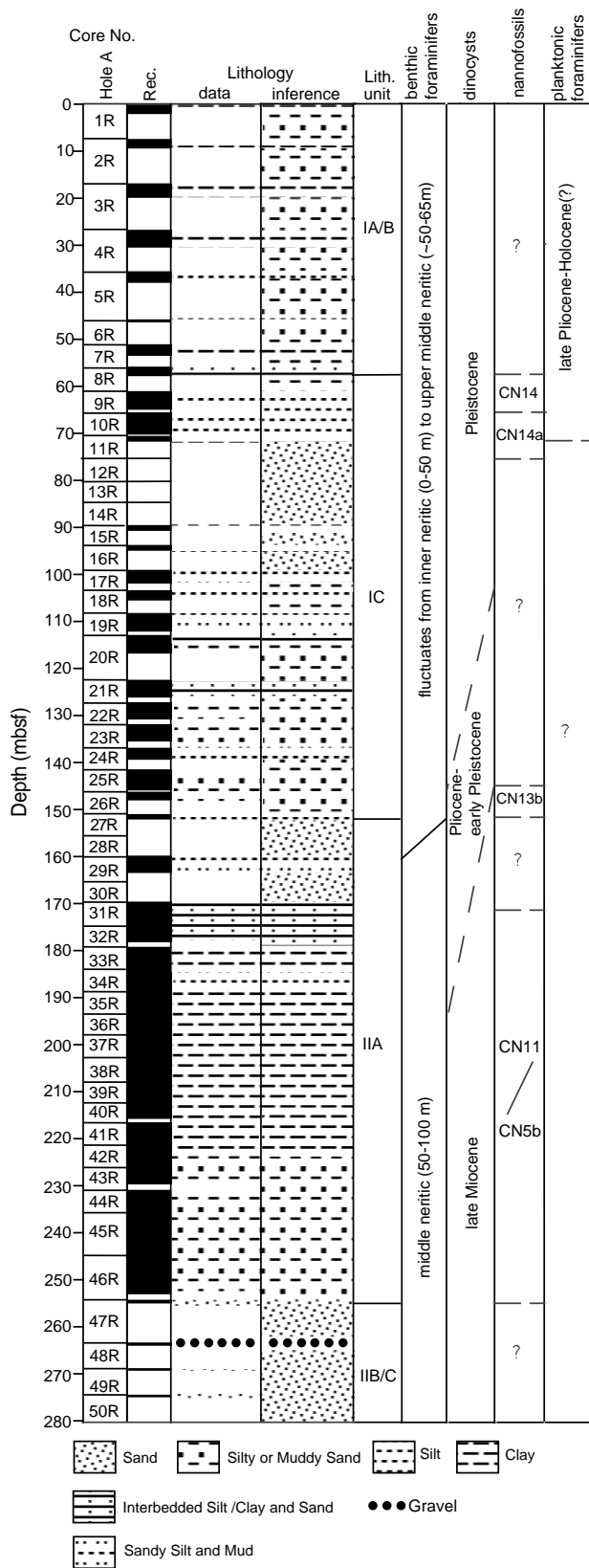
Most samples studied from 84.70 to 178.27 mbsf (Samples 174A-1072A-14R-CC through 32R-CC) are barren of planktonic foraminifers; where present, they are extremely rare (usually only one specimen per sample). The exceptions are in Samples 174A-1072A-23R-

CC (135.45 mbsf) and 24R-CC (139.42 mbsf), where planktonic foraminifers are rare to frequent. The presence of *Neogloboquadrina pachyderma* in these samples suggests an age of <9.2 Ma.

Planktonic foraminifers from 184.69 to 222.48 mbsf (Samples 174A-1072A-33R-CC through 41R-CC) are rare to frequent and include *Globigerina bulloides*, *Globigerina woodi*, *Globigerinoides immaturus*, *Globigerinoides obliquus*, *Globigerinoides quadrilobatus*, *Globigerinoides trilobus*, *Globigerinella pseudobesa*, *Globigerinita glutinata*, *Globorotalia scitula*, *Neogloboquadrina continuosa*, *Neogloboquadrina pachyderma*, *Orbulina bilobata*, *Orbulina suturalis*, and *Orbulina universa*. The presence of *Neogloboquadrina pachyderma* from 184.69 to 222.48 mbsf suggests an age of <9.2 Ma. The few specimens of *Neogloboquadrina continuosa* suggest a Miocene age (although reworking is a possibility). The absence of *Globorotalia truncatulinoides*, *Globorotalia inflata*, and *Neogloboquadrina dutertrei* may also indicate that this interval is >2.0 Ma. However, the rarity of species in Samples 174A-1072A-14R-CC through 32R-CC (84.7–178.27 mbsf), coupled with the fact that dissolution is strong throughout this recovered interval (184.69–222.48 mbsf), suggests an age range of 2.0–9.2 Ma, which, although consistent with other biostratigraphic data, should be viewed cautiously.

Apart from Sample 174A-1072A-47R-CC (254.65 mbsf), all core-catcher samples studied for Samples 174A-1072A-42R-CC through 48R-CC (226.43–263.78 mbsf) are barren of planktonic foraminifers. The rare planktonic foraminifer specimens in Sample 174A-1072A-47R-CC include *Candeina nitida*, which suggests an age of <8.1 Ma.

Wherever possible, the percentage of planktonic foraminifers relative to total foraminifers was recorded for all samples studied. For Samples 174A-1072A-4R-CC through 12R-CC (30.81–75.20 mbsf), the percentage of planktonic foraminifers varies from 1% to 57%. For



Figures 13. Biostratigraphic zonation from dinocyst, nannofossil, and planktonic foraminiferal assemblages, and paleobathymetry on the basis of benthic foraminifers for Site 1072.

Samples 174A-1072A-33R-CC through 41R-CC (184.69–222.48 mbsf), the percentage of planktonic foraminifers varies from <1% to 70%. As at Site 1071, the paucity of planktonic foraminifers throughout most of the recovered interval in Hole 1072A is most likely attributable to dissolution and the shallow (inner-middle neritic) paleoenvironments interpreted from benthic foraminifers. Only one broken, unidentifiable planktonic foraminifer was found in the single sample available from Hole 1072B (Sample 174A-1072B-3R-CC; 330.40 mbsf).

Benthic Foraminifers

Benthic foraminifers are rare to common in Pleistocene samples examined from Site 1072 (Samples 174A-1072A-1R-CC through 24R-CC; 2.22–139.42 mbsf). Fluctuations from faunas dominated almost exclusively by *Elphidium excavatum* to more diverse assemblages most likely reflect changing paleodepths or substrates related to glacial/interglacial cycles and/or changes in sediment input. Benthic foraminiferal species abundances indicate that paleodepths in the Pleistocene ranged from inner neritic (0–50 m) to upper middle neritic (~50–65 m) at Site 1072. Pleistocene samples dominated by *Elphidium excavatum* reflect inner neritic paleodepths (0–50 m), on the basis of the distribution of modern *Elphidium* biofacies on the New Jersey shelf (Poag et al., 1980) and the Chesapeake Bay shelf (Ellison and Nichols, 1976). Relative abundance changes of *Elphidium excavatum forma clavatum* (glacial) and *Elphidium excavatum forma lidoensis* (interglacial; Buck and Olson, in press) in core-catcher samples indicate that a high-resolution shore-based study may provide a detailed record of transgressive/regressive intervals and glacial/interglacial cycles in the Pleistocene section at Site 1072. Deep-water biofacies at Site 1072 yield species such as *Bolivina subaenariensis*, *Bulimina marginata*, *Cassidulina norcrossi*, *Cassidulina teretis*, *Cibicides lobatulus*, *Cibicidoides* spp., *Globobulimina auriculata*, *Nonionella miocenica stella*, *Quinqueloculina seminulum*, and *Triloculina trigonula*. Samples 174A-1072A-14R-CC through 31R-CC (84.70–174.73 mbsf) are barren or yield rare benthic foraminifer specimens.

Pliocene–Miocene benthic foraminifers are rare to common in samples from Hole 1072A (Samples 174A-1072A-29R-CC through 44R-CC; 163.17–235.47 mbsf). *Buliminella gracilis* and *Uvigerina juncea* are the most abundant species found in most of these samples, indicating middle neritic paleodepths (50–100 m); samples containing more abundant *Buliminella gracilis* may indicate slightly shallower paleodepths (50–80 m) than samples containing more abundant *Uvigerina juncea* (75–100 m), on the basis of faunal studies from New Jersey Coastal Plain boreholes (Miller et al., 1997). Other typical species in these *Buliminella-Uvigerina*-dominated faunas include *Bolivina calvertensis*, *Cassidulina laevigata*, *Quinqueloculina seminulum*, and *Textularia agglutinans*. *Buliminella-Uvigerina*-dominated biofacies may indicate a paleoenvironment that was higher in organic carbon and/or lower in dissolved oxygen content (Snyder et al., 1989; Miller et al., 1997) than biofacies dominated by *Cassidulina laevigata*.

Palynomorphs

Sections 174A-1072A-3R-CC through 17R-CC (19.60–101.96 mbsf) are assigned to the Pleistocene on the basis of sparse dinocyst assemblages dominated by *Brigantidium* spp., with *Spiniferites* spp., *Operculodinium centrocarpum*, and *Lingulodinium machaerophorum*. Samples 174A-1072A-20R-CC through 25R-CC (116.80–145.36 mbsf) are early Pleistocene (1.4 Ma) to Pliocene, on the basis of the presence of *Habibacysta tectata* together with *Operculodinium israelianum*, *Tectatodinium pellitum*, *Lingulodinium machaerophorum*, *Polysphaeridium zoharyi*, *Bitectatodinium tepikiense*, *Senonopemphix nephroides*, *Spiniferites* spp., *Achomospaera* spp., and *Brigantidium* spp. Samples 174A-1072A-35R-CC through 48R-CC (193.99–263.78 mbsf) are assigned to the late Miocene on the ba-

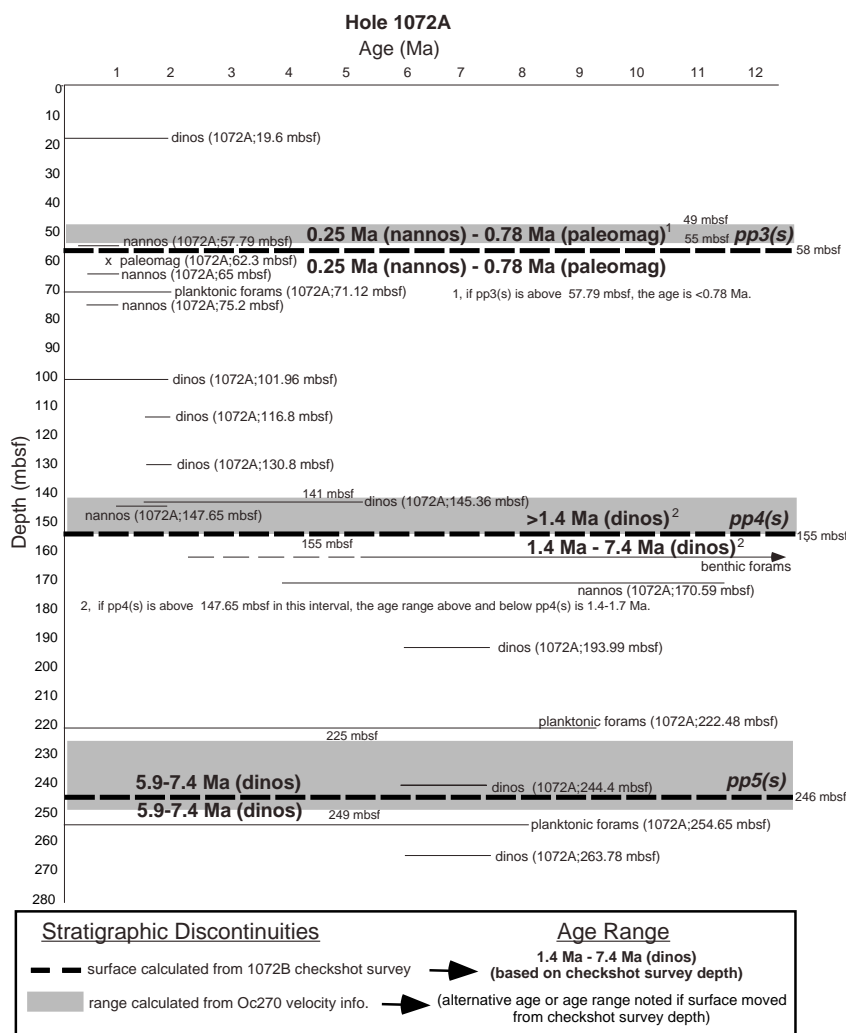


Figure 14. Age-depth plot showing the age ranges interpreted from microfossil assemblages at Site 1072. Depth ranges and checkshot depths for stratigraphic discontinuities pp3(s), pp4(s), and pp5(s) are also illustrated (see Table 22, “Seismic Stratigraphy” section, this chapter); their age constraints are derived from microfossil ranges above and below discontinuities. For example, sediments above pp4(s) must be older than 1.4 Ma on the basis of dinocyst assemblages. Sediments below pp4(s) are 1.4–7.4 Ma on the basis of dinocyst assemblages. Dinosaurs = dinocysts; paleomag = paleomagnetism; nannos = nannofossils; forams = foraminifers.

sis of the presence of *Habibacysta tectata*, *Ermynodinium delectabile*, *Trinovantedinium glorianum*, *Operculodinium janduchenei*, *Filisphaera filifera*, *Selenopemphix dinoaeacysta*, and *Selenopemphix brevispinosa*, together with longer ranging taxa like *Operculodinium centraocarpum*, *Selenopemphix nephroides*, *Lingulodinium machaerophorum*, *Polysphaeridium zoharyi*, *Lejeunecysta* spp., *Spiniferites* spp., and *Brigantedinium* spp. Despite the rare occurrence of cysts with Last Appearance Datum (LAD) levels earlier in the late Miocene (e.g., *Dapsilidinium pseudocolligerum*), the presence of some obviously reworked (corroded) dinocysts (e.g., *Apteodinium tectatum*, *Systematophora placantha*, and *Unipontidinium aquaeductum*) in these samples precludes confident identification of the zones of de Verteuil and Norris (1996). All Miocene sediments recovered are thus tentatively assigned to Zone DN10 (5.9–7.4 Ma).

Biostratigraphic Age Control of Stratigraphic Discontinuities

Where possible, biostratigraphic ages or age ranges were calibrated with stratigraphic discontinuities pp3(s), pp4(s), and pp5(s) for Site 1072. Biostratigraphic age control is derived from Hole 1072A. A calibration chart displays these biostratigraphic data and their accompanying age interpretations (Fig. 14).

Using the Hole 1072B checkshot survey, the depth of pp3(s) was estimated at 58 mbsf for Hole 1072A (see “Downhole Logging” section, this chapter). Paleomagnetic data (B/M boundary; 0.78 Ma) and calcareous nannofossils indicate an age range of 0.25–0.78 Ma for sediments both above and below the surface (Fig. 14). Changing the

depth of pp3(s) within the predrill estimated interval of the surface (49–55 mbsf) on the basis of Oc270 seismic velocity information would make the age of sediments above the surface less constrained, at <0.78 Ma (see “Seismic Stratigraphy” section, this chapter). Using the checkshot survey depth for pp3(s), the age ranges above and below pp3(s) at Site 1072 are compatible with the age ranges interpreted at Site 1071.

Dinocysts provide age constraints for pp4(s) (155 mbsf checkshot survey depth; see “Downhole Logging” section, this chapter). Sediments above the surface are >1.4 Ma and sediments below the surface range in age from 1.4 to 7.4 Ma. If, however, pp4(s) was above 147.65 mbsf (within the predrill seismically estimated interval of 141–155 mbsf), the age ranges both above and below pp4(s) would be much better constrained at 1.4–1.7 Ma, on the basis of additional calcareous nannofossil control. Using the 155 mbsf checkshot survey depth for pp4(s), the age ranges above and below pp4(s) for Site 1072 are the same as the age ranges for this surface at Site 1071.

The age range of sediments both above and below pp5(s) (246 mbsf checkshot survey depth; see “Downhole Logging” section, this chapter) at Site 1072 is 5.9–7.4 Ma; this age is based on dinocysts and is compatible with associated planktonic foraminifers. These age ranges are the same as those calibrated from Site 1071. The continuity of dinocyst ranges across this surface at both sites suggests either that pp5(s) is not an unconformity or that there is little time missing across pp5(s).

The age interpretations of these stratigraphic discontinuities are based solely on biostratigraphic data produced during the cruise. Because of problems with dissolution, reworking and shallow paleo-

bathymetric depths Site 1072 (see sections on specific fossil groups in this report), caution should be employed when using any of these age determinations. Further shore-based work on biostratigraphy, paleomagnetism, and isotope stratigraphy may help fine-tune these ages.

PALEOMAGNETISM

All the archive-half sections from Hole 1072A (RCB cores) were subjected to routine pass-through measurements (Tables 4–7 on CD-ROM, back pocket, this volume). The natural remanent magnetization (NRM) was measured routinely at intervals of 5 cm before demagnetization and after demagnetization at 10 and 20 mT increments. Discrete-cube samples were taken at a rate of one per section and alternating field (AF) demagnetized stepwise in nine steps up to 80 mT. Magnetization intensity after 20 mT is generally 1–100 mA/m for sediments above stratigraphic discontinuity pp5(s) (225–249 mbsf; see “Seismic Stratigraphy” section, this chapter) and <1 mA/m below pp5(s). Generally, RCB coring causes declinations of archive-half sections and discrete-cube samples to disagree.

Typical examples of demagnetization plots for discrete-cube samples are shown in Figure 15. In general, drilling-induced remanence with steep positive inclination is removed by demagnetization up to 20 mT. However, for samples with reversed polarity magnetizations (e.g., Fig. 15D), the normal polarity overprint is in some cases overlapping in the coercivity spectrum, causing a gradual change in paleomagnetic directions up to 60 mT. AF demagnetization above 60 mT is unstable, especially for these kinds of samples, making it difficult to get a reliable linear vector that decreases toward the origin. This feature is suspected to be anhysteretic remanent magnetization (ARM), related to the nature of the samples and the residual magnetic field in the AF demagnetizer (see “Paleomagnetism” section, “Site 1071” chapter, this volume). Figure 15F shows a sample (174A-1072A-39R-2, 59–61 cm; 209.4 mbsf) that is identified as normal polarity; Figure 15G shows a sample (174A-1072A-41R-1, 59–61 cm; 217.3 mbsf) that is identified as having reversed polarity with very shallow inclination. In some cases, the potential reversed magnetization component of samples may not be detected because of a strong and highly coercive normal component.

Magnetostratigraphy

Magnetic polarities were determined mostly from inclination of discrete samples at 20 mT (Fig. 16); these are also partially supported by vector endpoint diagrams for ambiguous samples. Following the criteria described for Site 1071 (see “Paleomagnetism” section, “Site 1071” chapter, this volume), the cut-off value was 1 mA/m. After AF demagnetization at 20 mT, residuals were considered unstable and not included in the polarity interpretation. Data from the intervals 89.7–105.3 mbsf and 122.4–139.5 mbsf were discarded, because they show convoluted layering, which indicates postdepositional deformation/slumping, possibly leading to remagnetization (see “Lithostratigraphy” section, this chapter). Histograms of all the inclinations of discrete samples after 20-mT AF demagnetization are plotted in Figure 17. The average value of positive inclination for all the discrete samples is $53^\circ \pm 20^\circ$, and for the negative inclination is $-31^\circ \pm 19^\circ$. Relatively low values for negative inclination, compared to the expected inclination for this site ($\sim 58^\circ$), may be caused by an overlapping coercivity spectrum of normal positive inclination overprinting the original, reversed, negative inclination magnetization. This can be verified by shore-based study of discrete samples using thermal demagnetization.

Several magnetic polarity boundaries were observed in Hole 1072A (Table 8). The Brunhes/Matuyama (B/M) boundary was found at 62.3 mbsf (Sample 174A-1072A-9R1, 130 cm) within a clayey silt layer (Subunit IC); this interpretation is consistent with

biostratigraphy (calcareous nannofossils), which yields an age between 0.46 and 0.9 Ma (see “Biostratigraphy” section, this chapter). The B/M boundary coincides with a marked increase both in magnetization intensity and downhole susceptibility (Fig. 18). This evidence suggests that the sedimentary environment, which supplied magnetic minerals, changed because of an association with sediments across the boundary, or because the boundary is instead a diagenetic front in the overlying Brunhes Chron. In contrast, magnetization intensity at Site 1071 decreases across the B/M polarity transition downhole, and susceptibility does not change significantly (see “Paleomagnetism” section, “Site 1071” chapter, this volume).

For the interval below the B/M boundary (62.3–152 mbsf), and down to pp4(s) (141–155 mbsf; see “Seismic Stratigraphy” section, this chapter), magnetic polarity is reversed except for a normal zone at 141.8–144 mbsf (Fig. 16) that is associated with intervals of low recovery. Because the boundary between this normal zone and the reversed zone beneath it corresponds to the boundary between a muddy sand and underlying sandy mud at 144 mbsf, careful consideration is needed (i.e., this may correspond to a lithologic, rather than a geomagnetic, change). If this normal magnetic polarity zone is real, then biostratigraphic constraints (dinocysts and calcareous nannofossils: 1.4–1.7 Ma for 116.8–147.65 mbsf; Fig. 14) eliminate the possibility of it being the Jaramillo Subchron (C1r.1n; 0.99–1.07 Ma) or the Cobb Mountain Subchron (C1r.2r–1n; 1.20–1.21 Ma). This normal zone may instead correspond to the Olduvai Subchron (C2n; 1.77–1.95 Ma).

Below pp4(s) in Subunit IIA (170–254 mbsf), magnetic polarity is dominantly normal, with three short zones of reversed polarity at 177–182 mbsf, 206–208 mbsf, and 215–218 mbsf (Fig. 16). This interval may correspond to C3An (5.89–6.57 Ma) or to a composite sequence between C3Bn and C4n (6.94–8.07 Ma), if biostratigraphic constraints of 3.8–7.4 Ma (calcareous nannofossils and dinocysts) for the upper part (170.6–194 mbsf) and 5.9–7.4 Ma (dinocysts) for the lower part (194–263.8 mbsf) are correct (see “Biostratigraphy” section, this chapter). The three short, reversed-polarity zones within the long normal show very shallow negative inclinations (Fig. 17; $-10^\circ \pm 8^\circ$; $N = 8$), indicating overlapping coercivity spectra with a normal polarity overprint on the initial magnetization. This is very different from the relatively steep inclination of negative polarity (Fig. 17; $-38^\circ \pm 17^\circ$; $N = 23$) from above pp4(s), which is rather close to (but still shallower than) the expected inclination of this site ($\sim 58^\circ$). This may indicate that the diagenetic alteration of magnetic minerals persisted through the normal polarity period, especially within the glauconite-rich silty clay interval at ~ 152 –225 mbsf (see “Lithostratigraphy” section, this chapter).

Rock Magnetism

Table 9 shows the paleomagnetic and rock magnetic results from discrete-cube samples. In Figure 19, NRM after 20-mT demagnetization, susceptibility of ARM (K_{arm}), volume magnetic susceptibility (K), K_{arm}/K , and median destructive field (MDF) of Hole 1072A are plotted vs. relative peak intensities of pyrite and siderite as determined by XRD analysis (see “Lithostratigraphy” section, this chapter). As with Site 1071 (see “Paleomagnetism” section, “Site 1071” chapter, this volume), the magnetic mineral is assumed to be magnetite, on the basis of rock magnetic results reported from Leg 150 (Urbat, 1996). From the top of the hole to 58 mbsf (Subunit IA/IB), rock magnetic parameters fluctuate. Magnetization intensity is moderately high, between 10 and 50 mA/m, with a few exceptions: K_{arm} ranges from 1×10^{-3} to 6×10^{-3} SI, and K from 3×10^{-4} to 1×10^{-3} SI. K_{arm}/K varies between 1 and 8, and MDF ranges from 20 to 30 mT, both of which indicate a medium- to coarse-grained magnetic mineral.

Between 58 and 152 mbsf (Subunit IC), NRM intensity is ~ 10 mA/m, with exceptions at 58–71 (Subunit IC₁) and 130–150 mbsf (Subunit IC₂). K_{arm} is $\sim 10^{-3}$ SI from 58 to 71 mbsf and 1 – 4×10^{-3} SI

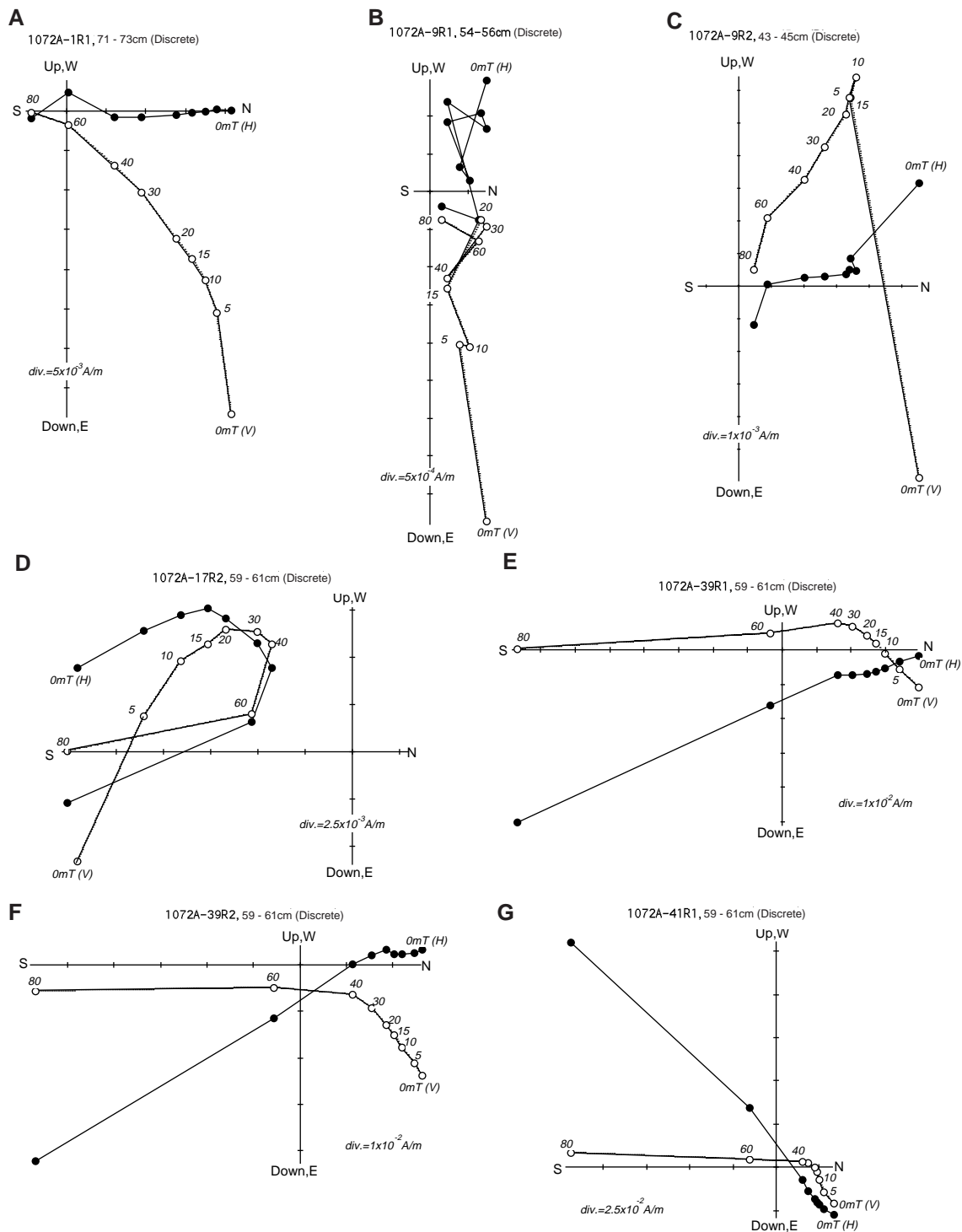


Figure 15. Typical examples of vector endpoint diagrams for discrete samples. Solid circles and open circles represent projections of magnetization vectors onto a horizontal plane and a vertical plane, respectively. Numbers denote demagnetization levels in milliteslas (mT).

for 90–150 mbsf. K is 2×10^{-4} to -1×10^{-3} SI. K_{arm}/K is low (below 2) for 58–72 mbsf, and is ~ 5 for 72–152 mbsf. MDF is generally high (40–50 mT), with low values at the top and bottom of Subunit IC (58–152 mbsf). K_{arm}/K values are consistent with the silty sand lithofacies (see “Lithostratigraphy” section, this chapter), which suggests relatively coarse magnetic grains.

Sediments from the upper part of Subunit IIA (152–225 mbsf) show strong NRM intensity (20–100 mA/m), high K_{arm} (3×10^{-3} to 1

$\times 10^{-2}$ SI), and high K (7×10^{-4} to 6×10^{-3} SI), which indicates high concentrations of magnetic minerals. For this interval, K_{arm}/K is high (5–8) and shows the highest value (~ 10) at the bottom (220–225 mbsf). MDF is also high, between 20 and 50 mT, and shows a downward-decreasing trend. These data indicate the dominance of a fine-grained, single-domain magnetite. From 225 mbsf down to the bottom of Subunit IIA (255 mbsf), magnetic concentration parameters (NRM, K_{arm}) show a decreasing trend. K_{arm}/K also shows a decreasing

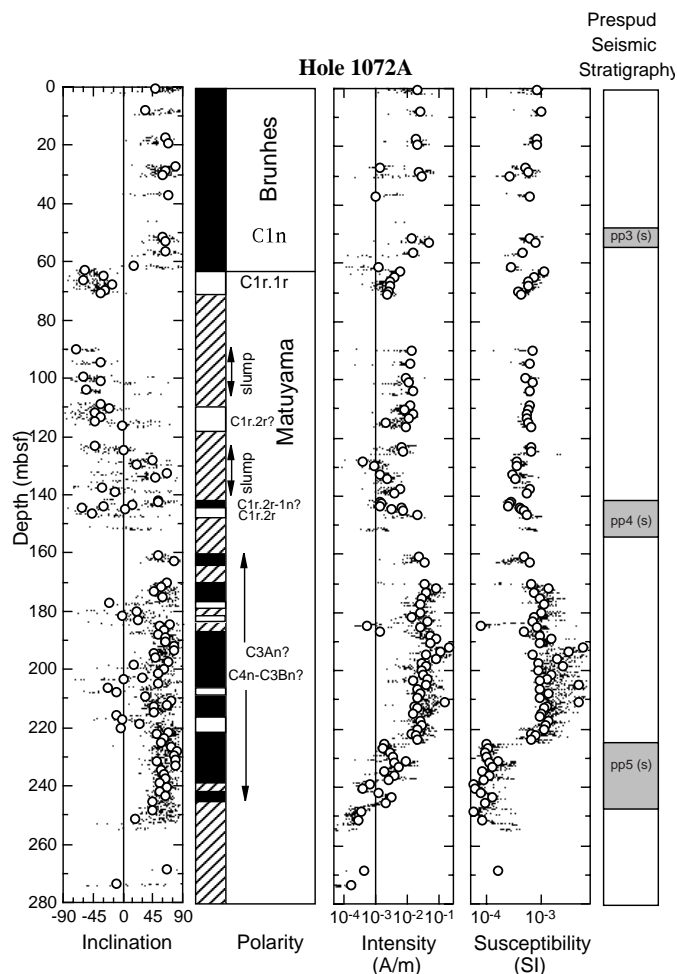


Figure 16. Inclination, magnetic polarity zones, magnetization intensity, and volume magnetic susceptibility for Hole 1072A. Dots and open circles indicate pass-through data and discrete data after 20-mT AF demagnetization, respectively. In the polarity column, black = normal polarity, white = reversed polarity, and cross-hatched = uninterpretable.

ing trend, continuing from the bottom of a silty clay layer at ~237 mbsf, which suggests an increase in magnetic grain size downhole.

INORGANIC GEOCHEMISTRY

Sixteen whole-round samples were taken from Hole 1072A for routine interstitial water analyses. Because we observed low salinity surface seawater at Site 1071, one sample of surface seawater was collected on 30 June in a bucket near the bow of the *JOIDES Resolution* at Site 1072, filtered through a 45- μ m filter, and analyzed for salinity and dissolved species.

Results

Salinity, Cl^- , and K^+ decrease from values near those of average seawater (as defined by the International Association for Physical Sciences of the Ocean [IAPSO]) at the seafloor to minima at 60 mbsf (Fig. 20; Table 10). Concentrations of Ca^{2+} , Mg^{2+} , Sr^{2+} , and SO_4^{2-} decrease from IAPSO values at the seafloor to shallow subsurface minima at ~30 mbsf. As at Site 1071, rates of decrease in uppermost sediments are significantly different for various dissolved species. Cl^- decreases by 16% to 469 mM, Sr^{2+} by 33% to 58 μM , Mg^{2+} by 42% to 31.63 mM, Ca^{2+} by 68% to 3.34 mM, K^+ by 70% to 3.14 mM, and

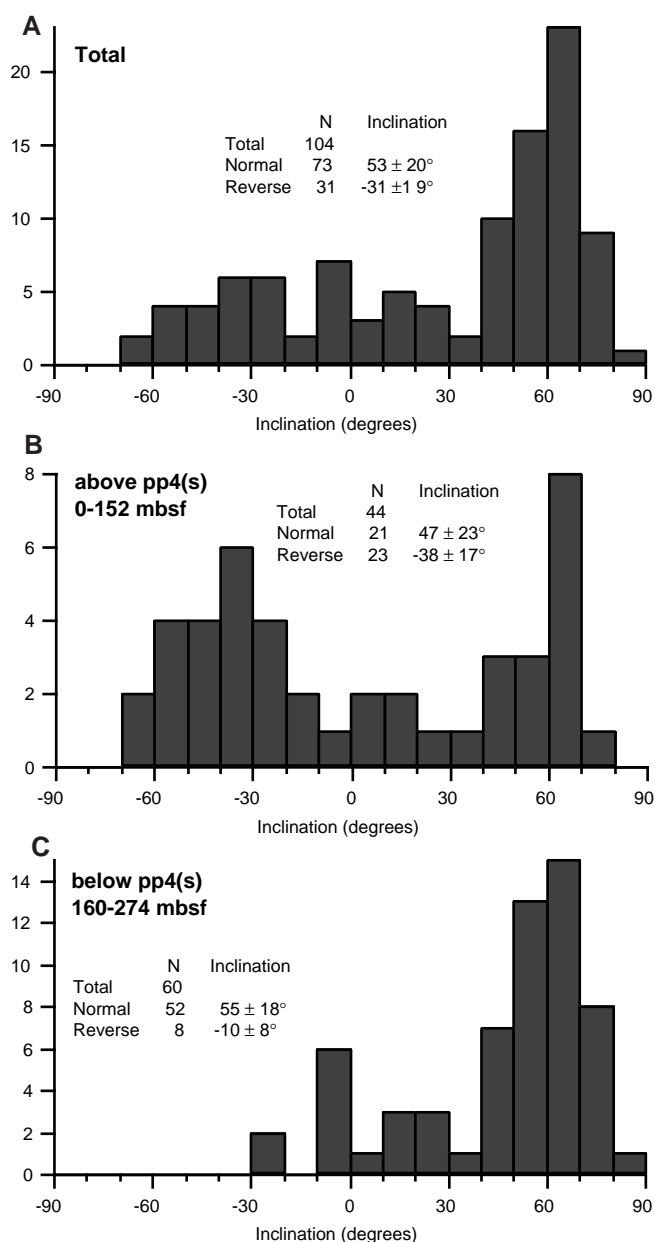


Figure 17. Histograms of inclinations measured on discrete cube samples after AF demagnetization at 20 mT for (A) total samples, (B) samples above pp4(s), and (C) samples below pp4(s).

SO_4^{2-} by 96% to 1.15 mM. In contrast, alkalinity, HPO_4^{2-} , and NH_4^+ increase to local maxima of 8.28 mM, 12.7 μM , and 1.5 mM, respectively, at ~30 mbsf.

Below the shallow subsurface minima, there is a general increase in salinity, Cl^- , Ca^{2+} , K^+ , Mg^{2+} , and Sr^{2+} with depth to the bottom of the hole. Salinity, measured by refractive index, increases to 33.5 (96% of IAPSO), Cl^- to 569 mM (102% of IAPSO), Sr^{2+} to 70 μM (80% of IAPSO), Mg^{2+} to 38.11 mM (69% of IAPSO), Ca^{2+} to 6.45 mM (61% of IAPSO), and K^+ to 8.62 mM (83% of IAPSO). Downhole profiles of alkalinity, NH_4^+ , HPO_4^{2-} , and SO_4^{2-} are more complex at depth. Between 50 and 95 mbsf, alkalinity, NH_4^+ , HPO_4^{2-} , and SO_4^{2-} are at approximately median concentrations for Site 1072 of 7 mM, 1.5 μM , 1.5 μM , and 8 mM, respectively. An exception to this trend is the relatively high HPO_4^{2-} concentration (6.5 μM) at 63.9 mbsf. Between 95 and 150 mbsf, alkalinity and HPO_4^{2-} concentra-

Table 8. Polarity chrons identified for Site 1072.

Depth (mbsf)	Polarity	Polarity chron	Age (Ma)
0.0-62.3	N	C1n (Brunhes)	0.0-0.78
62.3-71.1	R	C1r.1r	0.78-(0.99)
108.4-116.6	R	C1r.2r?	(1.07-1.77)?
141.8-144.0	N?	C1r.2r-1n?	(1.20-1.21)?
144.0-147	R	C1r.2r	(1.07-1.77)
170-254	N (3 short R?)	C3An?/C4n-C3Bn?	

Note: N = normal, R = reversed, ? = uncertain.

Hole 1072A (20mT)

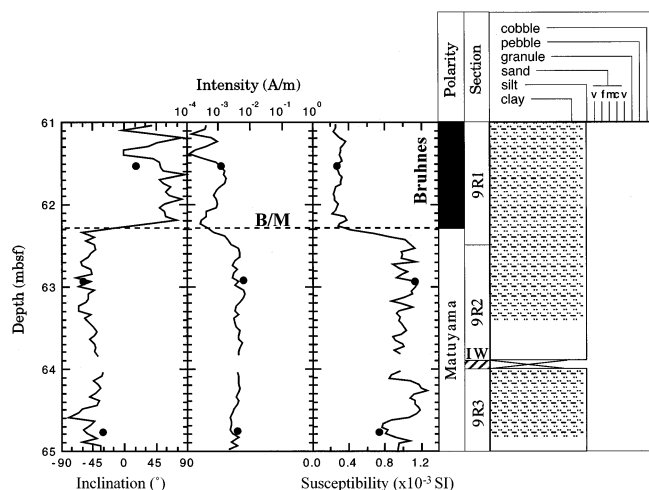


Figure 18. Inclinometer and intensity after AF demagnetization at 20 mT, and magnetic susceptibility plotted vs. depth for the Brunhes/Matuyama (B/M) polarity boundary of Hole 1072A. Solid lines show pass-through data and solid circles represent discrete data, respectively. Polarity column, section names, and simplified lithostratigraphy are shown on the right-hand side. Cross-hatched zone indicates a measurement gap where a whole-round interstitial water sample (IW) was taken.

tions are uniformly low (≤ 4.3 mM and 1.0 μ M, respectively), NH_4^+ concentrations are relatively constant but elevated (~ 1.5 mM), and SO_4^{2-} concentrations decrease to near zero. Below 150 mbsf, alkalinity, NH_4^+ , and HPO_4^{2-} concentrations increase significantly to values of 19.84 mM, 2.9 mM, and 15.9 μ M, respectively, at the bottom of the sampled hole. The increases in NH_4^+ and HPO_4^{2-} begin at greater depths than the increase in alkalinity.

A notable exception to aforementioned downhole profiles is observed in Sample 174A-1072A-27R-1, 115–118 cm (152.05 mbsf), a depth equivalent to the lithostratigraphic boundary between Subunits IC and IIA (Fig. 20; Table 10) and the top of a 1.2-m interval of glauconitic sand (see “Lithostratigraphy” section, this chapter). Relative to pore water from surrounding depths, concentrations of K^+ (18.48 mM) and H_4SiO_4 (773 μ M) are greatly elevated, Ca^{2+} (7.29 mM), SO_4^{2-} (3.46 mM), and NH_4^+ (2.0 mM) are moderately higher, and Cl^- (528 mM) and Mg^{2+} (26.24 mM) are significantly lower.

Preliminary Interpretations

Shallow Salinity Minimum

The salinity minimum is a nonequilibrium feature likely caused by large-amplitude oscillations in the salinity of overlying water. Freshwater has access to the sediment column during glacial stages/sea-level lowstands, whereas seawater covers the sediment column

during interglacial stages/sea-level highstands. The salinity minimum at Site 1072 is less pronounced and ~ 30 m deeper than the minimum at Site 1071. This difference may reflect elevation offset between the two locations during the last transgression.

Diagenesis

Decreases in SO_4^{2-} , with corresponding increases in alkalinity, NH_4^+ , and HPO_4^{2-} , exist over two distinct intervals of the sediment column (at 30 mbsf, associated with the shallow salinity minimum, and below 150 mbsf). We attribute these changes to organic-matter diagenesis. Upper and lower zones of significant bacterial degradation of organic matter were observed over similar depth intervals at Site 1071. However, changes in pore-water concentrations are more pronounced at Site 1072, suggesting higher overall rates of organic-matter diagenesis. In particular, SO_4^{2-} drops to 1 mM in the upper zone at Site 1072, but only to 6 mM at Site 1071. Despite nearly complete SO_4^{2-} reduction over two depth intervals at Site 1072, methane in headspace gas samples is at or near the detection limit, with the exception of three gas samples near 30 mbsf (see “Organic Geochemistry” section, this chapter). The multiple subsurface maxima of alkalinity, NH_4^+ , and HPO_4^{2-} are attributed to lithologic variations at Site 1071. Coincident depth zones of organic-matter diagenesis at Sites 1071 and 1072 may support this interpretation.

The upper zone of increased alkalinity (centered around 30 mbsf) coincides with decreased Mg^{2+} and Ca^{2+} , as well as elevated (relative to seawater) $\text{Mg}^{2+}/\text{Ca}^{2+}$. These pore-water changes are consistent with precipitation of dolomite; X-ray diffraction analyses indicate that dolomite is most abundant in the upper 60 mbsf (see “Lithostratigraphy” section, this chapter). The fairly constant Mg^{2+} profile across the lower alkalinity maximum suggests that dolomite precipitation is not occurring below 150 mbsf, at least at present. Again, this interpretation is consistent with X-ray diffraction analyses (see “Lithostratigraphy” section, this chapter). Siderite abundance increases abruptly below 152 mbsf and corresponds with the lower depth zone of relatively high alkalinity and low SO_4^{2-} (see “Lithostratigraphy” section, this chapter). Formation of siderite is enhanced under these chemical conditions (e.g., Mozley and Burns, 1993; Hicks et al., 1996).

Profiles of most dissolved species display an excursion at 152.05 mbsf, an interval of dusky green to greenish black glauconite sand approximately equivalent to the Subunit IC/IIA lithostratigraphic boundary, which is near sequence boundary pp4(s) (see “Seismic Stratigraphy” section, this chapter). In particular, K^+ and H_4SiO_4 concentrations increase markedly, whereas Mg^{2+} concentrations decrease significantly. The association between high values of K^+ and H_4SiO_4 and glauconitic sand may indicate dissolution (or recrystallization) of glauconite at 152.05 mbsf. Increases in pore-water iron, K^+ , and H_4SiO_4 are also coincident with the presence of glauconite sand at nearby ODP Site 903 (Mountain, Miller, Blum, et al., 1994).

ORGANIC GEOCHEMISTRY

Shipboard organic geochemical studies of cores from Hole 1072A included monitoring of hydrocarbon gases, carbonate carbon and total organic carbon, total sulfur, and total nitrogen contents, and a few Rock-Eval pyrolysis assays. Procedures are summarized in the “Explanatory Notes” chapter (this volume).

Volatile Gases from Sediments

All cores recovered from Holes 1072A were monitored for the presence of gaseous hydrocarbons by the headspace gas technique. Only in Cores 174A-1072A-3R through 5R was methane (C_1) detected at levels above background (5–10 parts per million by volume [ppmv]). Section 174A-1072A-3R-2 (17.0 mbsf) contained 376

Table 9. Paleomagnetic and rock magnetic parameters for discrete cube samples from Hole 1072A.

Core, section, interval (cm)	Depth (mbsf)	NRM		NRM at 20 mT		MDF (mT)	Susceptibility (SI)	K _{arm} (SI)
		Intensity (A/m)	Declination	Inclination	Intensity (A/m)			
174A-1072A-1R-1, 71-73	0.71	4.35E-02	1.7	49.4	2.11E-02	19	8.50E-04	4.24E-03
2R-1, 59-61	8.09	4.58E-02	63.9	33.6	2.63E-02	24	1.01E-03	3.28E-03
3R-1, 15-17	17.15	3.35E-02	68.0	63.3	1.98E-02	24	8.39E-04	4.44E-03
3R-2, 63-65	19.13	3.56E-02	11.4	69.1	2.18E-02	25	8.09E-04	4.24E-03
4R-1, 59-61	27.29	9.38E-03	64.8	78.1	1.50E-03	3	5.01E-04	3.38E-04
4R-2, 59-61	28.79	3.77E-02	17.7	63.7	2.37E-02	37	5.65E-04	1.30E-03
4R-3, 60-62	30.30	3.72E-02	340.5	59.1	2.98E-02	47	2.67E-04	1.43E-03
5R-1, 77-79	37.07	4.18E-03	316.8	67.8	1.02E-03	5	6.20E-04	5.50E-04
7R-1, 59-61	51.59	2.57E-02	319.1	60.0	1.45E-02	23	6.12E-04	4.16E-03
7R-2, 49-51	52.99	7.51E-02	42.1	64.2	4.98E-02	28	7.76E-04	6.14E-03
8R-1, 59-61	56.59	2.56E-02	143.5	63.3	1.62E-02	28	4.58E-04	2.57E-03
9R-1, 54-56	61.54	4.66E-03	302.9	16.8	1.29E-03	4	2.77E-04	6.00E-04
9R-2, 43-45	62.93	8.65E-03	353.4	-58.1	6.24E-03	36	1.14E-03	1.15E-03
9R-3, 77-79	64.77	7.61E-03	244.5	-29.8	3.94E-03	20	7.43E-04	7.55E-04
10R-1, 67-69	66.37	4.15E-03	96.3	-59.7	2.85E-03	37	5.64E-04	5.64E-04
10R-2, 70-72	67.90	4.79E-03	160.3	-16.4	2.97E-03	47	5.88E-04	6.14E-04
10R-3, 81-83	69.51	3.59E-03	91.8	-26.6	2.74E-03	40	3.85E-04	5.51E-04
11R-1, 17-19	70.87	3.01E-03	188.0	-34.3	2.46E-03	42	4.32E-04	5.91E-04
15R-1, 56-58	90.26	6.34E-03	217.9	-69.7	1.43E-02	50	7.08E-04	3.90E-03
16R-1, 56-58	94.56	1.54E-02	283.5	-32.6	1.31E-02	40	6.05E-04	2.49E-03
17R-1, 59-61	99.59	6.60E-03	93.5	-59.3	9.36E-03	40	5.01E-04	3.01E-03
17R-2, 59-61	101.09	1.63E-02	226.5	-33.5	1.17E-02	42	6.77E-04	4.23E-03
18R-1, 59-61	103.99	9.53E-03	126.8	-54.6	1.54E-02	50	6.18E-04	3.40E-03
19R-1, 59-61	108.99	1.30E-02	266.2	-32.7	1.28E-02	50	6.09E-04	3.09E-03
19R-2, 59-61	110.49	1.05E-02	307.9	-21.4	8.95E-03	42	5.68E-04	2.41E-03
19R-3, 59-61	111.99	1.36E-02	232.8	-42.8	1.57E-02	50	5.32E-04	2.22E-03
20R-1, 59-61	113.49	8.62E-03	272.9	-33.6	1.12E-02	41	5.30E-04	2.21E-03
20R-2, 59-61	114.99	1.03E-02	41.4	-42.5	2.26E-03	5	5.76E-04	2.75E-03
20R-3, 59-61	116.49	1.17E-02	281.8	-1.3	9.75E-03	42	6.42E-04	2.52E-03
21R-1, 56-58	122.96	3.72E-03	207.0	-42.9	7.15E-03	0	6.52E-04	2.15E-03
21R-2, 59-61	124.49	8.89E-03	272.5	1.6	7.76E-03	40	6.61E-04	2.30E-03
22R-1, 57-59	127.97	6.25E-03	334.9	43.9	3.95E-04	3	3.54E-04	1.31E-03
22R-2, 68-70	129.58	4.15E-03	188.5	20.5	8.96E-04	4	3.57E-04	1.39E-03
23R-1, 59-61	132.49	5.32E-03	178.0	66.7	1.48E-03	8	2.95E-04	1.75E-03
23R-2, 59-61	133.99	5.19E-03	290.5	48.8	2.35E-03	17	3.42E-04	1.85E-03
24R-1, 59-61	137.49	6.03E-03	269.5	-30.8	6.08E-03	20	6.16E-04	2.44E-03
24R-2, 59-61	138.99	5.36E-03	247.5	-11.4	4.04E-03	42	5.32E-04	2.75E-03
25R-1, 65-67	141.95	4.36E-03	76.7	53.6	1.43E-03	10	2.69E-04	1.50E-03
25R-1, 122-124	142.52	3.51E-03	52.3	53.7	1.53E-03	16	2.61E-04	1.44E-03
25R-2, 59-61	143.39	3.43E-03	107.4	15.1	1.48E-03	14	2.38E-04	1.20E-03
25R-2, 120-122	144.00	8.14E-03	353.4	-29.8	7.07E-03	46	3.92E-04	1.61E-03
25R-3, 37-39	144.67	2.18E-03	222.9	-61.0	3.23E-03	40	4.16E-04	1.90E-03
25R-3, 58-60	144.88	9.83E-03	316.8	3.7	7.46E-03	38	4.73E-04	2.54E-03
26R-1, 14-16	146.44	1.92E-02	296.5	-46.6	2.11E-02	60	5.27E-04	2.16E-03
29R-1, 59-61	160.89	3.09E-02	51.2	53.7	2.35E-02	36	4.77E-04	3.41E-03
29R-2, 80-82	162.60	4.66E-02	77.4	77.7	3.63E-02	43	6.22E-04	4.70E-03
31R-1, 59-61	170.39	5.28E-02	334.9	66.1	3.67E-02	36	6.51E-04	4.21E-03
31R-2, 59-61	171.89	1.11E-01	6.0	57.3	8.34E-02	40	1.35E-03	9.80E-03
31R-3, 56-58	173.36	4.99E-02	57.0	47.2	4.04E-02	45	7.16E-04	4.21E-03
32R-1, 54-56	175.34	4.27E-02	12.6	58.7	2.86E-02	32	9.62E-04	6.10E-03
32R-2, 59-61	176.89	3.09E-02	20.3	-20.2	2.59E-02	48	1.15E-03	7.12E-03
33R-1, 59-61	179.89	4.58E-02	323.6	19.9	2.61E-02	27	9.96E-04	6.70E-03
33R-2, 59-61	181.39	1.67E-02	326.6	-1.3	1.42E-02	0	7.26E-04	5.21E-03
33R-3, 53-55	182.83	5.70E-02	351.3	23.3	4.46E-02	43	7.01E-04	5.55E-03
33R-4, 51-53	184.31	6.65E-04	116.1	69.4	5.35E-04	44	7.57E-05	2.15E-04
34R-1, 58-60	184.88	4.36E-02	38.3	54.8	2.79E-02	30	8.41E-04	5.72E-03
34R-2, 78-80	186.58	6.10E-03	168.0	62.2	1.44E-03	10	4.88E-04	2.99E-03
34R-3, 56-58	187.86	7.82E-02	274.7	53.3	5.36E-02	34	9.62E-04	6.94E-03
35R-1, 59-61	189.19	1.04E-01	302.8	64.2	8.29E-02	43	1.55E-03	9.34E-03
35R-2, 59-61	190.69	7.03E-02	335.8	64.8	5.35E-02	42	9.36E-04	7.85E-03
35R-3, 59-61	192.19	4.37E-01	8.6	77.4	2.26E-01	22	5.83E-03	3.93E-02
35R-4, 23-25	193.33	1.94E-01	88.6	77.0	1.23E-01	31	3.23E-03	2.12E-02
36R-1, 59-61	194.19	5.94E-02	23.3	46.9	4.13E-02	38	6.74E-04	3.45E-03
36R-2, 59-61	195.69	1.31E-01	350.4	47.8	8.46E-02	33	1.93E-03	1.19E-02
36R-3, 59-61	197.19	4.24E-02	218.4	69.0	3.12E-02	38	8.92E-04	6.41E-03
37R-1, 59-61	198.49	7.51E-02	343.0	15.9	4.00E-02	23	2.52E-03	1.38E-02
37R-2, 59-61	199.99	3.85E-02	46.6	62.1	3.00E-02	0	9.11E-04	6.26E-03
37R-3, 59-61	201.49	4.73E-02	350.3	54.0	3.17E-02	35	1.53E-03	9.13E-03
37R-4, 60-62	203.00	6.42E-02	343.6	28.2	4.74E-02	40	1.29E-03	8.61E-03
38R-1, 59-61	203.49	2.52E-02	342.7	1.2	1.61E-02	33	9.57E-04	6.74E-03
38R-2, 59-61	204.99	1.55E-01	341.8	52.1	4.25E-02	8	4.86E-03	2.49E-02
38R-3, 59-61	206.49	2.44E-02	9.0	-23.4	2.19E-02	48	9.14E-04	6.79E-03
39R-1, 59-61	207.89	4.09E-02	15.7	-9.4	2.59E-02	37	1.37E-03	9.03E-03
39R-2, 59-61	209.39	3.55E-02	349.2	34.4	2.29E-02	31	9.64E-04	6.10E-03
39R-3, 62-64	210.92	3.54E-01	24.5	72.0	1.63E-01	18	4.79E-03	4.13E-02
39R-4, 58-60	212.38	2.96E-02	319.7	65.4	1.70E-02	24	1.29E-03	8.41E-03
40R-1, 53-55	212.83	3.33E-02	336.0	45.6	2.16E-02	40	1.15E-03	7.16E-03
40R-2, 66-68	214.46	2.73E-02	304.9	46.6	1.60E-02	28	1.01E-03	5.23E-03
40R-3, 48-50	215.78	2.66E-02	291.0	-8.9	2.27E-02	42	9.35E-04	6.70E-03
41R-1, 59-61	217.29	4.76E-02	39.1	-0.8	2.83E-02	28	1.33E-03	6.65E-03
41R-2, 59-61	218.79	5.22E-02	7.4	25.8	2.92E-02	25	1.21E-03	1.13E-02
41R-3, 59-61	220.29	4.38E-02	52.1	-3.9	2.17E-02	20	1.12E-03	1.29E-02
41R-4, 59-61	221.79	2.28E-02	106.2	69.0	1.43E-02	30	6.38E-04	6.26E-03
42R-1, 61-63	222.31	4.20E-02	357.6	51.4	1.91E-02	17	7.76E-04	8.11E-03
42R-2, 59-61	223.79	3.58E-02	100.0	61.6	2.18E-02	29	6.42E-04	7.44E-03
42R-3, 59-61	225.29	3.68E-03	39.1	56.5	2.06E-03	31	9.73E-05	7.72E-04

Table 9 (continued).

Core, section, interval (cm)	Depth (mbsf)	NRM		NRM at 20 mT		MDF (mT)	Susceptibility (SI)	K _{arm} (SI)
		Intensity (A/m)	Declination	Inclination	Intensity (A/m)			
43R-1, 59-61	226.69	2.65E-03	248.1	72.8	1.75E-03	27	1.05E-04	6.36E-04
43R-2, 59-61	228.19	4.94E-03	50.8	80.6	2.83E-03	26	9.46E-05	8.05E-04
43R-3, 59-61	229.69	6.27E-03	59.7	76.6	3.56E-03	27	9.86E-05	7.88E-04
43R-4, 59-61	231.19	1.43E-02	213.0	78.4	9.91E-03	34	1.55E-04	1.96E-03
44R-1, 59-61	231.69	5.92E-03	298.5	51.9	4.21E-03	36	1.11E-04	1.06E-03
44R-2, 59-61	233.19	7.43E-03	45.3	78.7	5.35E-03	38	1.26E-04	1.12E-03
44R-3, 59-61	234.69	2.50E-03	81.9	58.1	1.88E-03	35	8.11E-05	4.83E-04
45R-1, 59-61	236.09	6.01E-03	280.7	61.1	4.30E-03	37	1.08E-04	9.40E-04
45R-2, 61-63	237.61	3.99E-03	50.9	63.7	2.78E-03	40	8.51E-05	6.92E-04
45R-3, 60-62	239.10	8.83E-04	336.6	55.9	6.71E-04	27	5.68E-05	1.84E-04
45R-4, 59-61	240.59	7.47E-04	108.0	66.4	3.90E-04	22	5.94E-05	2.18E-04
45R-5, 59-61	242.09	1.81E-03	16.2	56.0	1.28E-03	28	7.57E-05	4.51E-04
45R-6, 59-61	243.59	4.52E-03	62.9	63.1	3.28E-03	46	1.27E-04	9.82E-04
46R-1, 63-65	245.33	2.54E-03	12.7	44.4	2.20E-03	37	9.46E-05	3.82E-04
46R-3, 59-61	248.29	7.44E-04	96.7	44.7	3.84E-04	31	5.81E-05	1.08E-04
46R-5, 59-61	251.29	6.53E-04	219.0	17.9	2.96E-04	15	7.97E-05	1.17E-04
49R-1, 7-9	268.78	7.99E-04	24.5	65.6	4.29E-04	21	1.61E-04	0.00E+00
50R-1, 46-48	273.76	1.80E-04	150.2	-10.0	1.85E-04	0	0.00E+00	3.27E-05

Note: MDF = median destructive field, K_{arm} = susceptibility of ARM.

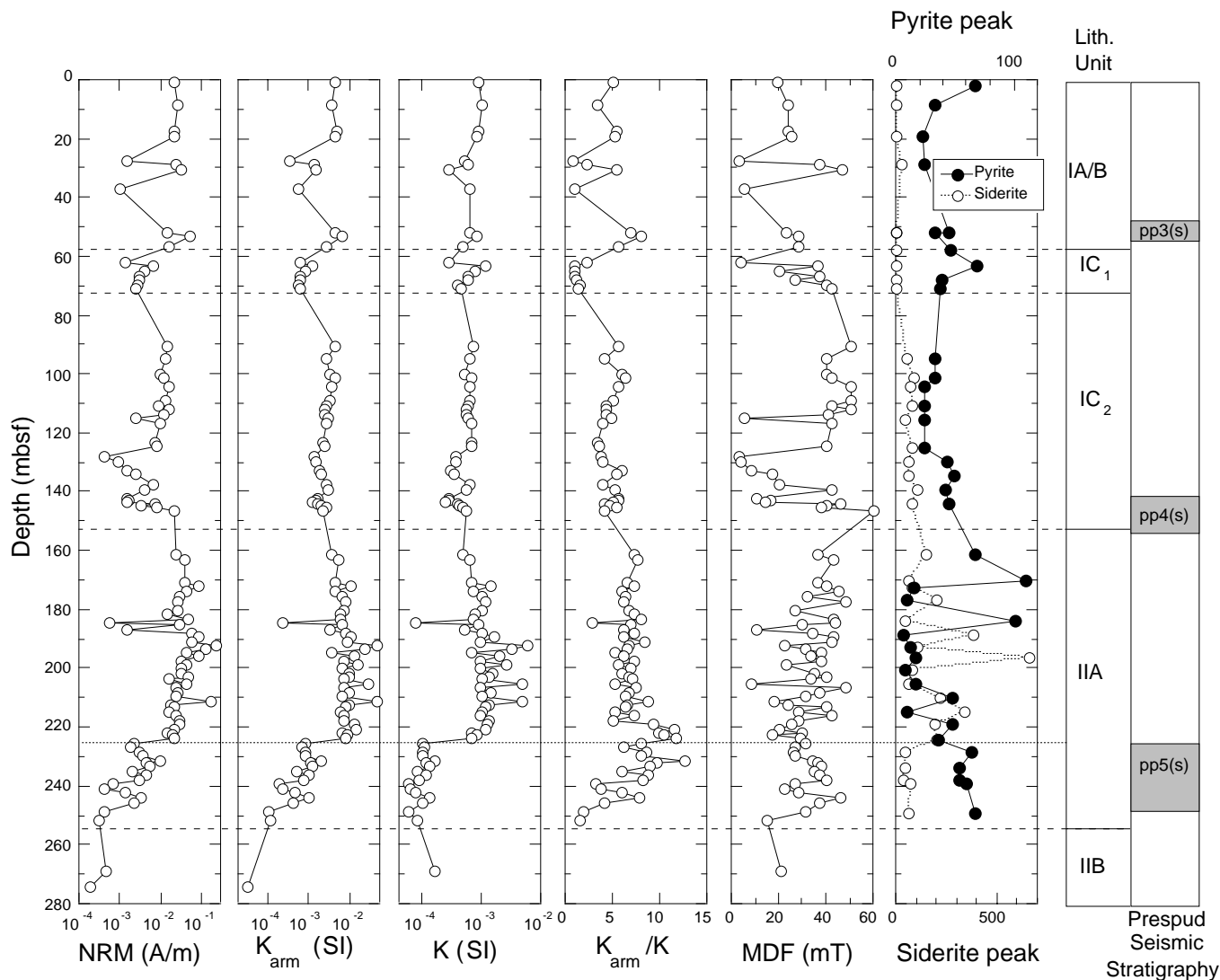


Figure 19. Rock magnetic properties plotted vs. depth for Hole 1072A. Natural remanent magnetization (NRM) after 20 mT demagnetization, ARM susceptibility (K_{arm}), susceptibility (K), K_{arm}/K, and median destructive field (MDF) from left to right. Relative peak intensities of pyrite and siderite identified from XRD analysis are also plotted at right. Depth ranges to seismic surfaces are those predicted on the basis of Oc270 seismic velocity data (see “Seismic Stratigraphy” section, this chapter).

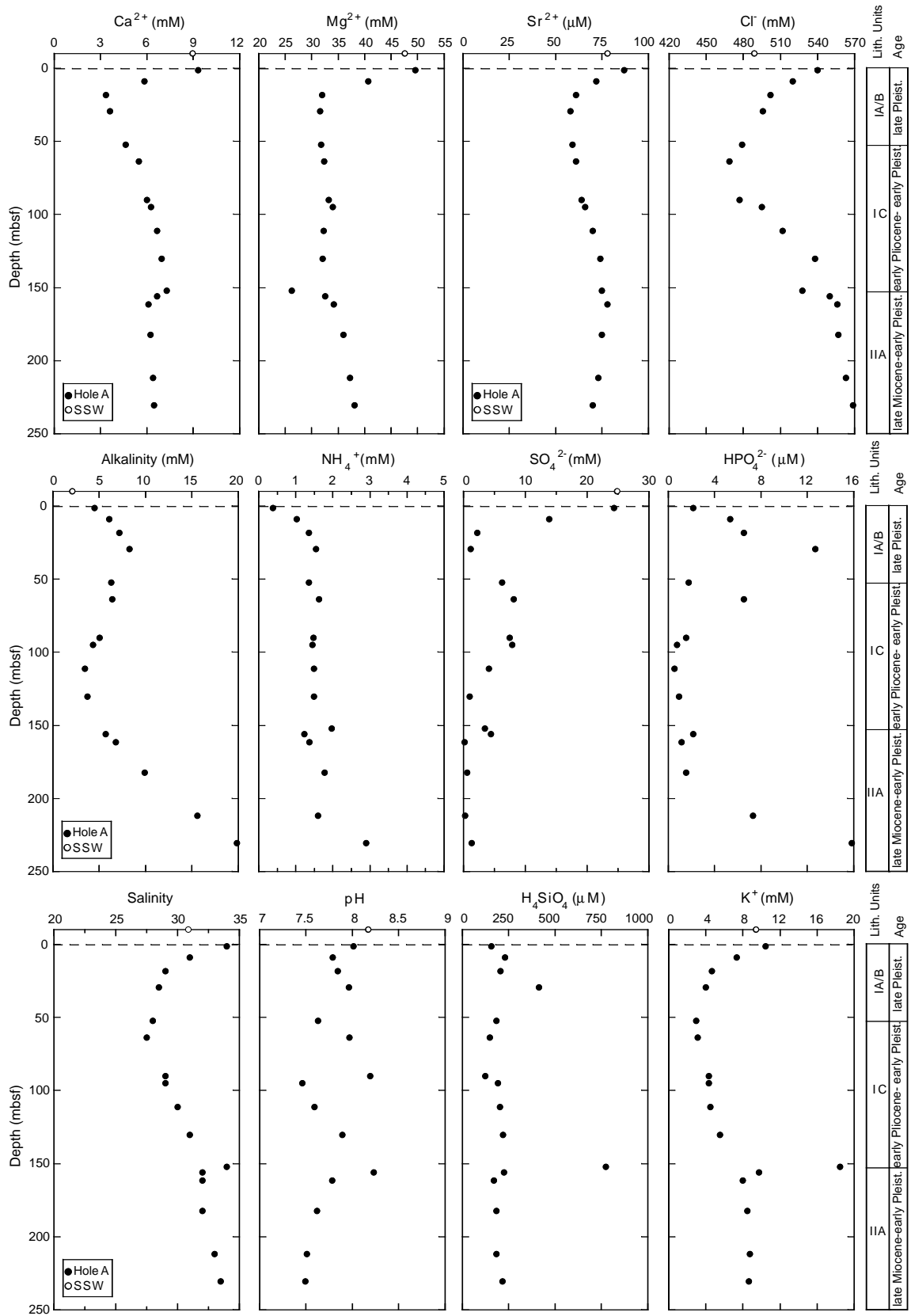


Figure 20. Concentration-depth profiles of interstitial water at Hole 1072A with approximate lithostratigraphic boundaries and corresponding ages (see “Lithostratigraphy” and “Biostratigraphy” sections, this chapter). Dashed lines at 0 mbsf represent the seafloor. Open circles, plotted an arbitrary distance above the seafloor, represent analyses of surface seawater.

Table 10. Interstitial water data from Hole 1072A.

Core, section, interval (cm)	Depth (mbsf)	pH	Alkalinity (mM)	Salinity	Cl ⁻ (mM)	SO ₄ ²⁻ (mM)	NH ₄ ⁺ (mM)	HPO ₄ ²⁻ (μM)	Sr ²⁺ (μM)	Mg ²⁺ (mM)	Ca ²⁺ (mM)	K ⁺ (mM)	H ₄ SiO ₄ (μM)
174A-1072A-													
1R-1, 134-144	1.34	8.01	4.51	34.0	540	24.38	0.4	2.1	87	49.60	9.31	10.44	157
2R-1, 140-150	8.90	7.79	6.09	31.0	520	13.88	1.0	5.3	72	40.63	5.85	7.33	231
3R-1, 140-150	18.40	7.84	7.17	29.0	502	2.20	1.4	6.5	61	32.00	3.34	4.65	206
4R-2, 140-150	29.60	7.96	8.29	28.5	496	1.15	1.5	12.7	58	31.63	3.62	3.97	414
7R-1, 140-150	52.40	7.63	6.32	28.0	479	6.20	1.4	1.7	59	31.82	4.63	2.95	184
9R-2, 140-150	63.90	7.97	6.43	27.5	469	8.17	1.6	6.5	61	32.37	5.48	3.14	148
15R-1, 33-43	90.03	8.19	5.04	29.0	477	7.51	1.5	1.5	64	33.22	6.01	4.32	123
16R-1, 104-114	95.04	7.46	4.31	29.0	495	7.91	1.5	0.8	66	33.98	6.28	4.33	191
19R-2, 140-150	111.30	7.59	3.46	30.0	512	4.08	1.5	0.6	70	32.23	6.66	4.49	201
22R-2, 140-150	130.30	7.89	3.71	31.0	538	0.99	1.5	1.0	74	32.06	6.97	5.55	218
27R-1, 115-118	152.05	NM	NM	34.0	528	3.46	2.0	NM	75	26.24	7.29	18.48	773
28R-CC, 0-5	155.90	8.23	5.70	32.0	550	4.47	1.2	2.1	NM	32.52	6.65	9.73	225
29R-1, 140-150	161.70	7.78	6.78	32.0	556	0.18	1.4	1.1	78	34.16	6.12	7.96	170
33R-1, 140-150	182.20	7.62	9.91	32.0	557	0.58	1.8	1.5	75	35.96	6.24	8.48	182
39R-3, 140-150	211.70	7.51	15.61	33.0	563	0.24	1.6	7.3	73	37.24	6.39	8.73	182
43R-1, 140-150	230.50	7.49	19.84	33.5	569	1.33	2.9	15.9	70	38.11	6.45	8.62	216
SSW	NA	8.2	2.09	30.5	489	24.82	NM	NM	78	47.58	8.97	9.39	NM
IAPSO	NA	NA	NA	35.0	559	28.90	NA	NA	87	54.00	10.55	10.44	NA

Notes: NM = not measured. SSW = surface seawater. IAPSO = International Association for the Physical Sciences of the Ocean. NA = not applicable.

ppmv methane, Section 4R-2 (26.7 mbsf) contained 1056 ppmv, and Section 5R-1 (36.3 mbsf) contained 289 ppmv. Cores deeper than 36 mbsf contained 5 ppmv or less methane.

The highest observed headspace methane content (1056 ppmv in Section 174A-1072A-4R-2) is equivalent to a dissolved CH₄ concentration of ~0.3 mM and corresponds with the depth of the shallow minimum in dissolved sulfate (1.2 mM) in the same core. Sulfate reduction apparently has progressed to near completion in the upper 30 m of sediment in Hole 1072A, with the consequent incipient onset of microbial methanogenesis. However, in the interval from 40 to 130 mbsf, sulfate has been replenished (or was never completely removed), and methanogenesis is inhibited. Methane continues to be absent from cores, even though sulfate is almost completely eliminated at 130 mbsf and is essentially at zero concentration (for rotary cores) from 160 to 230 mbsf. It is unclear whether methane was once present in the deeper sediments of Hole 1072A and has subsequently been vented or oxidized, or if it has never been present in the deeper sediments.

Carbon and Elemental Analyses

Carbonate carbon, total carbon (TC), total organic carbon (TOC, by difference), total nitrogen (TN), and total sulfur (TS) analyses on 36 sediment samples from Site 1072 are reported in Table 11. Organic and carbonate carbon contents are plotted against depth of burial in Figure 21. Carbonate carbon contents are similar to those measured at Site 1071, with relatively high (1–2 wt%) values in Pleistocene shelf sediments at 0–70 mbsf, and lower (0.1–0.5 wt%) values in the sampled intervals down to 250 mbsf. Samples at 196–209 mbsf, which have carbonate carbon contents of 2.65 and 1.18 wt%, may reflect the presence of diagenetic carbonate.

As at Site 1071, organic carbon varies inversely with carbonate carbon in samples from Hole 1072A. There is an increase in organic carbon content with increasing depth, with samples from 0 to 70 mbsf having somewhat lower organic carbon contents (0.1–0.4 wt%) than those from 100 to 250 mbsf (0.3–0.9 wt%).

TN content is consistently at ~1/10 the level of the organic carbon, whereas sulfur is more variable. TS content ranges from 0 to 1.2 wt%, and has no consistent relationship with organic carbon.

Organic-Matter Characterization

Fifteen samples from Hole 1072A were characterized by Rock-Eval pyrolysis (Table 12). Samples with >0.5 wt% organic carbon were selected for analysis. In general, samples from the lower Pleis-

Table 11. Carbon and elemental analyses for sediment samples from Hole 1072A.

Core, section, interval (cm)	Depth (mbsf)	IC (wt%)	CaCO ₃ (wt%)	TC (wt%)	OC (wt%)	TN (wt%)	TS (wt%)
174A-1072A-							
1R-2, 43-44	1.87	1.16	9.62	1.43	0.27	0.056	0.91
2R-1, 69-70	8.19	1.58	13.15	2.42	0.84	0.038	0.33
3R-2, 72-73	19.22	1.41	11.72	1.59	0.18	0.062	0.13
4R-2, 5-6	28.25	2.00	16.64	2.44	0.44	0.064	0.11
7R-1, 68-69	51.68	2.12	17.70	1.97	0.00	0.060	0.20
8R-CC, 5-6	57.55	2.25	18.78	2.59	0.34	0.035	0.00
9R-2, 68-69	63.18	0.85	7.10	1.03	0.18	0.031	0.00
10R-2, 80-81	68.00	1.84	15.29	2.01	0.17	0.037	0.00
11R-1, 14-15	70.84	1.90	15.82	2.19	0.29	0.037	0.08
16R-1, 37-38	94.37	0.49	4.12	0.51	0.01	0.042	0.04
17R-2, 80-81	101.30	0.24	2.01	0.47	0.23	0.039	0.06
18R-1, 86-87	104.26	0.17	1.43	1.00	0.83	0.043	0.09
19R-2, 80-81	110.70	0.15	1.21	1.01	0.86	0.047	0.15
20R-2, 71-72	115.11	0.51	4.28	1.09	0.57	0.044	0.13
21R-2, 80-81	124.70	0.16	1.33	0.32	0.16	0.033	0.07
22R-2, 73-74	129.63	0.28	2.30	0.59	0.31	0.035	0.05
23R-2, 74-75	134.14	0.37	3.11	0.71	0.34	0.047	0.06
24R-2, 74-75	139.14	0.37	3.06	0.68	0.31	0.036	0.18
25R-2, 136-137	144.16	0.41	3.38	0.95	0.54	0.055	0.53
29R-1, 94-95	161.24	0.28	2.33	0.64	0.36	0.029	0.82
31R-2, 89-90	172.19	0.29	2.42	0.89	0.60	0.060	0.10
32R-2, 20-21	176.50	0.63	5.22	1.24	0.62	0.074	0.05
33R-4, 19-20	183.99	0.14	1.19	0.60	0.45	0.046	1.19
34R-3, 92-93	188.22	0.80	6.66	1.36	0.56	0.065	0.09
35R-3, 95-96	192.55	0.26	2.13	0.76	0.50	0.050	0.15
36R-2, 136-138	196.46	1.09	9.09	1.85	0.76	0.065	0.10
37R-2, 80-81	200.20	0.16	1.34	0.75	0.59	0.073	0.30
38R-2, 80-81	205.20	0.15	1.23	0.95	0.80	0.066	0.87
39R-2, 85-86	209.65	1.06	8.87	1.53	0.47	0.052	0.14
40R-2, 87-88	214.67	0.63	5.24	1.23	0.61	0.068	0.68
41R-2, 82-83	219.02	0.44	3.70	0.82	0.38	0.049	0.23
42R-2, 71-72	223.91	0.44	3.66	1.02	0.58	0.054	0.64
43R-2, 80-81	228.40	0.20	1.63	0.58	0.39	0.048	0.60
44R-2, 82-83	233.42	0.18	1.48	0.61	0.43	0.043	0.36
45R-2, 82-83	237.82	0.11	0.92	0.50	0.39	0.044	0.32
46R-3, 141-142	249.11	0.22	1.82	0.97	0.76	0.048	0.59

Note: IC = inorganic carbon, CaCO₃ = calcium carbonate, TC = total carbon, OC = organic carbon, TN = total nitrogen, and TS = total sulfur.

tocene–Miocene section (>100 mbsf) have larger S₂ and Hydrogen Index (HI) values, compared with samples from the upper Pleistocene section (<50 mbsf). The unusually high Oxygen Index (OI) values for Miocene samples are probably an artifact of thermally unstable carbonate (siderite) minerals in deeper samples (see “Lithostratigraphy” section, this chapter). Although there is a general decrease in carbonate carbon with depth, samples with >0.5 wt% organic carbon also have somewhat higher carbonate carbon contents and thus have higher OI values. Except for the shallowest sample, the Pleistocene samples have extremely high T_{max} values, 473°–500°C.

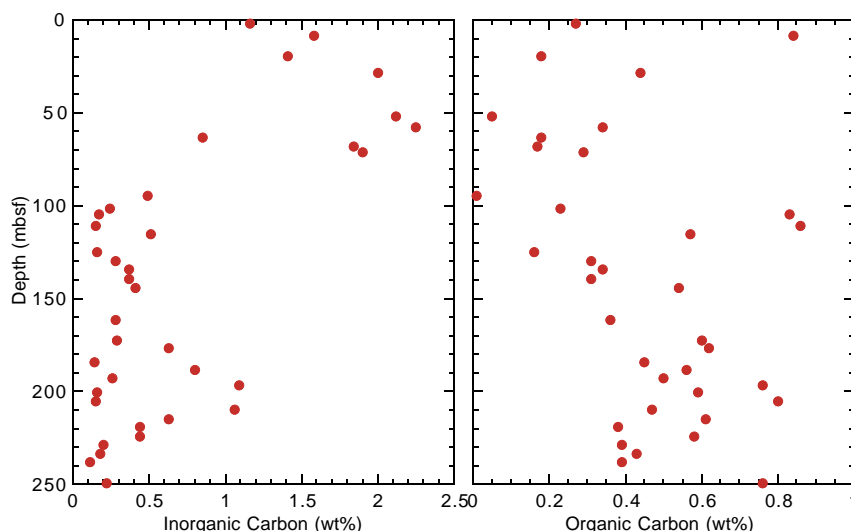


Figure 21. Carbonate carbon and organic carbon content vs. depth for sediment samples from Hole 1072A.

Table 12. Organic carbon and Rock-Eval pyrolysis for selected samples, Hole 1072A.

Core, section, interval (cm)	Depth (mbsf)	OC (wt%)	S ₁ (mg/g)	S ₂ (mg/g)	S ₃ (mg/g)	HI (mg/gC)	OI (mg/gC)	T _{max} (°C)
174A-1072A-								
2R-1, 69-70	8.19	0.84	0.04	0.21	0.65	25	77	391
18R-1, 86-87	104.26	0.83	0.00	0.76	0.61	91	73	500
19R-2, 80-81	110.70	0.86	0.00	0.80	0.71	93	82	491
20R-2, 71-72	115.11	0.57	0.00	0.69	0.55	121	96	495
25R-2,136-137	144.16	0.54	0.04	0.48	1.35	88	250	473
31R-2, 89-90	172.19	0.60	0.04	1.23	2.43	205	405	426
32R-2, 20-21	176.50	0.62	0.04	1.06	5.01	170	808	448
34R-3, 92-93	188.22	0.56	0.07	1.13	6.24	201	1114	417
35R-3, 95-96	192.55	0.50	0.05	0.76	1.60	152	320	454
36R-2,136-138	196.46	0.76	0.03	0.72	5.15	94	677	425
37R-2, 80-81	200.20	0.59	0.05	1.00	1.04	169	176	423
38R-2, 80-81	205.20	0.80	0.06	0.90	0.79	112	98	420
39R-2, 85-86	214.67	0.47	0.05	1.31	4.26	278	906	429
42R-2, 71-72	223.91	0.58	0.06	0.98	2.30	168	396	417
46R-3, 141-142	249.11	0.76	0.03	0.74	1.12	97	147	420

Note: OC = organic carbon, HI = hydrogen index, OI = oxygen index.

Such values are characteristic of organic matter that has been subjected to high-temperature (>150°C) alteration. Examination of pyrograms shows that all Hole 1072A samples analyzed by Rock-Eval have double S₂ peaks. In the Pliocene–Pleistocene section (lithostratigraphic Unit I), the two components of the S₂ peak are subequal, and the Rock-Eval microprocessor picks the maximum of the second S₂ peak as the T_{max} (i.e., the nominal pyrolysis temperature at which the rate of evolution of pyrolysis products is at a maximum). For analyzed samples from the Miocene section (Unit II), the first component of the S₂ peak is always dominant and gives T_{max} values, 417°–429°C, that are more typical of thermally immature organic matter. It appears that two components of organic matter have accumulated in the cored sedimentary succession on the New Jersey shelf. One component is the normal first-cycle organic matter that is preserved in marine sediments and produces the low-temperature part of the Rock-Eval S₂ peak. The other component may be recycled, thermally mature organic matter associated with clastic debris eroded from older rocks exposed on the continent. The primary component is subordinate in the Pleistocene section, but dominant in the deeper Miocene section. The recycled component is present as a relatively constant background of ~0.2 wt% organic carbon.

PHYSICAL PROPERTIES

Introduction

Physical properties data collected at Site 1072 are based on measurements and procedures discussed in the “Explanatory Notes”

chapter (this volume), with the exception that the PWL component of the MST was turned off for all cores. In this section, results of physical properties measurements are presented, trends in the data are discussed, and correlations are made between physical properties and other shipboard measurements.

Density and Porosity

Density measurements at Site 1072 were acquired at a resolution of two per section; the results are presented in Figure 22. For Hole 1072A, we used the gamma-ray attenuation porosity evaluator (GRAPE) component of the MST to estimate whole-core density at a sample spacing of 4 cm (Table 13 on CD-ROM). Outliers were removed from the recorded data by visual inspection; the most common cause of such outliers is gaps in the cores (densities <~1 g/cm³ were removed). Filtering resulted in the removal of ~0.1% of observed data. For cores recovered from Hole 1072A, index properties samples were taken at a nominal spacing of 75 cm (two samples per section). Index properties samples were used to calculate wet, dry, and grain density; porosity; water content; and void ratio (Fig. 22; Table 14 on CD-ROM).

GRAPE density estimates are consistently lower than index properties bulk density measurements, particularly in intervals of low recovery (e.g., 0–38 and 90–95 mbsf [Fig. 22]). This offset is probably the result of incomplete filling of core liners associated with RCB coring. Agreement between GRAPE and index properties densities improves throughout most of the high-recovery interval between 170 and 253 mbsf, which is indicative of reduced drilling disturbance.

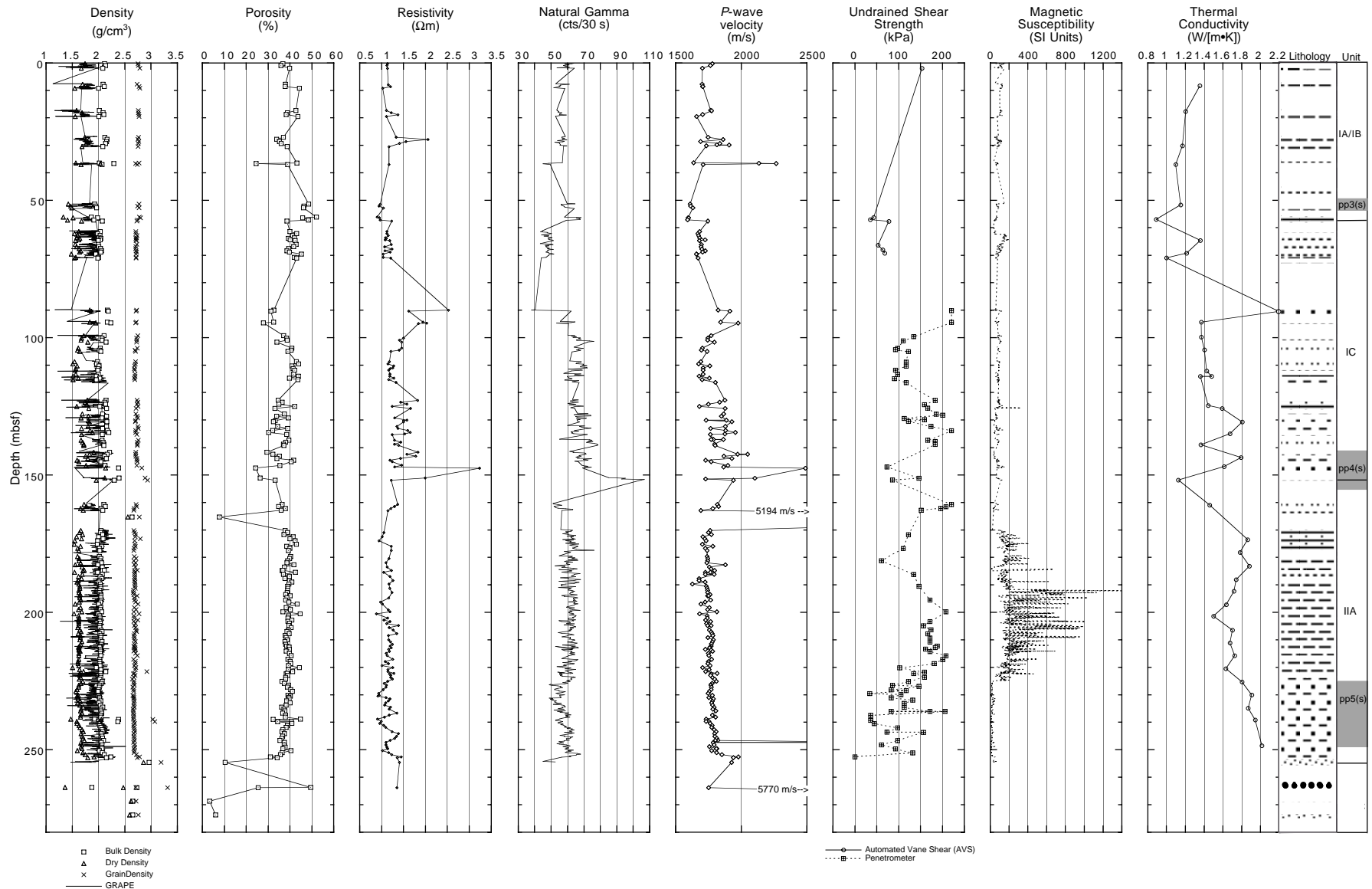


Figure 22. Index properties (IP) and multisensor track (MST) GRAPE density, discrete IP porosity, longitudinal resistivity, natural gamma, PWS3-derived *P*-wave velocity, undrained shear strength, MST magnetic susceptibility, and thermal conductivity measurements from Hole 1072A. Physical properties data are plotted along with a simplified lithologic summary; lithologic symbols are those used in the “Lithostratigraphy” section (this chapter). Only PWS3 *P*-wave velocity measurements (x-direction, orthogonal to core axis) were made. Undrained shear strength measurements were made using the AVS hand-held penetrometer. Depth ranges to seismic surfaces (gray bars on far right) are based upon Oc270 seismic velocity data (see “Seismic Stratigraphy” section, this chapter).

The overall trend of GRAPE densities is that of a slight increase with depth, which is almost certainly linked to improving core condition with depth. In contrast, index properties bulk densities in lithologic Subunit IIA are less than those in overlying Unit I. This follows a similar trend in grain densities.

A narrow peak in index properties bulk density (up to 2.29 g/cm³) is present at ~37 mbsf, in muddy sand recovered in a short core in an otherwise unrecovered interval. A sharp downhole increase in index properties bulk density at ~57 mbsf, which is the boundary between Subunits IA/IB and IC and is close to sequence boundary pp3(s) (see “Lithostratigraphy” and “Seismic Stratigraphy” sections, this chapter), is linked, unusually, to a downhole decrease in grain density. Silty clay overlies clayey silt at this boundary. Index properties bulk density increases downhole from 71 to 90 mbsf, across an uncored interval, to a peak of ~2.23 g/cm³. It declines downhole from 90 to ~115 mbsf, before rising again across another uncored interval between 115 and 123 mbsf. A peak in index properties bulk density of up to ~2.4 g/cm³ is noted between 147 and 151 mbsf. This is the interval of glauconitic sand (see “Lithostratigraphy” section, this chapter), which is near the boundary between Units I and II and pp4(s) (see “Seismic Stratigraphy” section, this chapter), and is also associated with a peak in grain density. This peak is overlain by a thin interval of reduced index properties bulk density and increased porosity (Fig. 22). A higher peak in index properties bulk density (2.64 g/cm³) is present at 165 mbsf in lithified sandstone, just below pp4(s) (see “Seismic Stratigraphy” section, this chapter). Index properties bulk density is fairly constant at 2.0–2.1 g/cm³ downhole from ~170 to 250 mbsf. However, a peak of 2.14 g/cm³, with a grain density of 2.92 g/cm³, is present at ~222 mbsf. Index properties bulk density increases to 2.96 g/cm³ at ~255 mbsf in glauconitic silty sand with possible siderite nodules, near the base of Unit II and in the vicinity of pp5(s) (see “Lithostratigraphy” and “Seismic Stratigraphy” sections, this chapter). Grain density also peaks at this depth, at 3.19 g/cm³. High index properties bulk densities (>2.6 g/cm³) are associated with gravel and lithified sandstones in Subunit IIB, although a lower density (1.87 g/cm³) in an interval of sandy mud attests to the presence of interbedded lithologies in this poorly recovered interval.

Porosity measurements made on cores from Hole 1072A (Fig. 22) range from 52% to a low of 3.4% for a fully lithified sample (269 mbsf). Porosity shows a slight overall decrease downhole, probably related to compaction. Smaller scale trends mirror index properties bulk density fluctuations discussed above. Changes in porosity associated with lithified intervals (e.g., ~165, 269, and 274 mbsf), and in the glauconitic silty sand with possible siderite nodules at ~255 mbsf are particularly pronounced, as are those between ~56 and 130 mbsf, where fluctuations in porosity may be at least in part related to slumping (see “Lithostratigraphy” section, this chapter). In the midst of this latter section is a short, undisturbed interval (~109–117 mbsf), where porosities are more uniform.

Magnetic Susceptibility

Magnetic susceptibility was measured on whole cores at 4-cm intervals on the MST (Table 15 on CD-ROM). No correction was made to the data to account for incompletely filled cores, and no filtering was applied to the raw data. Therefore, susceptibility data for Holes 1072A (Fig. 22) are likely to be useful for interpreting overall trends, but not for determining accurate individual values. Susceptibility trends are commonly used to infer changes in depositional environment and/or diagenetic changes. Susceptibility values increase markedly between 170 and 225 mbsf in Subunit IIA in a thick interval of silty clay containing pyrite (see “Lithostratigraphy” section, this chapter).

Natural Gamma-ray Emission

NGR measurements (Table 16 on CD-ROM) were made using the MST at 20-cm intervals in each section, with a counting period of

30 s. In Hole 1072A, NGR results (Fig. 22) are influenced by both sand vs. clay and glauconite contents. Recovery in lithostratigraphic Unit I was low, but the silty clays of Subunits IA/IB generally have higher NGR counts than the clayey silts at the top of Subunit IC, with a pronounced downhole decrease at the boundary. NGR counts increase downhole at 90 mbsf, where the muddy sands and sandy muds of the lower part of Subunit IC underlie an interval of no recovery, which is presumed to be sand. NGR counts increase downhole toward the base of Subunit IC, possibly as a result of increasing glauconite content; they peak in the glauconite sand interval at the boundary between Units I and II at ~150 mbsf. Beneath a sandy interval of poor recovery at the top of Unit II lies an interval (170–226 mbsf) of silty clays with fairly uniform NGR values, at the base of which is a downhole drop in counts. The interval 226–250 mbsf is sandier and contains four cycles, at least two of which are characterized by downhole increases. These cycles could represent fluctuating sand (coarsening upward) or possibly glauconite content, although little glauconite was described from this interval (see “Lithostratigraphy” section, this chapter).

Thermal Conductivity

Thermal conductivity was measured once per core (Fig. 22; Table 17 on CD-ROM). The wide sampling interval and the fact that measurements were preferentially made in the more clayey parts of cores allow only general observations to be made. Values range between 0.89 and 2.2 W/(m·K) and increase with depth, with the higher values tending to come from coarser grained intervals. In Subunit IA/IB (silty clay), values generally range between 1 and 1.4 W/(m·K), whereas those in Subunit IIA (silty clay) are between 1.45 and 1.8 W/(m·K). In Subunit IC, there seems to be a clear relationship with lithology: intervals of clayey silt, sandy mud, and muddy sand have progressively higher thermal conductivities. In contrast to the normal pattern, low values were observed at the boundary zone of Subunits IC and IIA in an interval of glauconitic sand. These low values may be the result of coring disturbance in this poorly recovered interval. The usual trend resumes below 175 mbsf: silty clays display higher values where they are more sandy (e.g., 182–187 mbsf), and values also increase in the muddy sands near the bottom of Subunit IIA.

Compressional Wave Velocity

Because Hole 1072A was drilled using the RCB system and core disturbance was greater than that with the APC/XCB, the PWL on the MST was not run. All *P*-wave velocity measurements are discrete measurements on split-core sections using only the PWS3 frame (orthogonal to core axis, *x*-direction; Table 18 on CD-ROM). Measurement frequency was the same as that for index properties, two per section (~75-cm spacing), with velocity and index properties measurements made at the same core locations.

P-wave velocities predominantly range between 1600 and 1900 m/s, with several higher velocity peaks (Fig. 22). A narrow peak in velocity (up to 2260 m/s) was noted at 36.6 mbsf in muddy sand and correlates with a similar density peak. The muddy sand was present in a short core in an otherwise unrecovered interval. A sharp downhole increase in velocity is observed at ~58 mbsf, near the boundary between lithologic Subunits IA/IB and IC (~pp3[s]; see “Seismic Stratigraphy” section, this chapter); silty clay overlies clayey silt near a downhole increase in bulk density at ~57 mbsf. Small fluctuations in velocity occur within Subunit IC to 147 mbsf, where there is a marked excursion to 2489 m/s. A high-velocity interval (2100–2489 m/s) lies between 147 and 151 mbsf, associated with an interval of glauconitic sand near the boundary between Units I and II and near pp4(s) (see “Seismic Stratigraphy” section, this chapter). A single velocity measurement of 5194 m/s in lithified sandstone creates a peak at 165.35 mbsf just below pp4(s). Velocities below the sandstone layer are remarkably uniform downhole throughout the remainder of Subunit IIA, with a downhole increase at 252 mbsf, near the bound-

ary between Subunits IIA and IIB/IIC, in the vicinity of pp5(s) (see “Seismic Stratigraphy” section, this chapter). Lithified sandstone layers at 268.79 mbsf are characterized by velocities in excess of 5700 mbsf.

Shear Strength

Undrained shear strength data are presented in Figure 22. Sandstone measurements were made once or twice per section and more frequently in sections with varying lithology (Tables 19, 20 on CD-ROM). Automated vane shear (AVS) measurements were made only to ~70 mbsf, below which the penetrometer was used because of the stiffness of the recovered material. In several cores, the sediment cracked when the penetrometer was inserted; no results were obtained when this occurred. Strength values reaching 220 kPa represent the upper limit of the penetrometer’s range of measurement. Actual strength values at such locations should be higher. In Subunit IC, shear strength increases downhole, whereas in Subunit IIA it generally decreases. In the upper 10 m of Subunit IC, described as clayey silt, values are <70 kPa. In Subunit IC, sandy mud between 100 and 120 mbsf has fairly constant shear strength (80–140 kPa). Strength increases downhole to 140 mbsf (150–200 kPa) as the sediment coarsens to muddy sand. In Subunit IC, high shear strength generally correlates with low porosity. Shear strength is low in the vicinity of the boundary between Units I and II. After first increasing, it then decreases downhole in the upper part of Subunit IIA, in an interval of silty clay that fines downhole. Below 220 mbsf, values generally decrease and little correlation between porosity and shear strength can be drawn. Shear strength in this interval may reflect sediment composition. Shear strength varies widely in the muddy sand below 233 mbsf.

Electrical Resistivity

Resistivity measurements were made once or twice per core. Resistivity values (Fig. 22; Table 21 on CD-ROM) range from ~0.8 to 3.2 Ωm . In general, because grain density is fairly constant, the dominant influences on resistivity are porosity and pore-water composition. In Hole 1072A, porosity appears to be the dominant influence, although it must be noted that few resistivity measurements were made in Subunits IA/IB, where recovery was low and the greatest changes in pore-water salinity occur (see “Inorganic Geochemistry” section, this chapter). The correlation between resistivity and porosity is particularly apparent in the vicinity of the boundary between Subunits IA/IB and IC and throughout Subunit IC, where resistivity fluctuations are greatest, perhaps associated with slumping (~56–130 mbsf). In the midst of this interval is a short interval (~109–117 mbsf) where resistivities are more uniform. Resistivity throughout Subunit IIA is fairly constant at ~1.2 Ωm , but more pronounced fluctuations are found below ~225 mbsf.

Summary

As at Site 1071, several discontinuities and trends in physical properties measurements coincide with observed lithologic changes, unit boundaries, and with interpreted seismic discontinuities (see “Lithostratigraphy” and “Seismic Stratigraphy” sections, this chapter). Several sharp changes in density correlate with changes in velocity in the same direction (e.g., both increasing downhole); consequently, they reinforce each other in generating impedance contrasts. The depths of these physical properties changes are generally consistent with previously estimated depth ranges to seismic discontinuities. For example, both density and velocity increase downhole at ~57–58 mbsf (~pp3[s]), in contrast to Site 1071, where they decrease downhole. Density and velocity also both increase downhole at ~147–151 mbsf in the interval of glauconitic sand, close to pp4(s). However, both also increase at ~165 mbsf in lithified sandstone, just below the estimated depth to pp4(s). Finally, density and velocity in-

crease at 252 mbsf in the vicinity of the interpreted depth to pp5(s). The lithified sandstone at ~265–274 mbsf has *P*-wave velocities exceeding 5700 m/s; because this was recovered in two cores, it may represent a thicker unit than was drilled at Site 1071 and COST-B2 (see “Downhole Logging” section, this chapter, and “Site 1071” chapter, this volume). The sandstone layer should thus be capable of generating a strong seismic reflection.

Resistivity appears to correlate mainly with porosity, as at Site 1071. Changes in pore-water chemistry appear to have little influence on resistivity values (see “Inorganic Geochemistry” section, this chapter). Magnetic susceptibility values increase markedly between 170 and 225 mbsf in Subunit IIA, in a thick interval of silty clay containing pyrite (see “Lithostratigraphy” section, this chapter).

SEISMIC STRATIGRAPHY

Introduction

In this section, we summarize regional geophysical information available before Leg 174A in the vicinity of Site 1072 (proposed Mid-Atlantic Transect [MAT] site 9B-1) and describe its use for deciphering the relationships between the sampled section and proposed fluctuations of sea level in the late Miocene–Pleistocene. One key component is a set of high-resolution multichannel seismic (MCS) profiles acquired during *Oceanus* Cruise 270 (Oc270, summer 1995), collected both in site-specific “hazards” grids (Fig. 23), and as a regional survey stretching from Leg 150 sites on the continental slope to the south to the Hudson Apron to the east (see “Introduction” chapter, this volume). These data were collected using a 48-channel receiver (6.25-m groups; 22-m offset to the near trace) and a single generator-injector (GI) air gun towed at 2–3 m below the sea surface. Seismic resolution is estimated to be ~5 m vertically throughout the interval anticipated for Leg 174A drilling and sampling (to ~1.2-s two-way traveltimes [TWT]). The Oc270 data build upon two other primary geophysical data sets: (1) MCS profiles collected by *Maurice Ewing* Cruise 9009 (Fig. 23; see “Introduction” chapter, this volume), and (2) downhole logs and velocities from a checkshot survey collected in an adjacent industry well, the Continental Offshore Stratigraphic Test (COST)-B2; see “Downhole Logging” section, this chapter).

Oc270 Profile 147 is a seismic dip line showing the sequence-stratigraphic surfaces penetrated and sampled at Site 1072 (Fig. 24). Using velocity functions derived from semblance analyses of Oc270

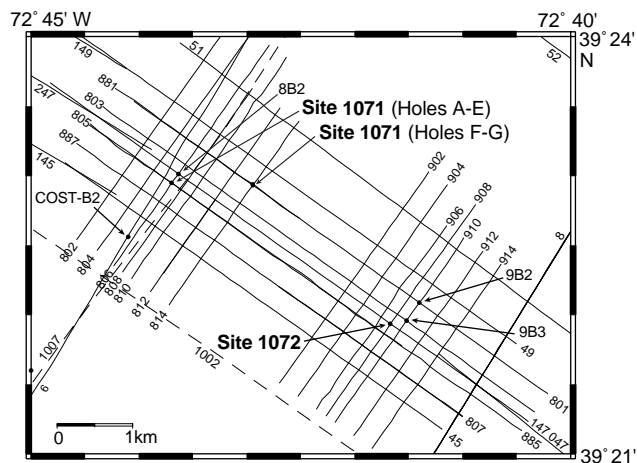


Figure 23. Leg 174A shelf sites (MAT-8B2, 8B3/ Site 1071 [Holes 1071A–1071E, 1071F–1071G]; MAT-9B1/ Site 1072, MAT-9B2, and 9B3), the COST-B2 well (see “Site 1071” chapter, this volume), and track lines of MCS profiles collected during Cruises Oc270 (solid lines) and Ew9009 (dashed lines).

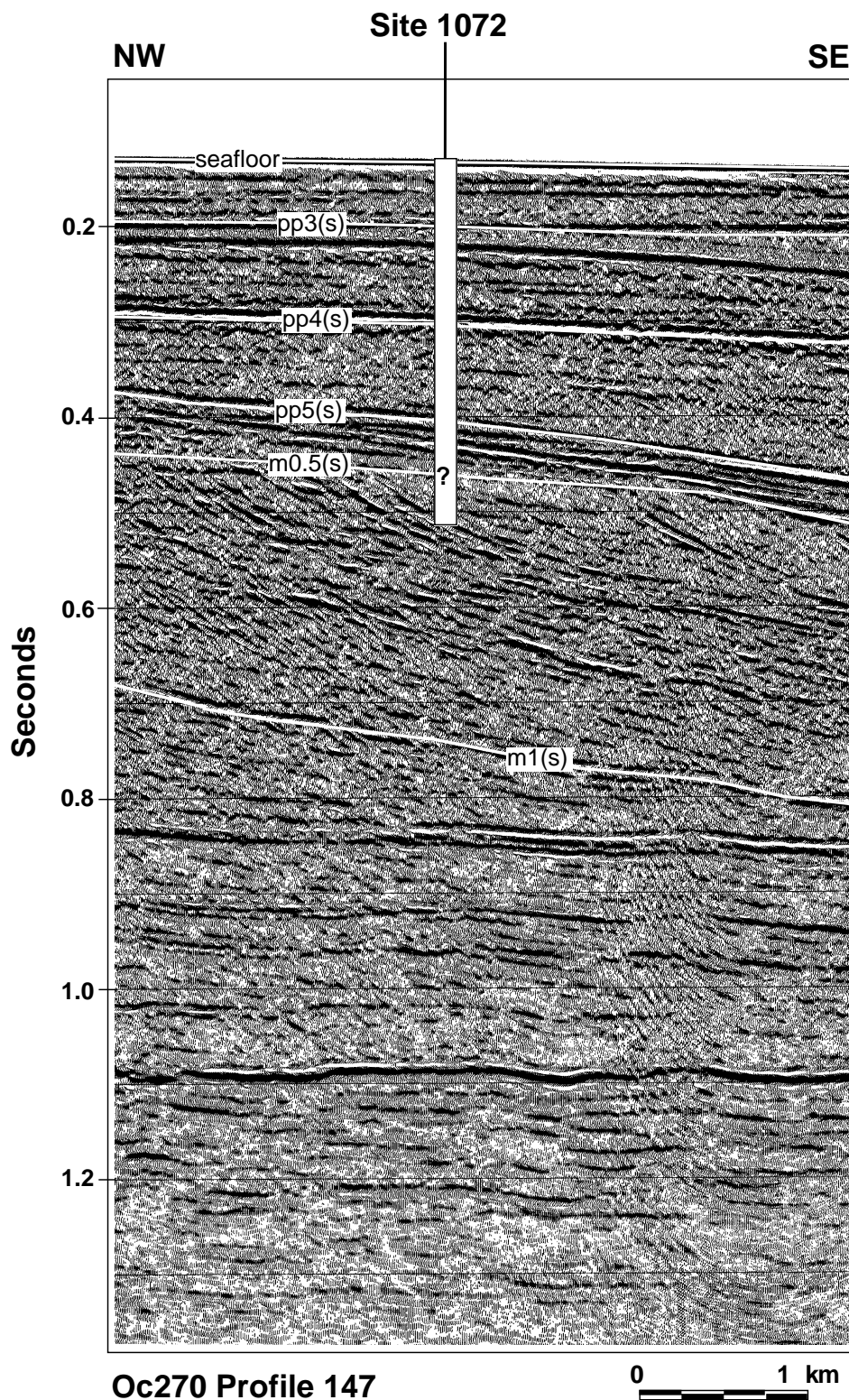


Figure 24. Interpreted version of part of Oc270 Profile 147, a dip section running through Site 1072 (see Fig. 23). The approximate total depth (TD) penetrated in Holes 1072A and 1072B at the site is indicated (vertical white bar), as are the locations (white lines) of prominent stratigraphic discontinuities/sequence boundaries identified by tying previously interpreted regional Ewing 9009 profiles to the Oc270 profiles (Christie-Blick et al., 1992; Mountain, Miller, Blum, et al., 1996; Austin et al., 1996). The “s” designation following the “pp” (provisionally Pliocene/Pleistocene) and “m” (provisionally Miocene) sequence boundary identifications are meant to distinguish the shelf sequence boundaries, targeted for sampling and logging by Leg 174A, from similarly labeled surfaces calibrated on the slope by Leg 150 (Mountain, Miller, Blum, et al., 1994).

Profile 51, checkshot survey results from the COST-B2 well, and results from a checkshot survey conducted at Site 1072, traveltimes-depth conversions of selected seismic surfaces (Table 22) were used first to predict, and then to attempt to tie, lithologies sampled at Site 1072 to the regional sequence-stratigraphic framework (see below). Information from other downhole logs that were collected in Holes 1072A, 1072C, and 1072D were also used to infer the nature of the sampled geologic section, particularly where samples were not recovered (see “Lithostratigraphy” and “Downhole Logging” sections, this chapter).

Predicting Sequence Boundary Depths

A base map (Fig. 23) displays the Oc270 seismic data, two Ew9009 regional profiles that cross this region, the COST-B2 well location, and the proposed and approved MAT-8B and 9B drilling locations (MAT-9B1 became Site 1072). Figures 24 (dip seismic Profile Oc270-147) and 25 (adjacent dip seismic Profile Oc270-885, which connects Site 1071 with a point ~150 m south-southwest from

Site 1072) illustrate some of the key seismic-sequence boundaries that were mapped into the Oc270 profiles (Table 22) using a sequence-stratigraphic framework derived from previous (e.g., Greenlee et al., 1992) and ongoing (Fulthorpe and Austin, 1998) interpretations of industry MCS data and extrapolations from Leg 150 (Mountain, Miller, Blum, et al., 1994; Miller et al., 1996) and Ew9009 profiles to Oc270 profiles (Christie-Blick et al., 1992; Mountain et al., 1996; Austin et al., 1996; see “Introduction” chapter, this volume). Stratigraphic goals for drilling and logging at Site 1072 were penetration of the m0.5(s), the m1(s) late middle Miocene sequence boundaries, and their associated stratigraphic successions; the m1(s) boundary was presumed from Leg 150 results to be ~11 Ma (Miller et al., 1996). Site 1072 was located to sample the m0.5(s) sequence boundary near its rollover/breakpoint and the m1(s) sequence boundary ~3.5 km seaward of its rollover/breakpoint (Fig. 25). As at Site 1071, the “s” designation following the “pp” (provisionally Pliocene–Pleistocene) and “m” (provisionally Miocene) sequence boundary identifications is meant to distinguish the shelf sequence boundaries, targeted for sampling and logging by Leg 174A, from

Table 22. Traveltime-depth ties at the crossing of Oc270 Profile 147 with Oc270 Profile 908 (Site 1072).

Prespud reflector depths	TWTT (s)	TWTT (sbsf)	Depth (mbsf*)	Depth (mbsf**)	Depth (mbsf***)	Comments
Oc270 Profile 147						
Seafloor (98 m)	0.131	0.000	0	0		
late Miocene–Pleistocene (informal)						
pp3(s)	0.202	0.071	52 (49-55)	67	58	Hiatus/offlap/onlap
pp4(s)	0.304	0.173	148 (141-155)	163	155	Hiatus/offlap/onlap
pp5(s)	0.400	0.269	237 (225-249)	254	246	Possible onlap
Miocene (modified from Miller et al., 1996)						
m0.5(s)	0.460	0.329	293 (278-308)	311	302	Hiatus/offlap/onlap
m1(s) (~11 Ma)	0.737	0.606	551 (523-579)	583	—	Hiatus/offlap/onlap

Notes: TWTT = two-way traveltime, sbsf = seconds below seafloor. * = calculated using semblance velocities from Oc270 Profile 51. These depths are considered accurate to ±5%, so a range is also given (in parentheses) to reflect this uncertainty (see “Seismic Stratigraphy” section, “Site 1071” chapter, this volume). ** = calculated using COST-B2 checkshot velocity function (see “Downhole Logging” section, “Site 1071” chapter). *** = calculated using Site 1072 checkshot velocity function (see “Downhole Logging” section, this chapter). Traveltime-depth conversions were made using an average velocity-traveltime relationship derived from semblance picks interpreted at ~1-km intervals from adjacent Oc270 Profile 51 (see Fig. 23 and “Seismic Stratigraphy” section, “Site 1071” chapter), a checkshot survey/VSP from the COST-B2 well (see Fig. 23 and “Seismic Stratigraphy” section, “Site 1071” chapter), and checkshot results from Site 1072 (see “Downhole Logging” section, this chapter).

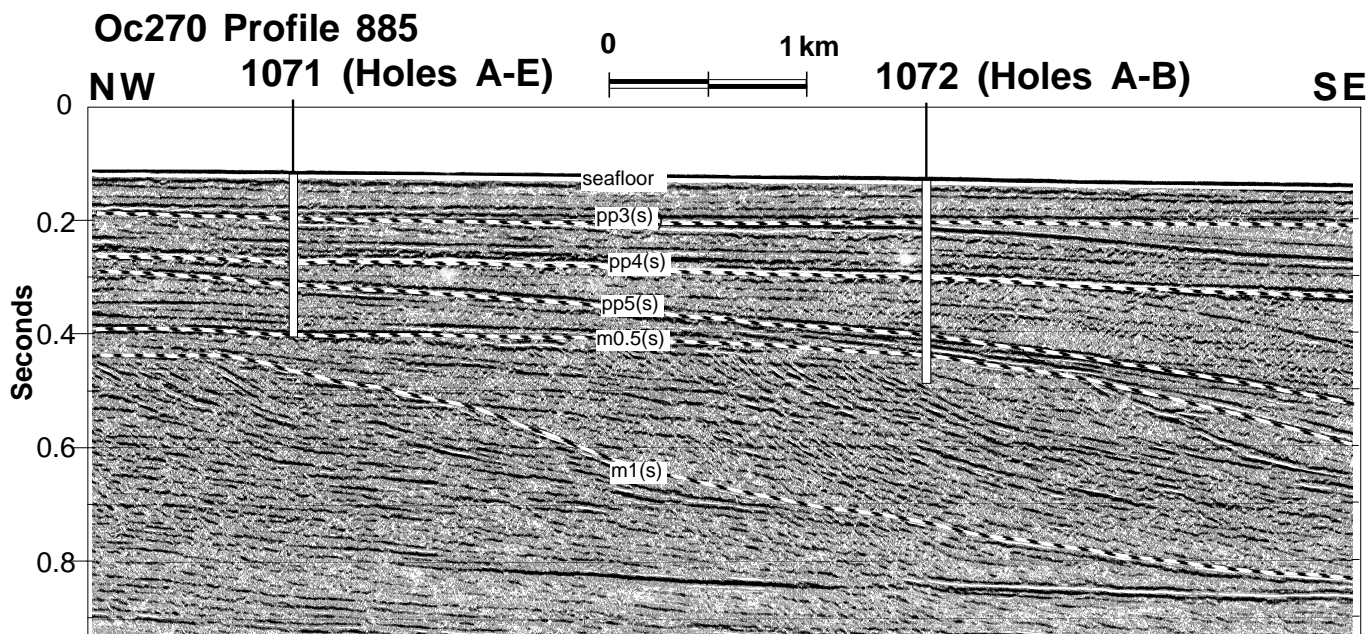


Figure 25. Interpreted version of part of Oc270 Profile 885, a dip profile that runs through Holes 1071A–1071E (Fig. 23), and within ~150 m of Site 1072. The approximate total depths (TDs) penetrated at Holes 1071A–1071E and Holes 1072A and 1072B are indicated (vertical white bars), as are the locations of prominent stratigraphic discontinuities/sequence boundaries (dashed lines) identified by tying previously interpreted regional Ew9009 profiles to the higher resolution Oc270 profiles (Christie-Blick et al., 1992; Mountain, Miller, Blum, et al., 1996; Austin et al., 1996).

similarly labeled surfaces calibrated on the slope by Leg 150 (Mountain, Miller, Blum, et al., 1994). Site 1072, along with Site 1071, examined the chronostratigraphic and paleobathymetric signatures of these “typical” progradational sequences during the 0–42 Ma “Ice-house” interval (see “Introduction” chapter, this volume).

Unstable hole conditions precluded sampling as deeply as m1(s) at this site; m0.5(s) was probably penetrated (see “Downhole Logging” section, this chapter), but no samples were recovered in a thick section of unconsolidated sands over the expected depth range of this sequence boundary. Pleistocene–latest Miocene surfaces pp3(s), pp4(s), and pp5(s) were sampled and their stratigraphic significance is discussed below.

Time-Depth Estimation Technique

Several different techniques were used to predict depths from traveltimes using Oc270 profiles at or near Site 1072. The first involved using the COST-B2 VSP or checkshot survey (see also “Downhole Logging” section, “Site 1071” chapter, this volume). The second was a compilation of semblance or stacking velocity analyses used for normal moveout corrections of Oc270 Profile 51 near the site (Fig. 23). The third was a compilation of velocity analyses from a checkshot survey conducted at Site 1072 (see “Downhole Logging” section, this chapter). Different sets of interval velocities resulted; these velocities were used to calculate the depths of sequence boundaries on Oc270 profiles in the vicinity of Site 1072 (Table 22; also see “Seismic Stratigraphy” section, “Site 1071” chapter, this volume).

Calculation of Depths

Using the Oc270 Profile 51, COST-B2, and Site 1072 time-depth conversion equations, depths to sequence boundaries interpreted on

Oc270 profiles in the MAT-9B grid (Fig. 23) were calculated (Table 22). These depths were used by the Shipboard Scientific Party as guides for interpretation of lithostratigraphy (see “Lithostratigraphy” section, this chapter), magnetostratigraphy (see “Paleomagnetism” section, this chapter), and biostratigraphy (see “Biostratigraphy” section, this chapter) during drilling of Holes 1072A and 1072B. A preliminary synthesis of those results is presented below (Fig. 26).

Outer Shelf Late Miocene/Pleistocene Sequence Boundaries: Preliminary Lithostratigraphic/Chronostratigraphic Correlations

Figure 26 summarizes preliminary ties between seismic surfaces identified regionally on Oc270 dip Profile 885 in the vicinity of Site 1072 and the lithostratigraphy and chronostratigraphy that were developed as a result of sampling in Holes 1072A and 1072B. Figure 27 illustrates the same information for Holes 1071A–1071E, and compares it to results from Holes 1072A and 1072B (see “Seismic Stratigraphy” section, “Site 1071” chapter, this volume). From the top down, three “Pliocene–Pleistocene” discontinuities were identified: pp3(s), pp4(s), and pp5(s). The pp3(s) boundary correlates approximately with the transition between lithostratigraphic Subunits IB and IC at 57.5 mbsf; the predicted depth for this surface was 49–55 mbsf (Table 22). Compressional wave velocity and density both increase downhole at ~57–58 mbsf (see “Physical Properties” section, this chapter). The checkshot survey conducted in Hole 1072B provides a depth of 58 mbsf for pp3(s) (see Table 22 and “Downhole Logging” section, this chapter), almost exactly correlative with the lithostratigraphic results. The pp3(s) surface is 0.25–0.78 Ma, based in part upon its close spatial association with the B/M boundary at 62.3 mbsf in Hole 1072A (see “Paleomagnetism” section, this chapter). The transition from lithostratigraphic Subunit IC to IIA at

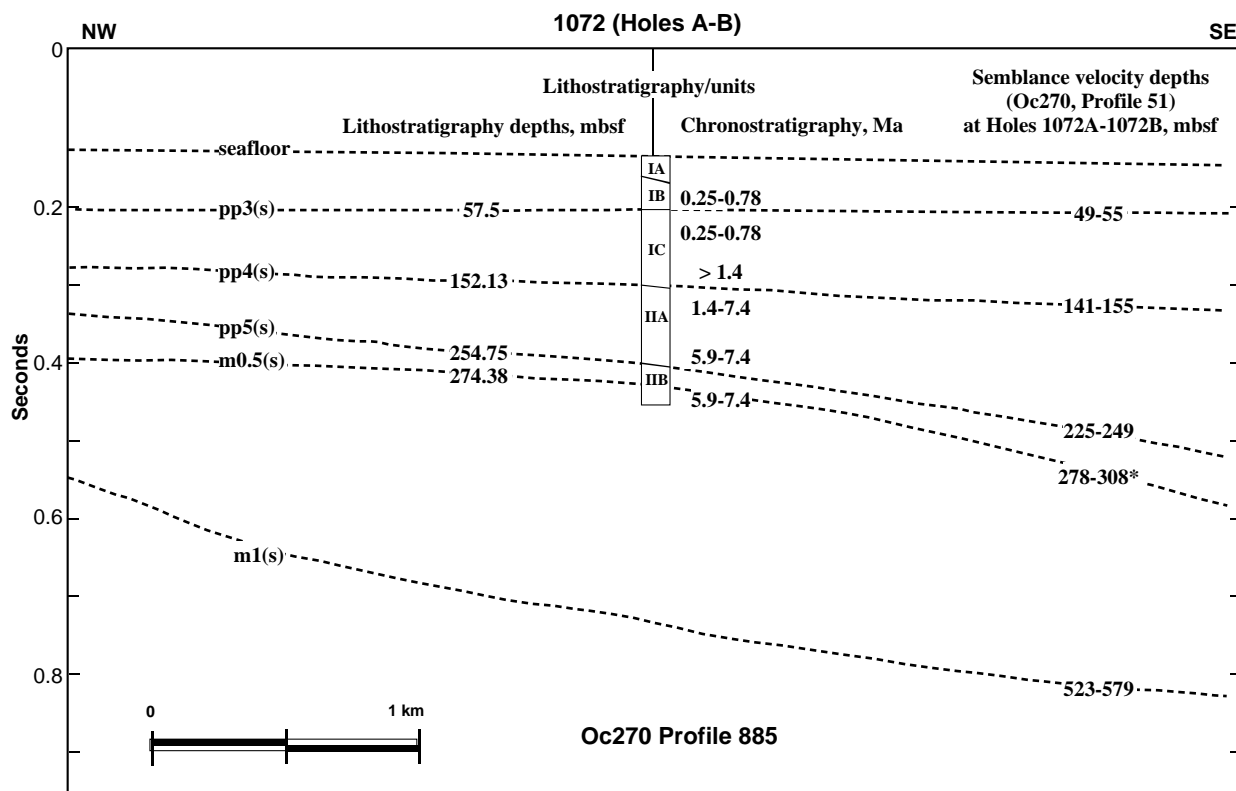


Figure 26. A summary of the preliminary chronostratigraphy (see “Biostratigraphy” section, this chapter) and lithostratigraphy (see “Lithostratigraphy” section, this chapter) at Site 1072, tied to the preliminary sequence stratigraphy interpreted along Oc270 Profile 885 (see also Fig. 25). The asterisk associated with the m0.5(s) depth (278–308* mbsf) is in reference to the prespud prediction (Table 22) only; neither sampling nor logging unequivocally identified this sequence boundary at Site 1072 (see “Downhole Logging” section, this chapter).

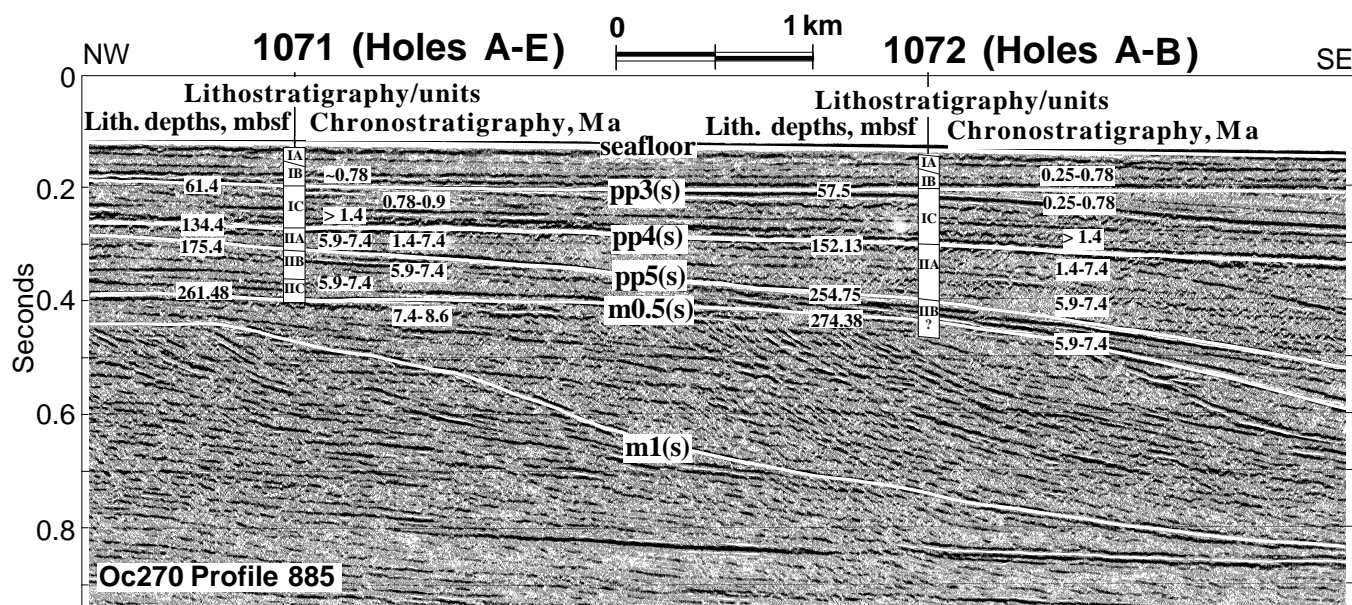


Figure 27. A preliminary comparison of results from Holes 1071A–1071E and from Holes 1072A and 1072B, superimposed on Oc270 Profile 885. Although the primary target was the m1(s) clinoform front and associated sequence, ample chronostratigraphic and lithostratigraphic evidence was collected at both sites to constrain sequence boundaries of late Miocene (pp5[s]) through late Pleistocene (pp3[s]) age. Wireline logs were collected in Hole 1072A; a checkshot survey (VSP) was run in Hole 1072B. Logging-while-drilling downhole measurements were acquired in Hole 1072D (see “Downhole Logging” section, this chapter).

~152.13 mbsf corresponds approximately to pp4(s); the predicted depth range of pp4(s) was 141–155 mbsf (Table 22). This sequence boundary may mark a Miocene/Pleistocene hiatus; above pp4(s), ages are >1.4 Ma, whereas below, ages are 1.4–7.4 Ma (see “Biostratigraphy” section, this chapter; Fig. 26). Wireline logs pinpoint pp4(s) at 157 mbsf in Hole 1072A and 151.4 mbsf in Hole 1072B, correlative with a glauconite sand at those depths. The checkshot survey carried out in Hole 1072B provides a depth of 155 mbsf for pp4(s) (see “Downhole Logging” section, this chapter). Compressional wave velocity and density both increase downhole at ~147–151 mbsf, and again at ~165 mbsf. The stratigraphic significance of pp5(s) is uncertain. Its prespud predicted depth was 225–249 mbsf (Table 22); that depth would make it approximately correlative with the transition between Subunits IIA and IIB/C at 254.75 mbsf (see “Lithostratigraphy” section, this chapter). The checkshot survey in Hole 1072B provides a depth of 246 mbsf for pp5(s) (see Table 22). Compressional wave velocity and density both increase at 252 mbsf, as well as in the lithified sandstone at ~268.79 mbsf (see “Physical Properties” section, this chapter). Preliminary biostratigraphic information (see “Biostratigraphy” section, this chapter) suggests that pp5(s) may not mark an identifiable depositional hiatus (Fig. 26). Instead, this boundary may represent a late Miocene flooding surface (see “Summary and Conclusions” section, this chapter). Hole 1072B bottomed at 358.6 mbsf in a thick section of unconsolidated sands; unfortunately, there was virtually no recovery in the interval below 306.8 mbsf in which coring was attempted. The predicted depth to the m0.5(s) sequence boundary was 278–308 mbsf (Table 22; Fig. 26).

DOWNHOLE LOGGING

Introduction

Downhole log measurements are crucial to the primary goal of Leg 174A, which is to determine the lithologic character, age, and origin of regional discontinuities in siliciclastic sediments. Rapid sedimentation and minor tectonic subsidence during a time of known

glacial-eustatic sea-level change combine to make the Neogene New Jersey margin an excellent location to examine the link between sea-level change and the stratigraphic record. These sand-prone, shallow-water sediments, however, are especially difficult to drill and core, and for this reason provide compelling reasons to pursue downhole log measurements.

Unstable hole conditions often caused washouts to diameters much greater than bit size, as well as hole constrictions impassable by wireline devices, some of which packed off the BHA and completely stopped the drillstring. In many instances, sand-rich intervals could be drilled, but not cored. In these situations, wireline logging was the only record of formation properties (e.g., bed thickness and gross composition). Because of shallow water depths, it was not possible to use the sidewall-entry sub (SES); as a result, fluids could not be circulated while logging. Half-core advances were used in Hole 1072A to optimize core recovery, but this may have contributed to the deterioration of hole conditions.

LWD was employed in Holes 1072C and 1072D because of the desire to log in a less deteriorated borehole, the need to acquire data to the seafloor, and because of difficulties in getting wireline logging devices down the open hole. LWD operations proved that, as long as the sediment could be drilled, under most conditions, continuous and good-quality log data could be acquired. Nonetheless, in extremely sandy intervals in the bottom of Hole 1072D, washouts were a problem. This may have resulted from the need to maintain high circulation rates in an attempt to clear the bit and lift these sands up and out of the borehole. It is also possible that because of the very loose nature of these sands, sediment was washed away from the bit before a core could be cut.

These logging data were augmented with a checkshot survey in Hole 1072B that provided reliable ties between logs and cores measured in depth and seismic data measured in acoustic traveltime. Seismic data constitute the primary means by which regional stratigraphic discontinuities have been recognized on the New Jersey shelf and slope. Understanding the nature of these surfaces is a major objective of Leg 174A (see “Introduction” chapter, this volume).

Logging Operations

Logging operations at Site 1072 are summarized in Figure 28. Hole 1072A was logged from 300 mbsf to the seafloor using the triple combo logging string (dual induction resistivity, neutron porosity, and density tools), the spectral gamma-ray, and the Lamont-Doherty Earth Observatory temperature tools. Log data are of good quality except for washed-out intervals near the bottom of the hole. A repeat run from 110 mbsf up to 30 mbsf confirmed the log responses of the main run. The pipe became stuck while rigging down and was severed at 23 mbsf.

Hole 1072B was then washed to 306.8 mbsf and logged in three complete wireline runs. The wireline heave compensator was used to counter the relatively small ship heave resulting from the minimal sea state. The first run with the sonic-resistivity string failed to pass a bridge at ~90 mbsf. The tool string was pulled out, the hole was reamed, and a repeat run was made using the LSS in place of the SDT. Despite difficulties in passing several bridges with diameters of ~6 in, the hole was logged successfully from 306.5 mbsf up to the pipe at 43 mbsf. Overall, the LSS tool, despite its lack of a receiver array, performed better than the SDT in the variable-diameter borehole and the relatively low-velocity sediments in this hole. The FMS tool was then run from 306.5 to 38 mbsf in Hole 1072B. A VSP completed the final logging operations in Hole 1072B. Shots were fired from the ship's GI airgun, which was tethered to a float at 2.4 mbsl and 48.5 m offset from the moon pool off the port quarter. The geophone receiver in the WST was clamped at 12 positions in the borehole between 296 and 58 mbsf at an average interval of 20 m (Table 23).

Successful operations in Hole 1072B demonstrated that these sand-prone intervals could be logged; therefore, LWD was conducted in Holes 1072C and 1072D to 106 and 356 mbsf, respectively. Hole 1072D was drilled because of failure to re-enter Hole 1072C after pulling up the pipe to add drilling jars to the BHA. Measurements included resistivity, spectral gamma ray, neutron porosity, density, and PEF (photoelectric factor). In addition, borehole diameter was statistically derived from the density measurements. Log data were recorded in the upper ~100 m of both Holes 1072C and 1072D, providing replicate LWD measurements and thus quality control for these sets of data.

Data Quality and Wireline-LWD Comparisons

The wireline logs recorded in Holes 1072A and 1072B are shown in Figure 29; they are generally of high quality. However, density, induction, and sonic data recorded in the drill pipe (Fig. 28) are not interpretable; furthermore, the natural gamma-ray logs in the pipe are highly attenuated and should be interpreted only qualitatively. Both holes were enlarged in some intervals, possibly a result of washouts within sand-rich layers (see the caliper log in Figure 29); as a result, the density log and FMS images in these sections are degraded. Poor data quality arises when the sensing pad does not make complete contact with the borehole wall, and a small amount of borehole fluid is included with the measurement of sediment density and electrical conductivity. Roughly 20% of these holes were washed out beyond the maximum opening of the FMS calipers. However, images of the remaining 80% of the log provide good detail of bedding features.

The velocity data from the logs are of high quality. A minor amount of cycle skipping (resulting in velocities that are one half the actual formation values) is present in the raw log data, but shipboard processing of the traveltimes eliminated these excursions. Thin intervals of especially abrupt velocity changes correspond to indurated sandstones. The WST measurements at 12 positions within Hole 1072B provided excellent data for time-depth conversion (Table 23). The data indicate interval velocities that compare well with the shipboard *P*-wave measurements on cores from Hole 1072A (Fig. 30), and yield a time-depth conversion that gives seismic-core-log correlations a high degree of precision.

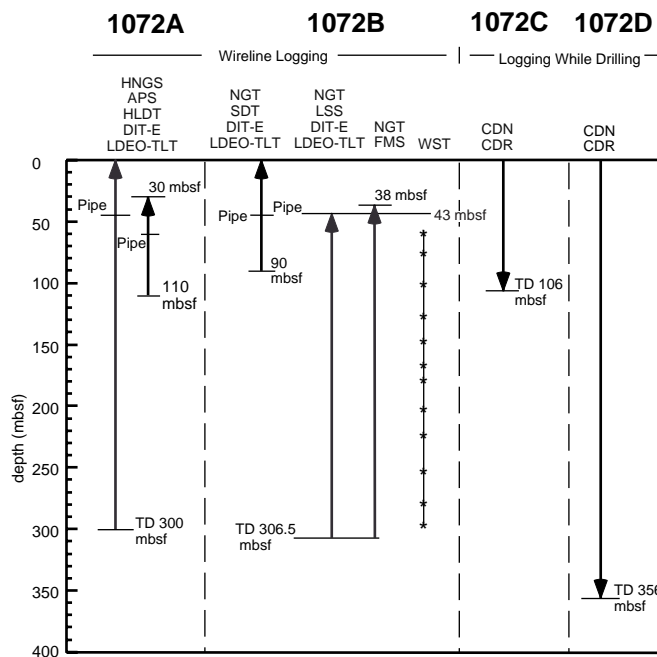


Figure 28. Summary figure of Site 1072 logging operations. HNGS = Hostile-environment Natural Gamma-ray Spectrometry tool; APS = Accelerator Porosity Sonde; HLDT = Hostile-environment Litho-Density Tool; DIT-E = Dual Induction Tool; LDEO-TLT = Lamont-Doherty Earth Observatory Temperature-Logging Tool; NGT = Natural Gamma-ray Tool; SDT = array-sonic tool; LSS = Long-Spaced Sonic tool; FMS = Formation MicroScanner; WST = Well Seismic Tool; CDN = Compensated Density Neutron tool; CDR = Compensated Dual Resistivity tool; * = station for WST; TD = total depth reached by each tool string.

Table 23. Checkshot data collected in Hole 1072B.

Depth (mbrf)	OWTT (ms)	Depth (mbsf)	TWTT (ms)	Interval velocity (m/s)
405	225.1	296	319	
387	216.6	278	302	2094
361	203	252	274	1892
333	188.4	224	245	1894
310	176.4	201	220	1889
287	164.2	178	195	1854
275	157.7	166	182	1813
256	148.6	147	164	2035
235	138.2	126	142	1961
209	124.5	100	114	1836
184	112	75	88	1908
167	102.7	58	68	1737
109.5	65.3	0	0	1693

Notes: First two columns record the unprocessed checkshot data. Depth is referenced in meters below rig floor (mbrf), and one-way traveltimes (OWTT) is referenced from the sea surface. The last three columns record the processed checkshot data. Two-way traveltimes (TWTT) is referenced from the seafloor; interval velocities record the average velocity at the given depth to the depth of the next checkshot measurement. Water depth at this site is 98 m (65.3 ms below the sea surface at a nominal sea-water velocity of 1500 m/s).

LWD was a valuable complement to the wireline logs, providing measurements in the shallow section that was shielded by the BHA during the wireline logging runs and within the interval 300–356 mbsf, where wireline logs were not obtained in Holes 1072A or 1072B. Despite difficult drilling conditions, LWD data quality is good over most of the drilled interval. High penetration rates and enlarged borehole diameters degraded data quality within sandy intervals (Fig. 31). This was especially true for the density, PEF, and neutron porosity logs, which are the measurements most sensitive to borehole conditions. The differential caliper shows that 17% of Hole

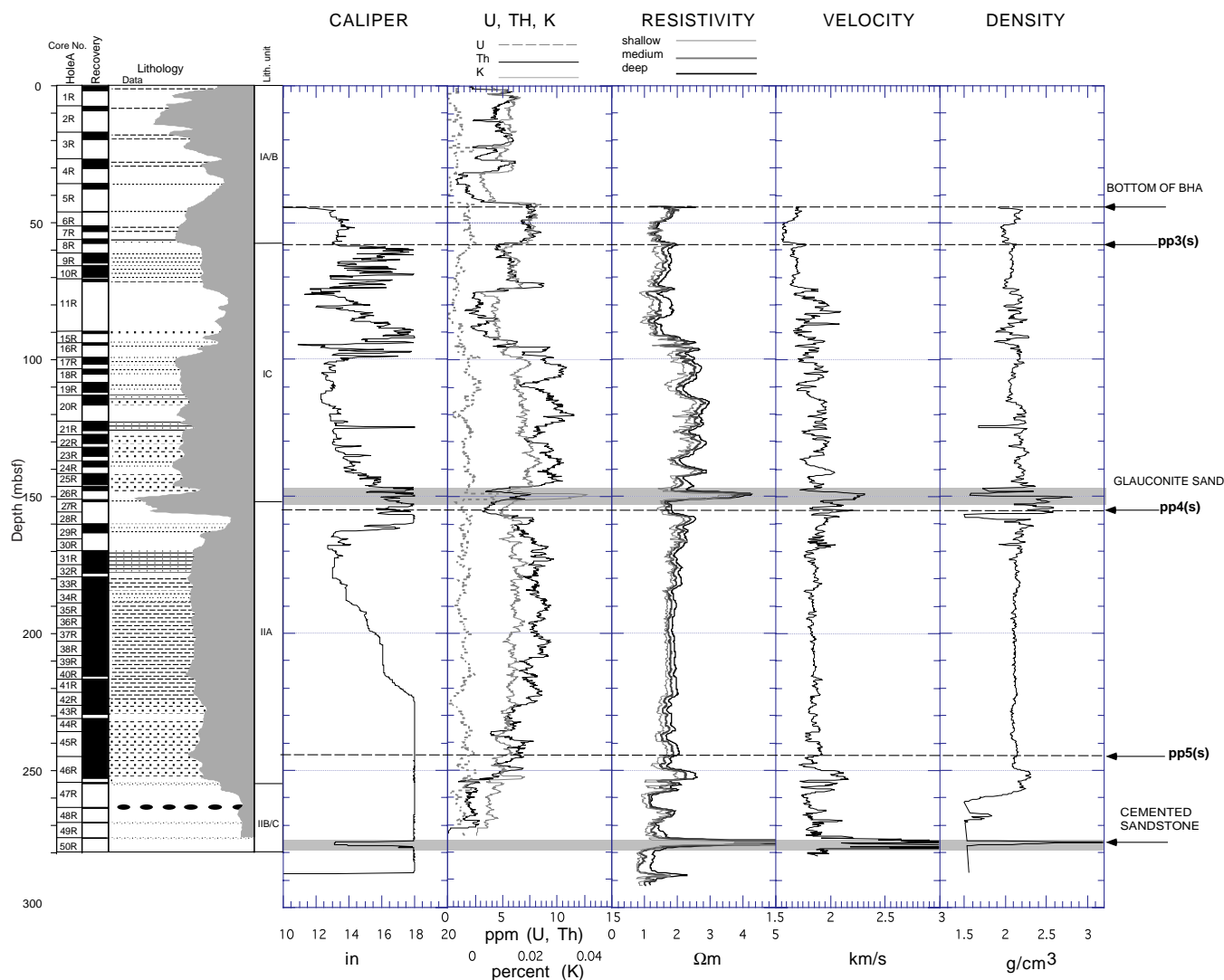


Figure 29. Summary of wireline logs at Site 1072 compared to the core-derived lithologic interpretations (see “Lithostratigraphy” section, this chapter). Caliper and density data are from Hole 1072A; remaining logs are from Hole 1072B. Depths of mapped seismic surfaces (pp3[s], pp4[s], and pp5[s]; Table 22) based on the Hole 1072B checkshot velocity function are shown on the right margin. The lithology column (see “Lithostratigraphy” section, “Explanatory Notes” chapter, for symbols) is composed using the gamma-ray curve (gamma ray increasing to the left) to illustrate high clay content and/or glauconite (gray area).

1072D had a diameter >1 in larger than the bit (“tool standoff”) and should be “suspect” according to industry standards. About 9% of the differential caliper data in Hole 1072D indicate a tool standoff of zero. While this would seem ideal, such data must also be examined carefully because intervals of severe washout (hole diameter >6 in greater than the bit size) are generally beyond the ability of the density caliper to detect hole variations. In these cases, density and PEF measurements also tend to be much lower than expected (e.g., <1.5 g/cm³), confirming the interpretation that the hole is probably out of gauge despite a differential caliper value of zero. Several wiper trips were made during the course of drilling Hole 1072D to prevent getting the BHA stuck; the deterioration of the hole during these wiper trips may have adversely affected data quality over some intervals (e.g., 225–235 mbsf). Bit size and differential caliper corrections were applied to all LWD logs except resistivity to minimize the effects of variable borehole conditions.

LWD density, neutron porosity, and PEF suffer from poor hole conditions in intervals throughout the drilled section (Fig. 32) and are unreliable below ~260 mbsf. Low gamma ray and resistivity in this interval, as well as severely washed-out hole conditions, suggest a thick sandy unit at this depth (see below). LWD gamma-ray (GR)

measurements compare well with wireline total spectral gamma ray (HSGR, from the IPLT string), but are consistently higher than the wireline SGR (sonic-resistivity string; Fig. 33). Both the LWD GR and HSGR were corrected for borehole diameter during shipboard processing, while the sonic-resistivity SGR was not (SGR borehole diameter corrections are performed postcruise at LDEO). The LWD GR log shows greater amplitude of change than the wireline HSGR, possibly because of incomplete borehole correction within the washed-out intervals where the LWD statistical caliper (DCAL) may not indicate borehole diameter precisely.

A significant difference between wireline and LWD logging is that the elapsed time between cutting the hole and making the measurements is much shorter in the latter. For example, in Holes 1072A and 1072B, the time between drilling and wireline logging was more than 12 hr. In contrast, during the LWD run, the time between when the formation was drilled and when it was logged was ~5–10 min. Resistivity measurements are very sensitive to changes in the formation fluid caused by invasion of drilling fluids. This invasion process is more easily detected when the resistivity of the formation water is different from that of the borehole fluid. The separation between the shallow and deep resistivities is therefore interpreted to represent for-

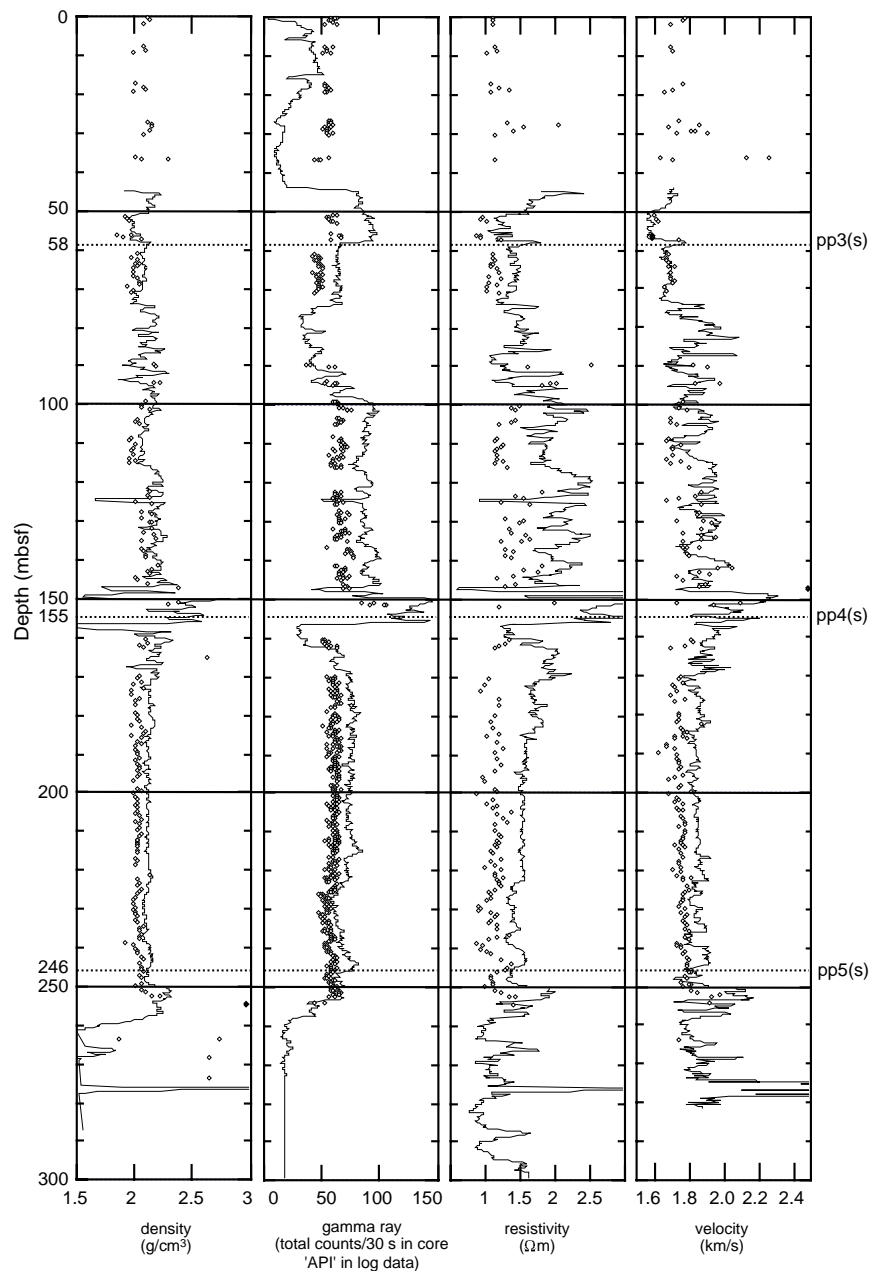


Figure 30. Comparison of physical properties measurements (diamonds) on cores from Hole 1072A and logging data (lines) from both Holes 1072A and 1072B. There is good agreement between both measurements, except that the core data values are generally lower than those derived from the log data, which can be explained by the expansion of the cores after recovery. Depths of seismic surfaces (pp3[s], pp4[s], and pp5[s]; see Table 22) are calculated from the Hole 1072B checkshot velocity data. These depths would be slightly different in Hole 1072A, ~20 m up dip (Fig. 1).

mation invasion by borehole fluid (seawater + sepiolite mud) into porous and permeable layers. At Site 1072, over the interval logged, the deep resistivity is greater than the shallow resistivity in many of the sand intervals (Fig. 28), implying that the formation fluid is less saline (fresher) than the borehole fluid.

LWD resistivity logs at Site 1072 show good agreement with the wireline results (Figs. 33 and 34). The negligible offset between LWD deep (ATR) and shallow (PSR) resistivities indicates minimal invasion of the formation (Fig. 34). In contrast, wireline resistivity measurements show invasion in both sandy and muddy intervals because of the longer time between drilling and logging (Fig. 34). Sandy layers commonly show a 0.4–0.6 Ωm offset between the deep and shallow measurements in both the LWD and wireline resistivity logs, suggesting very early invasion of the formation (Fig. 34). The degree of separation between shallow and deep resistivity is therefore a useful quantity for defining porous and permeable intervals. The intervals showing greatest separation also correspond to the lowest GR values and are interpreted to be sand-rich and/or coarser grained units (Fig. 34).

Results

A major goal of Leg 174A is to understand how the details of borehole-scale observations relate to the geometry of regional stratal surfaces seen in seismic profiles. Accordingly, we devoted considerable attention to log-seismic correlations to ensure we understood how regional surfaces expressed in seismic profiles were manifested in the rock record. The discussion that follows begins with a summary of log-seismic correlations, and concludes with a discussion of log-core correlations. Integrated shore-based studies of logs, cores, and seismic data will continue to be very valuable in reaching the goals of Leg 174A.

Log-Seismic Correlation—Sonic Data

In situ sound velocities provide a valuable link between logs and borehole samples measured in depth and seismic reflections measured in time. At Hole 1072B, we collected wireline sonic-log data as well as traveltimes to a hydrophone (a “checkshot survey” or VSP)

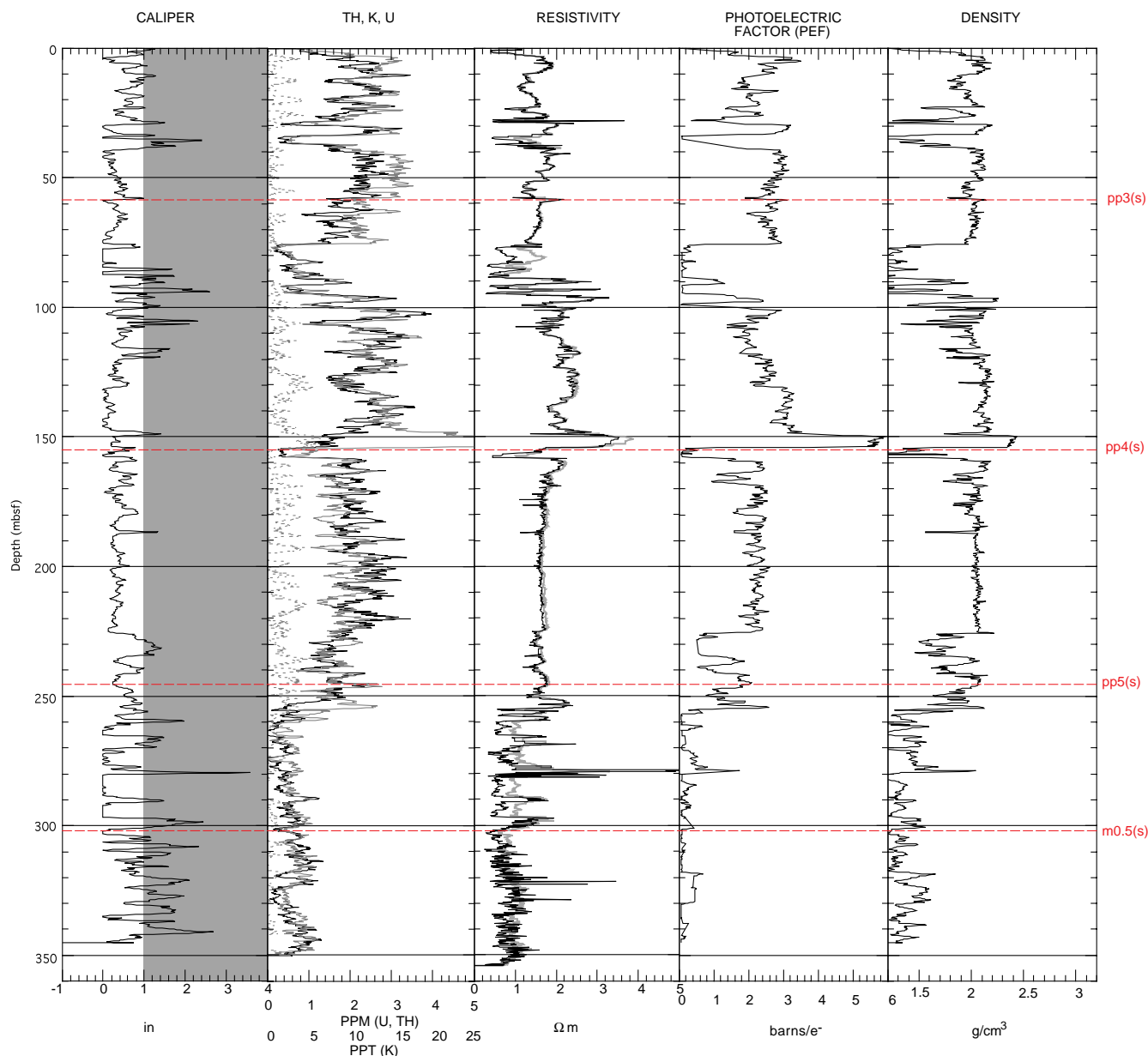


Figure 31. Summary of LWD results from Hole 1072D. Tool standoff of 1 in or greater (gray-shaded region) indicates less reliable data quality (see text for further discussion). In the Th, K, U plot, Th = black line, K = gray line, and U = dashed line. In the resistivity plot, lower values represent shallow resistivity (black line) and higher values deep resistivity (gray line). Depths of mapped seismic horizons are indicated, as calculated using Hole 1072B checkshot velocity data.

clamped to the borehole wall at 12 depths between 58 and 296 mbsf (Table 23). These two procedures provided reliable and complementary measures of sound velocity throughout the cored interval, and from these we have calculated time-depth conversions and prepared a synthetic seismogram to investigate the geologic significance of prominent seismic reflections.

Before measurements at Site 1072, the COST-B2 sonic-log and checkshot survey (Scholle, 1977), plus semblance analyses of nearby Oc270 multichannel seismic data, were the best velocity information available (see “Seismic Stratigraphy” and “Downhole Logging” sections, “Site 1071” chapter, this volume). These data are compared with the Site 1072 checkshot velocity data in Figure 35. The COST-B2 checkshot provides one velocity measurement, of ~1800 m/s, for the entire interval logged at Site 1072. In contrast, the semblance velocity analysis of nearby Oc270 Profile 51 provides several downward increasing values, all of which agree closely with the checkshot data.

There is overall agreement between the COST-B2/semblance values, and the log velocity/checkshot data acquired in Hole 1072B, as well as with shipboard *P*-wave velocity measurements performed on cores from Hole 1072A (Fig. 35; Table 23). Understandably, the shipboard data show two departures from the other data: first, most values are slower than those measured by the other in situ techniques, probably because of unloading from in situ pressure; second, shipboard measurements were occasionally made on unusually high-velocity sandstones that tend to be thin ($\ll 1$ m) and below the vertical resolution of the other techniques. For example, velocities reach 5194 m/s and 5700 m/s in such sandstones at ~165.35 and ~268.79 mbsf in Hole 1072A; these values are too high to plot in the range shown in Figure 35. The latter bed is clearly imaged in the resistivity log as a highly resistive interval.

The first sonic-log data were collected at 40 mbsf, immediately below the bottom of the drill pipe. There is a 40 m/s decrease in velocity from this point to where values increase abruptly at 58 mbsf.

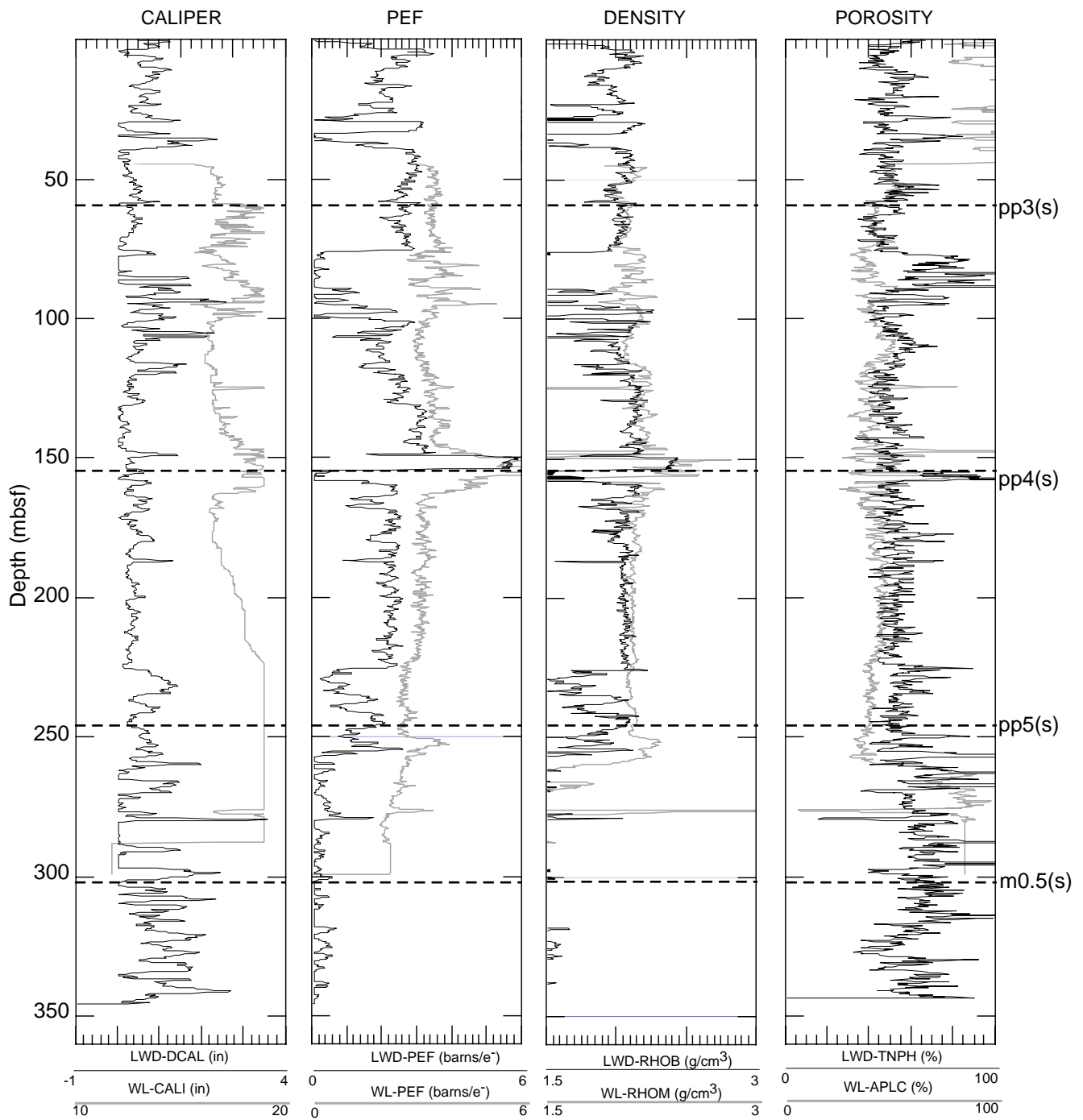


Figure 32. Comparison of wireline (WL) with LWD logs, Site 1072. The caliper logs for both LWD and wireline indicate substantial borehole washouts. LWD logs are more sensitive to increasing borehole size, and the data quality for density, porosity, and photoelectric factor (PEF) is lower in sections of hole enlargement. Depths of mapped seismic horizons are indicated on the right, as calculated using Hole 1072B checkshot velocity data.

Changes in other log characteristics are observed at these same levels (Fig. 29), and the deeper of the two matches pp3(s) as well as the base of lithologic Subunit IA/IB. Both the sonic-log and checkshot data detect an abrupt downward increase in velocity at ~75 mbsf, which is near the top of an 18-m interval of very low core recovery and no shipboard measurements. We equate this depth to an unnamed flooding surface that lies between pp3(s) and pp4(s) (see prominent change in seismic facies, Fig. 24). Below 75 mbsf, all three sets of velocity data (checkshot, sonic log, shipboard) show a relatively erratic pat-

tern of velocity vs. depth and a distinctly abrupt increase to locally high values at ~150 mbsf. This depth corresponds to the base of lithologic Subunit IC and at ~155 mbsf to pp4(s). Markedly lower and more uniform velocities are observed from 170 to 250 mbsf by all three techniques. Another sharp velocity increase occurs at 250 mbsf, corresponding to the base of lithologic Subunit IIA and close to the depth of pp5(s) (~246 mbsf) calculated from the checkshot survey. Core recovery was poor below this depth, and log data provide the only complete set of velocities close to the logging TD of Hole 1072B

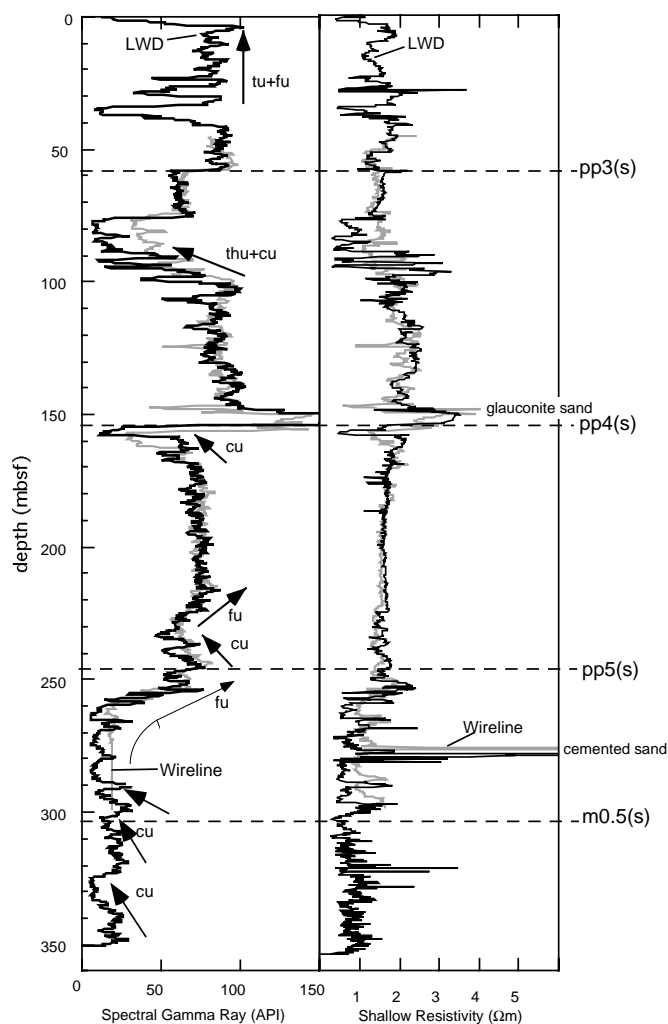


Figure 33. Summary of the gamma-ray (LWD GR, SGR) and resistivity data from wireline (gray line) and LWD (black line) logging runs at Site 1072. Depths of mapped seismic horizons are indicated, as calculated from the Hole 1072B checkshot velocity data. tu = thinning upward; fu = fining upward; th = thickening upward; and cu = coarsening upward.

(~297 mbsf). These data show a very high velocity layer several meters thick at ~278 mbsf that may correspond in part with a sandstone recovered in Section 174A-1072A-50R-1.

Log-Seismic Correlation—Synthetic Seismograms

The amount of downgoing sound energy reflected back to the sea surface and recorded in a seismic profile depends on many factors. Among these are the amplitude and frequency content of the source pulse, impedance contrasts at and beneath the seafloor, bed thickness, and bed geometry. Despite this complexity, comparing a synthetic seismogram to a seismic profile can be instructive in terms of determining exactly what stratal features have generated the observed profile. Synthetic seismograms are useful to the study of the geologic expression of sea-level change because they permit a precise comparison between the age and facies of sediments and the stratal geometry imaged in reflection data. Synthetic seismograms were prepared from the data collected at Site 1072 for such a task.

A one-dimensional synthetic seismogram was constructed for Site 1072 (Fig. 36). There are two steps to this process: converting the wireline data from depth to traveltime, and constructing the synthetic

seismogram. The conversion to two-way traveltime (TWTT) was accomplished using a “sonic-adjusted” checkshot: the TWTT was calculated exactly at locations where checkshot measurements were made at Hole 1072B; between these checkshots, the Hole 1072B sonic log was used to adjust the TWTT.

The synthetic seismogram was constructed in the following manner. The sonic log was edited to account for cycle skipping and a constant density of 2.0 g/cm³ was assumed. This was necessary because washouts and hole rugosity led to poor-quality density logs. Reflection coefficients were then calculated from the change in impedance with depth. Finally, an 80 Hz, minimum phase, Ricker wavelet was convolved with the reflection coefficients. This wavelet was chosen because it was a reasonable approximation of the sea-bottom reflection on the Oc270 seismic data.

Several points are important in examining Figure 36. First, the average amplitude of the seismic data decreases with depth. This contrasts with the synthetic, which has a more even distribution of amplitudes with depth. To make a more accurate comparison, amplitudes of the seismic data should be normalized with depth. Second, a synthetic seismogram was generated only between 0.185 and 0.440 s, which is the interval over which a sonic log was acquired. Third, the log data were acquired from three different holes at Site 1072 (see caption to Fig. 36).

Nonetheless, the synthetic seismogram and the actual seismic data compare well (Fig. 36). At surface pp4(s) (0.304 s at Site 1072), there is a double peak in the seismic data. Comparison with the synthetic seismogram shows that the seismic trough beneath this couplet closely matches the top of a coarsening-upward interval that underlies the pp4(s) surface (see Fig. 33). The section between pp4(s) and pp5(s) is characterized by relatively weak reflections in both the synthetic and the actual seismic data. However, several of those present in the seismic data are not represented in the synthetic. It is possible that some of the observed reflections are multiples; additional shore-based processing of the Oc270 seismic data may help resolve this. Surface pp5(s) corresponds with a weak peak on the seismic data and with a peak in the spectral-gamma log (Fig. 36).

Beneath pp5(s), a thin interval (~1.0 m) of high resistivity, density, and velocity at ~278 mbsf correlates with a cemented glauconitic sandstone (see “Lithostratigraphy” section, this chapter). This corresponds with one of the largest troughs in the seismic data (at 0.43 s). The trough is large because of constructive interference between positive impedance contrast at the top and negative impedance contrast at the base of this high velocity interval. Despite our simplification of assuming a uniform density of 2.0 g/cm³, the resulting synthetic seismogram reproduces this observed trough and brackets positive deflections. This implies that in this zone we are able to detect beds of a few meters in thickness. Finally, the m0.5(s) surface is located ~50 m beneath pp5(s) (at 0.46 s). This surface is located within a thick sandy interval, where a few, small fluctuations are imaged in the LWD GR log (Fig. 29), but beneath the bottom of the synthetic seismogram.

Log-Core and Hole-to-Hole Correlations—Stratigraphic Discontinuities

The preceding discussions of velocity vs. depth patterns and synthetic seismograms underscore the importance of accurate sonic information that only log data can provide. Assigning a seismically identified surface to either the top or the bottom of a moderately thick sand unit, for example, can be difficult. Yet, the alternative interpretations can lead to contrasting implications concerning depositional history. Below, we discuss our preliminary log-core correlations, beginning with a description of the regional stratigraphic discontinuities linked by our log data to the samples recovered at Site 1072.

Surface pp3(s) is placed at 57.6 mbsf in Holes 1072A, 1072B, 1072D, corresponding to an abrupt upward increase in gamma-ray

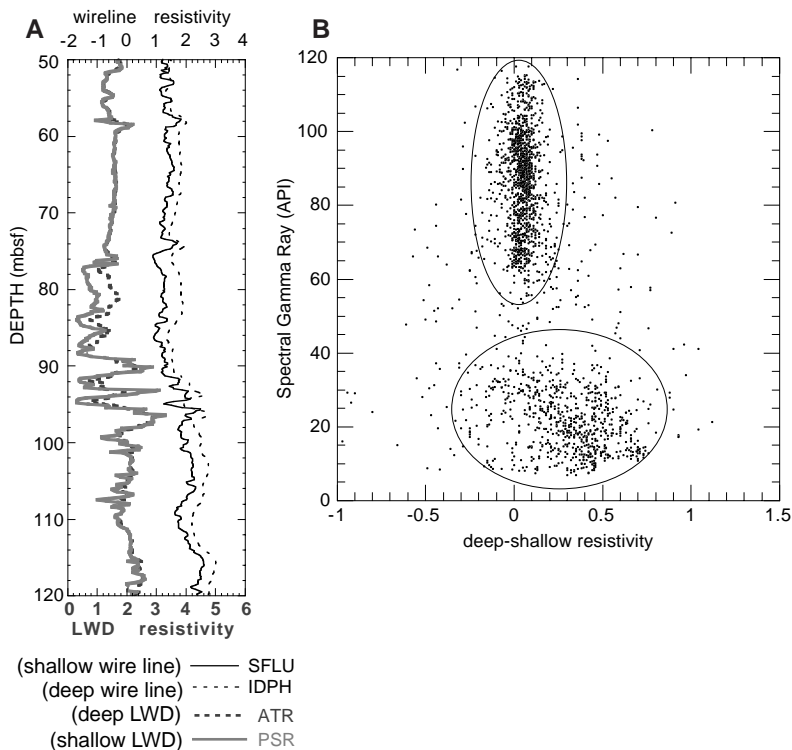


Figure 34. Comparison of shallow (PSR) and deep resistivity (ATR) measurements in wireline and LWD logging. **A.** The separation of the deep and the shallow resistivity logs shows the effect of invasion of more resistive borehole fluid into less resistive formation fluid. Additionally, washouts reduce the shallow resistivity more than the deep resistivity. **B.** The difference between the shallow and deep resistivities plotted vs. gamma ray. The highest separation can be related to low gamma-ray values and therefore to sandy intervals.

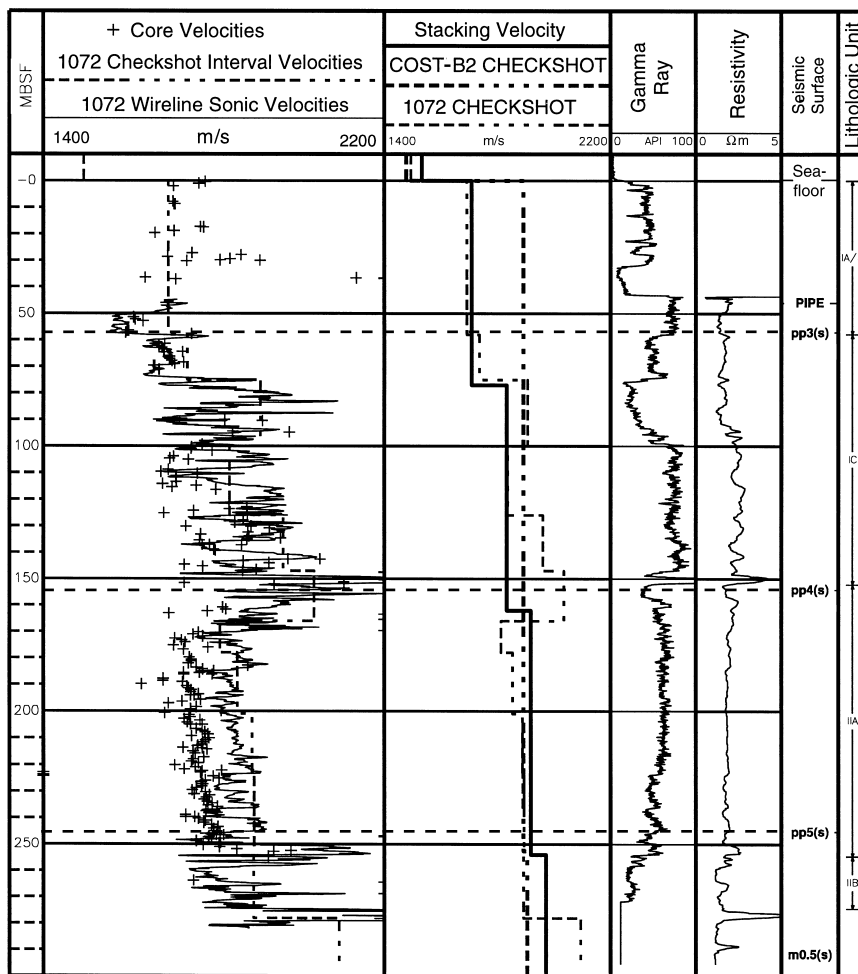


Figure 35. Velocity-depth plot for Site 1072 and nearby velocity measurements. From left to right, columns are as follows: depth in meters below seafloor; three sets of independent velocity data, including ship-board *P*-wave data measured on split cores, wireline sonic velocities, and interval velocities calculated from the checkshot survey at Site 1072; checkshot velocities compared to previously obtained checkshot values at the nearby COST-B2 well, and interval velocities derived from semblance analysis of Oc270 MCS Profile 51 (see “Downhole Logging” section, “Site 1071” chapter, this volume); wireline gamma-ray values; resistivity values; mapped seismic surfaces; and core-based lithologic units. Surfaces pp3(s), pp4(s), and pp5(s) are shown at depths derived by the Site 1072 checkshot survey (see Table 22). Surface m0.5(s) is predicted at 302 mbsf.

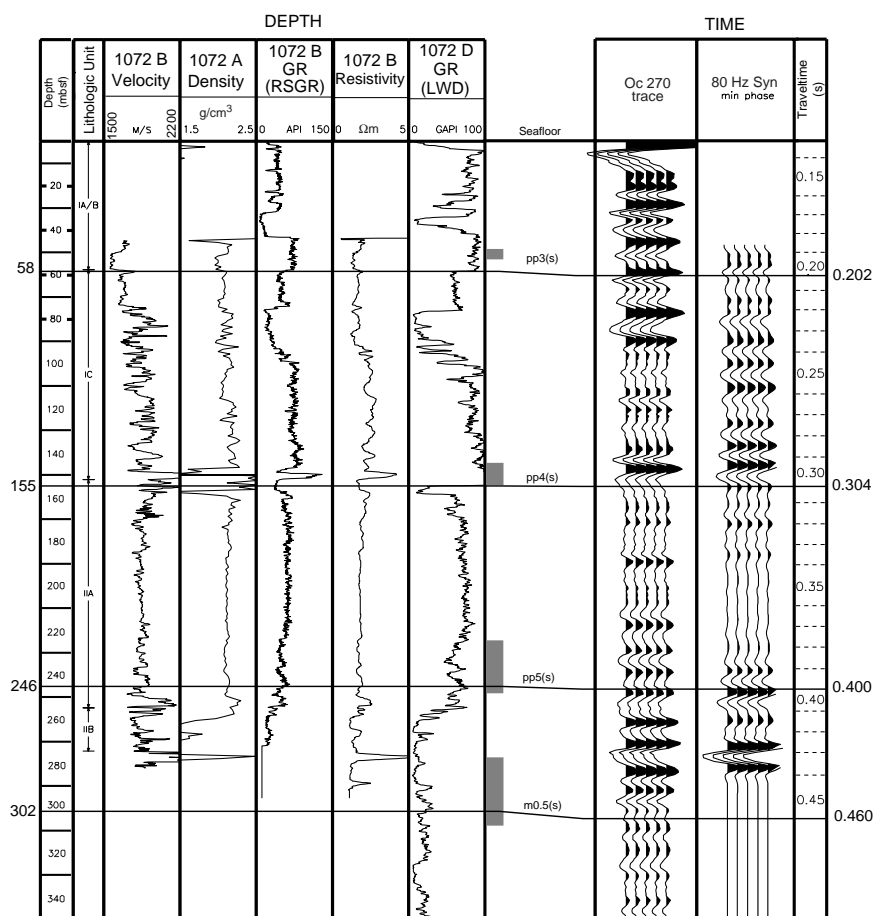


Figure 36. Correlations between depths to features in various boreholes (left) to traveltimes in a seismic profile crossing within a few tens of meters of Hole 1072A (right). Depth below seafloor is in Column 1, and lithologic units are in Column 2. Downhole logging data from Holes 1072A, 1072B, and 1072D are shown in Columns 3–7. The processed seismic trace from Oc270 Profile 908 is in Column 8. Column 9 is a synthetic seismogram based on an 80-Hz, minimum phase, Ricker wavelet convolved with reflection coefficients generated from the sonic log. A constant density of 2.0 g/cm³ was assumed. The sonic log was edited to account for cycle skipping caused by poor borehole conditions. Synthetic seismograms and actual data are plotted with positive to the right and peaks filled black. Finally, the measured traveltimes in seconds below sea level is in Column 10. Lines connecting the depth and time summaries identify four major seismic surfaces that have been tied to the core, log, and seismic records. The vertical gray bars mark calculated depths ($\pm 5\%$) to these reflectors, based on the Oc270 stacking velocities (see Table 22). The horizontal lines that extend to the depth scale at the far left are calculated depths to these surfaces based on checkshot measurements in Hole 1072B. These depths, and the traveltimes to the reflectors, are labeled along the left and right edges of the figure, respectively.

and a decrease in density, velocity and resistivity values (Figs. 29, 37). Recovered cores indicate an abrupt change from clayey silts below to silty clays above. FMS data also show a marked contact, with relatively thick and homogeneous (bioturbated?) beds below and thin-bedded, parallel-laminated sediment above (Fig. 38).

Surface pp4(s) is placed between the glauconite and quartz sands of Cores 174A-1072A-27R and 29R (see “Lithostratigraphy” section, this chapter). The glauconite sand is of variable thickness in the three holes logged at this site (Fig. 39). We interpret this to represent infilling over an irregular pp4(s) surface with ~5 m of local relief. An interval of low gamma-ray and resistivity values lies immediately beneath pp4(s) (Fig. 39). Log excursions e1–e3 represent beds or bed sets dipping to the southeast. We interpret this arrangement to indicate imbrication of a prograding unit beneath the sequence boundary. A similar geometry is observed in the Desert Member (Cretaceous) of the Book Cliffs, Utah (Van Wagoner et al., 1990, their fig. 31). The FMS data suggest the presence of thick (~1 m) beds containing large, resistive clasts, pebbles, and/or shells (Fig. 40) both below and above pp4(s). The FMS image character above the glauconite sand suggests a more disorganized bedding pattern.

Surface pp5(s) is interpreted to represent upward deepening of the environment of deposition. In the logs, we observe a well-defined, stepwise, upward increase in gamma-ray and resistivity values, best expressed in the LWD logs in Hole 1072D (Fig. 41). This marks an abrupt upward increase in clay content during transgression, with possible glauconite contribution to the high gamma-ray values. Core 1072A-48R recovered subangular to rounded quartz and lithic gravel fragments, which we interpret to correspond to a 4-m-thick interval of higher resistivity below pp5(s) centered at 265 mbsf (Fig. 41).

A cemented sandstone was recovered in Section 174A-1072A-50R-1. This interval is of variable thickness and log characteristics in

each of the three holes, but in general shows slightly increased gamma-ray and very high resistivity, density, and velocity values (~278 mbsf in Hole 1072A, Figs. 29, 41). The cemented interval also dips to the southeast (from Hole 1072A to Hole 1072D), consistent with reflection geometry on Oc270 Profile 885 (Fig. 24).

Surface m0.5(s) is tentatively placed at 302 mbsf in Hole 1072D, where there is a change in the character of the resistivity and gamma-ray logs: low frequency variations in resistivity values overlie high frequency variations below m0.5(s), suggesting relatively thin-bedded sediments beneath this surface (Fig. 33). The gamma-ray log suggests that the two coarsening-upward units, ~20 m thick each, lie below m0.5(s); these were not cored.

Log-Core Correlations—Patterns Between Surfaces

Asymmetric trends are tentatively identified in Figure 33 with respect to the stratigraphic discontinuities drilled at this site. Below m0.5(s), coarsening upward is implied by the gamma-ray log over two 20-m-thick intervals. No characteristic pattern can be discerned immediately above m0.5(s), but overall upward fining characterizes the interval beneath pp5(s) from 270 to 252 mbsf. Abrupt coarsening and perhaps thickening upward from silty clays to coarse sands is inferred beneath pp4(s). Upward coarsening and thickening is also inferred from 105 to 75 mbsf in the succession above pp4(s); above 75 mbsf, there is an abrupt contact with clayey silts at an unnamed flooding surface. The clayey silts are overlain by silty clays at another abrupt contact across the pp3(s) surface. The uppermost 40 m display an irregular gamma-ray and resistivity profile. A thick sand-rich unit, with a sharp basal contact above silty clays, extends from 40 to 33 mbsf. Gamma-ray values increase progressively from 40 to 5 mbsf, suggesting interbedded clays and sands in a fining- and thinning-

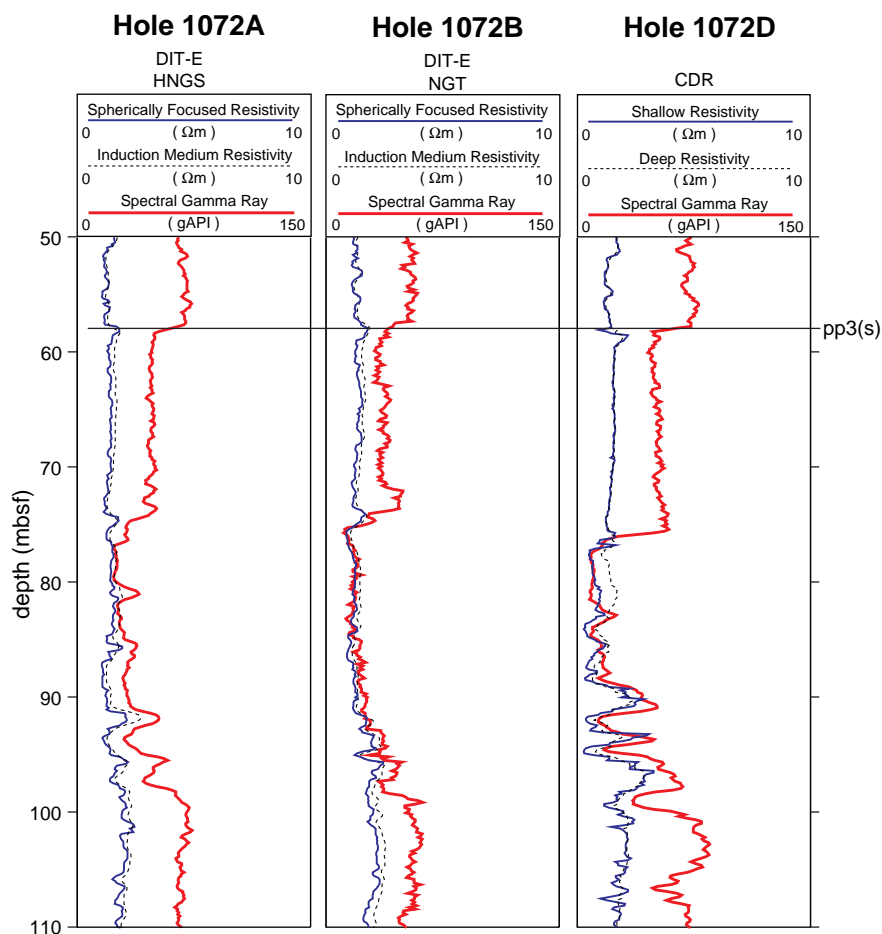


Figure 37. Wireline and LWD logs across the boundary corresponding to surface pp3(s), interpreted at 57.6 mbsf in Holes 1072A, 1072B, and 1072D. This surface is marked by an abrupt upward increase in gamma-ray, and a less pronounced decrease in resistivity values. Different holes are arranged in a north-west–southeast transect, with Hole 1072D located ~40 m to the southeast (downdip) of Hole 1072A (see Fig. 1).

upward pattern. Core recovery in this interval was likely biased to the clay-rich sediments. From 5 mbsf up to the seafloor, gamma-ray and resistivity values decrease abruptly.

FMS images are particularly useful at this site for facies characterization. Examples of the range of features acquired in Hole 1072B are shown in Figures 42 and 43. Figure 42 shows alternations of sandy muds and muddy sands with variable dips that help confirm the visual description of slumps in Core 174A-1072A-17R. Figure 43 displays several conductive and resistive features that are interpreted as burrows, pyrite, siderite concretions, and wood fragments. Detailed comparison with available core data will be necessary to document fully the relationship between electric and sedimentary facies.

Log-Core Correlations—Physical Properties, Lithology, and Mineralogy

In addition to providing control for seismic interpretations as described, log data are very useful for characterizing sediment not recovered by coring. Most intervals of low core recovery at Site 1072 are associated with very low gamma ray, low resistivity, and variable velocity and density. The relationships between these different properties are not straightforward, as illustrated in the crossplots of Figure 44. Velocity and density are positively correlated; in general, gamma ray and velocity increase within more resistive intervals (left two graphs of Fig. 44). Scatter in the resistivity crossplots denotes several exceptions, in particular within the intervals 150–170 and 75–90 mbsf, where velocity increases as resistivity and gamma ray decrease (Fig. 29). These characteristics suggest that very coarse sediments are present within these intervals, and this is supported by the high separation between shallow and deep resistivities (Fig. 34). This interpre-

tation is also corroborated by FMS images in the vicinity of surface pp4(s) that show highly resistive patches within a moderately resistive matrix, suggesting pebbles/gravel within a sand-rich, porous matrix (Fig. 40). Several intervals with very low resistivity, and high deep to shallow separation, are also observed between 250 and 300 mbsf (Fig. 29).

Physical properties measurements on cores are compared with the equivalent downhole logging measurements in Figure 30. Bulk density, gamma ray, sonic velocity, and resistivity all show similar trends to those observed in the in situ measurements. The discrete core measurements of density and velocity are characteristically lower than those observed downhole, most likely as a result of core decompression from in situ pressures. The offset in gamma-ray measurements is due mostly to the different units of measurement. (Core data are recorded in total counts in 30 s, whereas log data are registered in gAPI units, as defined by the University of Houston standard calibration facility.)

Comparing well-log data with recovered cores reveals several general relationships. High gamma ray, low resistivity and low sonic velocity are typically associated with intervals that contain relatively fine-grained (muddy) sediments. However, the gamma-ray log alone does not distinguish sands from clay-rich intervals. For instance, the interval immediately above pp3(s) corresponds to silty clays, whereas the interval above pp4(s) (90–145 mbsf) has gamma-ray values similar to those above pp3(s) but contains instead muddy sands and sandy muds. Apparently, the muddy sand interval above pp4(s) contains a significant amount of mica, which is one of the likely sources of additional radioactivity.

Peaks in natural radioactivity are associated with discrete intervals rich in glauconite immediately above surfaces pp4(s) and

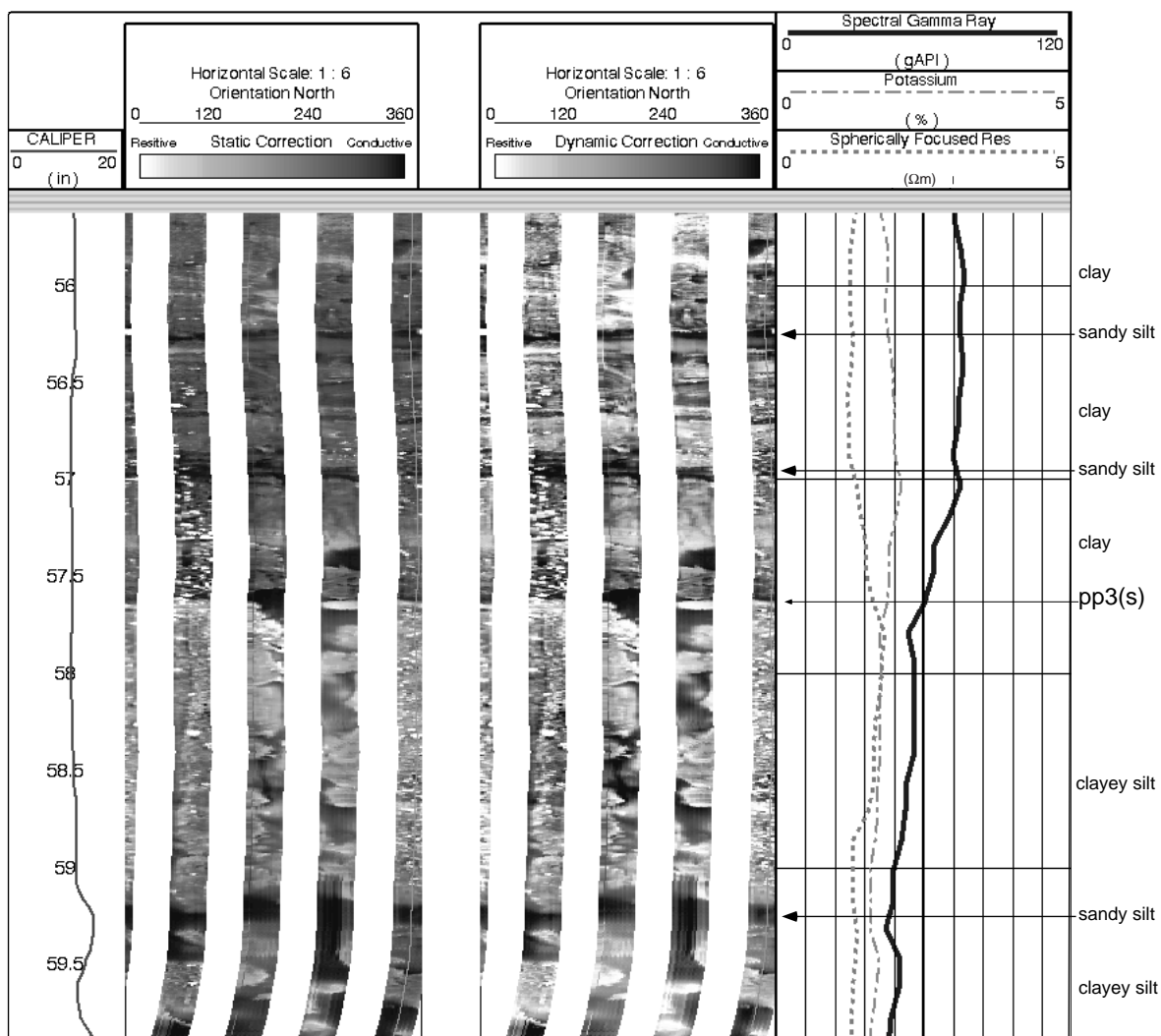


Figure 38. FMS image across the surface correlated with pp3(s) at 57.6 mbsf in Hole 1072B, showing relatively thicker and homogeneous (bioturbated?) beds below and thin-bedded, parallel-laminated sediments above. The image at left is displayed with a range of grayscale of resistivity values that are fixed for the entire logged interval ("static correction"); the image at right allows for a greater range of grayscale to be displayed for normalizing gains for a user-specified depth interval. Both images are from 55.5 to ~60 mbsf.

m0.5(s). These thin intervals (1–2 m thick) also show comparatively high bulk-density, resistivity, sonic velocity, PEF, neutron capture cross section (sigma) and potassium content (Fig. 31).

Examination of the spectral components (K, Th, and U) of the natural radioactivity reveals that the U content is generally very low (<3 ppm), except within the glauconite-rich sand above pp4(s) and within a 10-m interval straddling the pp5(s) surface at ~246 mbsf (Figs. 29, 31). Uranium enrichment often is associated with the presence of organic material; however, TOC values are not particularly high at these depths (see "Organic Geochemistry" section, this chapter). High U levels may be associated with a postdepositional reducing environment related to diagenetic reactions in the vicinity of glauconite-rich layers.

Changes in mineralogy within the drilled section can be evaluated using the Th, K, and PEF measurements from the triple combo run in Hole 1072A. Figure 45 shows the downhole variability in Th/K and PEF. The crossplot in Figure 45 shows that most of the points fall within a region bordered by the kaolinite, illite, and glauconite characteristic values. Mixed-layer clays (e.g., illite/smectite) have PEF and Th/K values intermediate between illite and kaolinite. Some of

the values also show low PEF and Th/K values characteristic of mica (muscovite), whereas several points fall within the range of expected values for pure glauconite. Assuming that the section drilled is a simple mixture of illite and kaolinite, the general uphole trend of decreasing Th/K values and increasing PEF suggests an uphole decrease in the kaolinite/illite value above 250 mbsf. A dramatic decrease in kaolinite/illite ratios from the late Miocene to the Pleistocene on the New Jersey continental slope has previously been attributed to the onset of Northern Hemisphere glaciation and enhanced erosion of the North American hinterland (Deconinck and Vanderaveroet, 1996; Hesselbo, 1996).

Correlation with Hole 1071G

A preliminary correlation between Sites 1071 and 1072 is shown in Figure 46. Using log character and seismic geometry, surface pp3(s) and a prominent flooding surface below it can be tied accurately between the sites. The flooding surface shows a similar log character at both sites, with an abrupt contact between low gamma-ray values below and high values above. Surface pp3(s) was tenta-

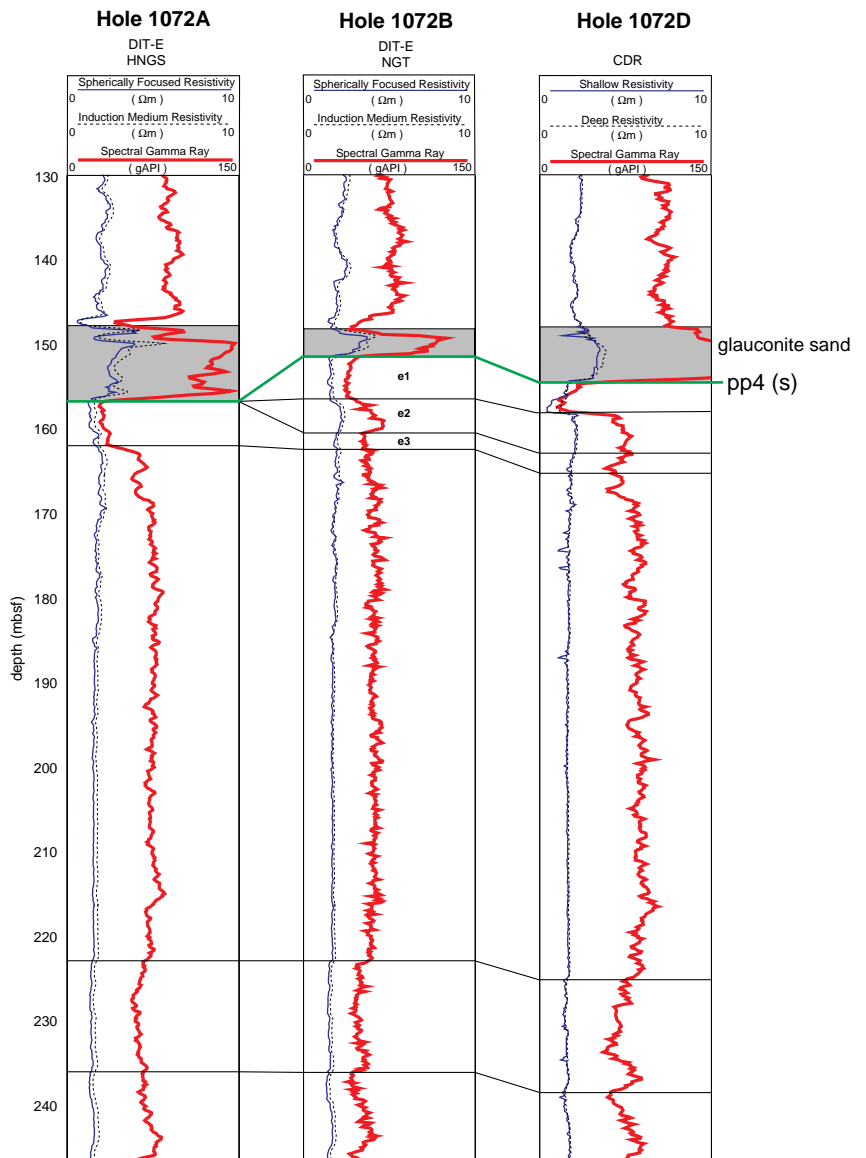


Figure 39. Gamma-ray and resistivity wireline and LWD logs across surface pp4(s) from 130 to 245 mbsf showing different bed characteristics in Holes 1072A, 1072B, and 1072D. The log excursions e1–e3 below pp4(s) correspond on seismic profiles to an interval of imbricated reflections that dip southeast (Fig. 24). The glauconite sand resting on pp4(s) is of variable thickness and has a planar top, suggesting infill over the irregular surface pp4(s). Hole 1072D is located ~40 m to the southeast (down dip) of Hole 1072A (see Fig. 1).

tively defined in Core 174A-1072B-5X (at 57.5 mbsf) and at 57.6 mbsf in the logs (Fig. 38). The position of pp3(s) at Site 1071 is tentatively defined at the low gamma-ray excursion at ~65 mbsf in Hole 1071G, which probably corresponds to the interval of increased sand content seen in Sections 174A-1071B-5X-2 and 174A-1071C-2X-2. The seaward thickening of the interval between pp3(s) and the flooding surface beneath is consistent with the offlap seismic geometry (Fig. 25).

SUMMARY AND CONCLUSIONS

Site 1072 intersected most of the sequences and bounding surfaces observed at Site 1071, with the exception of m1(s). Hole 1072D, the deepest at this site, penetrated >50 m below the level of m0.5(s) in a thick interval of unrecovered sand. The succession at Site 1072 differs from that at Site 1071 primarily in an increase in the proportion of silt/clay to sand at all stratigraphic levels above m0.5(s), and in an increase in the thickness of fine-grained intervals immediately below surfaces pp3(s) and pp4(s). Site 1072 reinforces all of the conclusions tentatively reached at Site 1071. A full suite of downhole logs permits more precise location of pp3(s), pp4(s), and m0.5(s) and corroboration of biostratigraphically determined ages.

The main elements of the succession are as follows. Unit I (Holocene[?] to lower Pliocene [?]; 0–152.13 mbsf in Hole 1072A) consists of sand, silt, and clay that are locally micaceous, glauconitic, fossiliferous, and bioturbated. Unit II (lower Pleistocene[?] to upper Miocene; 152.13–274.38 mbsf in Hole 1072A) is lithologically similar, and contains siderite nodules and cement in places. Sand is poorly represented in recovered samples and is inferred on the basis of downhole wireline logging (Holes 1072A and 1072B) and LWD (Holes 1072C and 1072D).

Surfaces pp3(s), pp4(s), and m0.5(s) are located as follows. Surface pp3(s) is interpreted at 57.6 mbsf on the basis of core observations and downhole logging data. Surface pp3(s) is characterized in core at 57.5 mbsf in Hole 1072A by localized coarsening from burrow-mottled clayey silt to silty clay with thin interbeds of sand and scattered pebbles (Core 174A-1072A-8R-1). An abrupt upward increase in gamma-ray and a decrease in density, velocity, and resistivity values at 57.6 mbsf provides the best estimate of the depth to pp3(s), and is consistent in three holes (Holes 1072A, 1072B, and 1072D). Both logging and core depths are very close to the depth predicted from traveltimes using semblance velocities from Oc270 seismic reflection data and checkshot data at Site 1072 (49–55 and 58 mbsf, respectively). The gamma-ray data indicate that the 15-m interval above pp3(s) is finer grained overall than the section below, as in

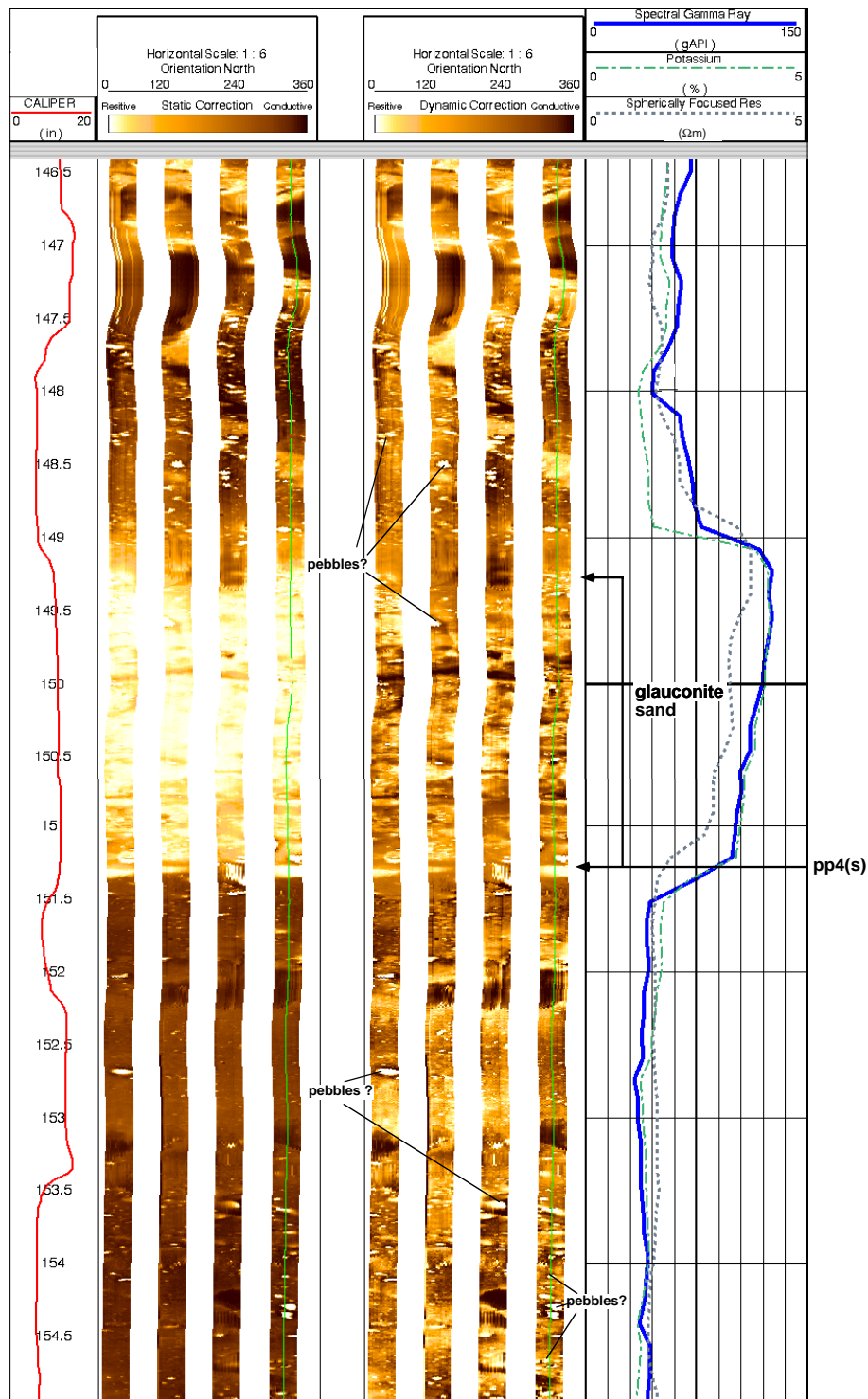


Figure 40. FMS image across the surface correlated with pp4(s) at 151.4 mbsf in Hole 1072B, which suggests thick (~1 m) beds containing large, resistive clasts, pebbles, and/or shells both below and above pp4(s). Image character above the glauconite sand suggests more disorganized bedding. See Figure 38 for explanation of FMS display.

Hole 1071G; this is considered to indicate overall upward deepening across the contact in the preserved sediments. Surface pp4(s) is interpreted in an unsampled interval between 152.1 and 160.3 mbsf (Cores 174A-1072A-27R and 29R), consistent with the depth predicted from traveltimes using Oc270 semblance velocities and check-shot data (141–155 and 155 mbsf, respectively). Sediments above the boundary (Core 174A-1072A-27R) consist of poorly sorted fine- to

coarse-grained glauconite sand. Below the boundary, sediments recovered in Core 174A-1072A-29R are sandy silt with intercalated fine-grained sand. A comparison of spectral gamma-ray (SGR) data allows pp4(s) to be located relatively precisely at a sharp contact between glauconite sand above and several meters of quartz sand below. This contact is at 157 mbsf in Hole 1072A, 151.4 mbsf in Hole 1072B, and 155 mbsf in Hole 1072D; the variation in depth is inter-

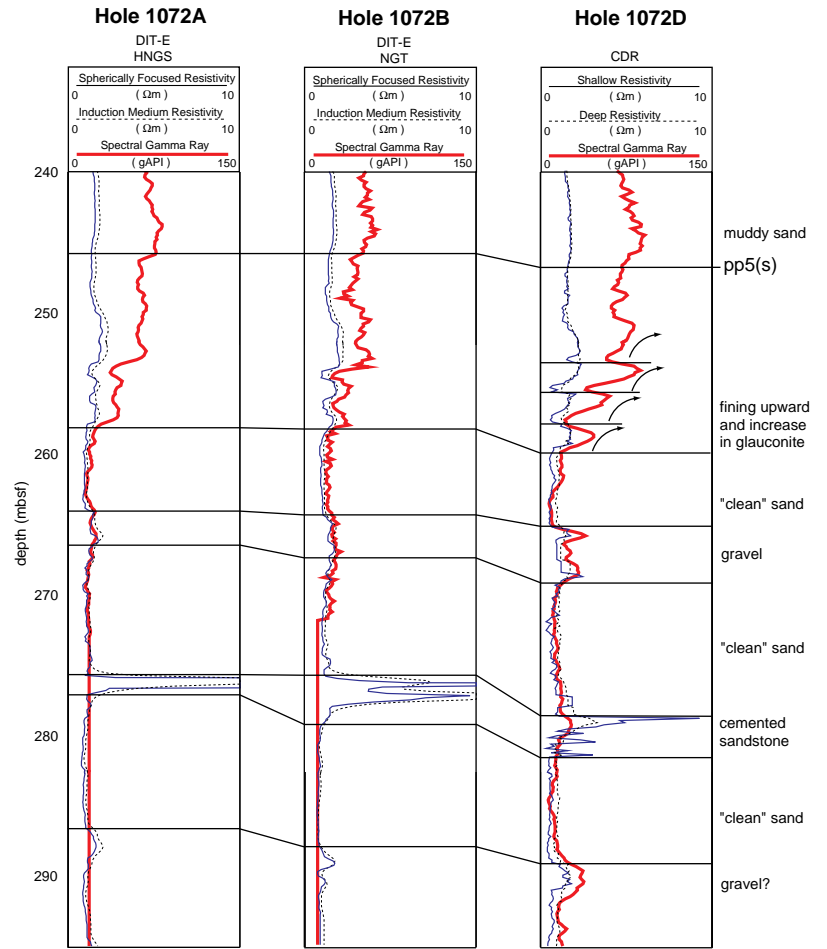


Figure 41. Gamma-ray and resistivity wireline and LWD logs across surface pp5(s) from 240 to 295 mbsf on Holes 1072A, 1072B, and 1072D. All three logs show a prominent peak in resistivity that is correlated with a cemented sandstone in Core 174A-1072A-50R. Gamma-ray and resistivity logs in all three holes suggest increasing clay content and a fining-upward pattern; the surfaces show a gentle southeast dip. Surface pp5(s) is interpreted to be a marine flooding surface (see “Summary and Conclusions” section, this chapter, for further discussion). Hole 1072D is located ~40 m to the southeast (down dip) of Hole 1072A (see Fig. 1).

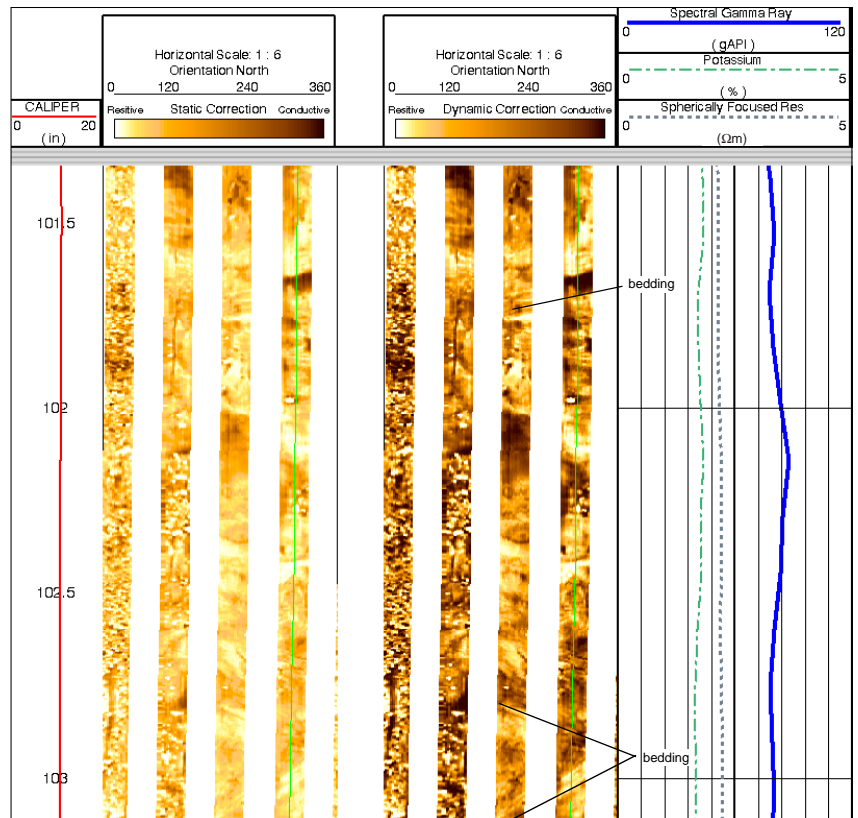


Figure 42. FMS image from ~101 to ~103 mbsf in Hole 1072D showing alternations of sandy muds and muddy sands with variable dips that corroborate the visual report of slumps in Core 174A-1072A-17R. See Figure 38 for explanation of FMS display.

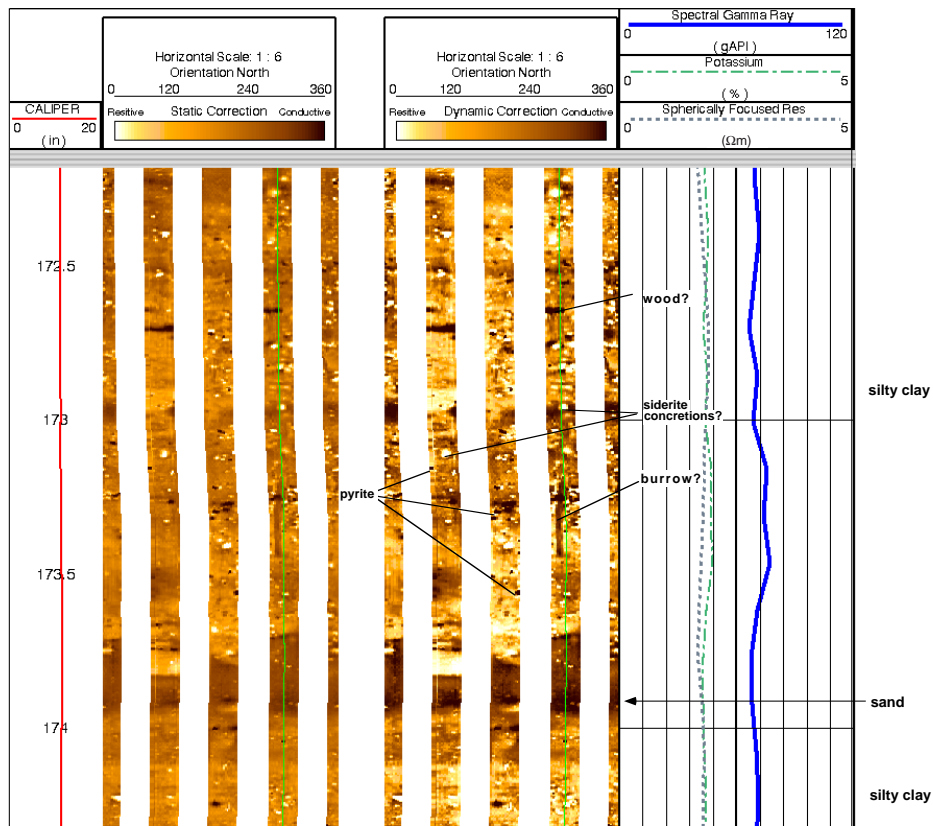


Figure 43. FMS image from 172 to 174.5 mbsf in Hole 1072D showing several conductive and resistive features that are interpreted as burrows, pyrite, siderite concretions, and wood fragments.

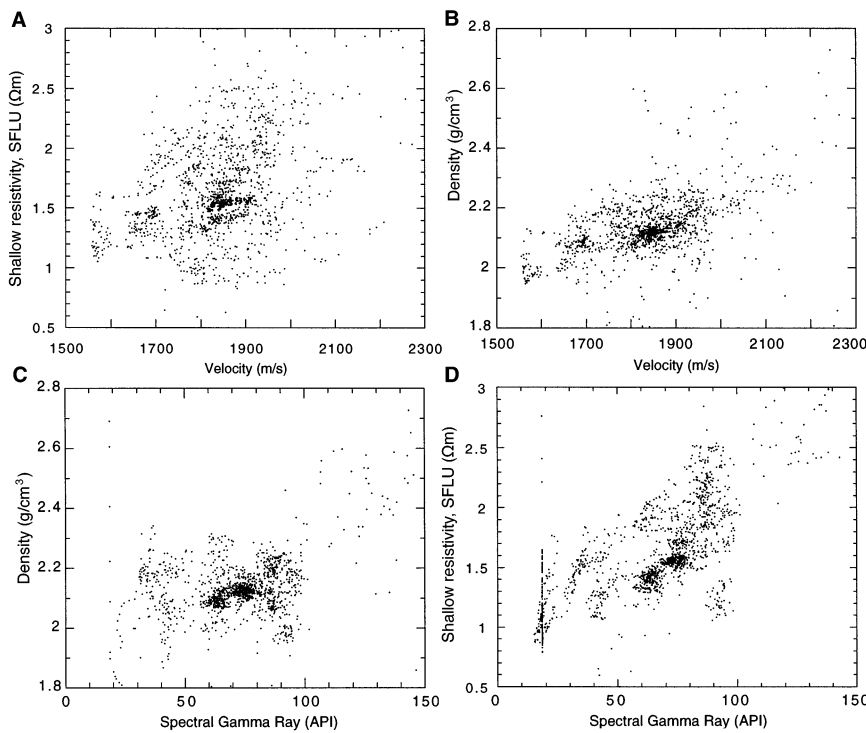


Figure 44. Crossplots of (A) velocity/resistivity, (B) velocity/density, and (C) spectral gamma ray/density that show positive correlations at Site 1072. The positive correlation (D) between spectral gamma ray and shallow resistivity is related to the lithology. In this setting, the unconsolidated sand-rich layers show the lowest resistivity, and the clay-rich layers show the highest resistivity and highest gamma-ray values.

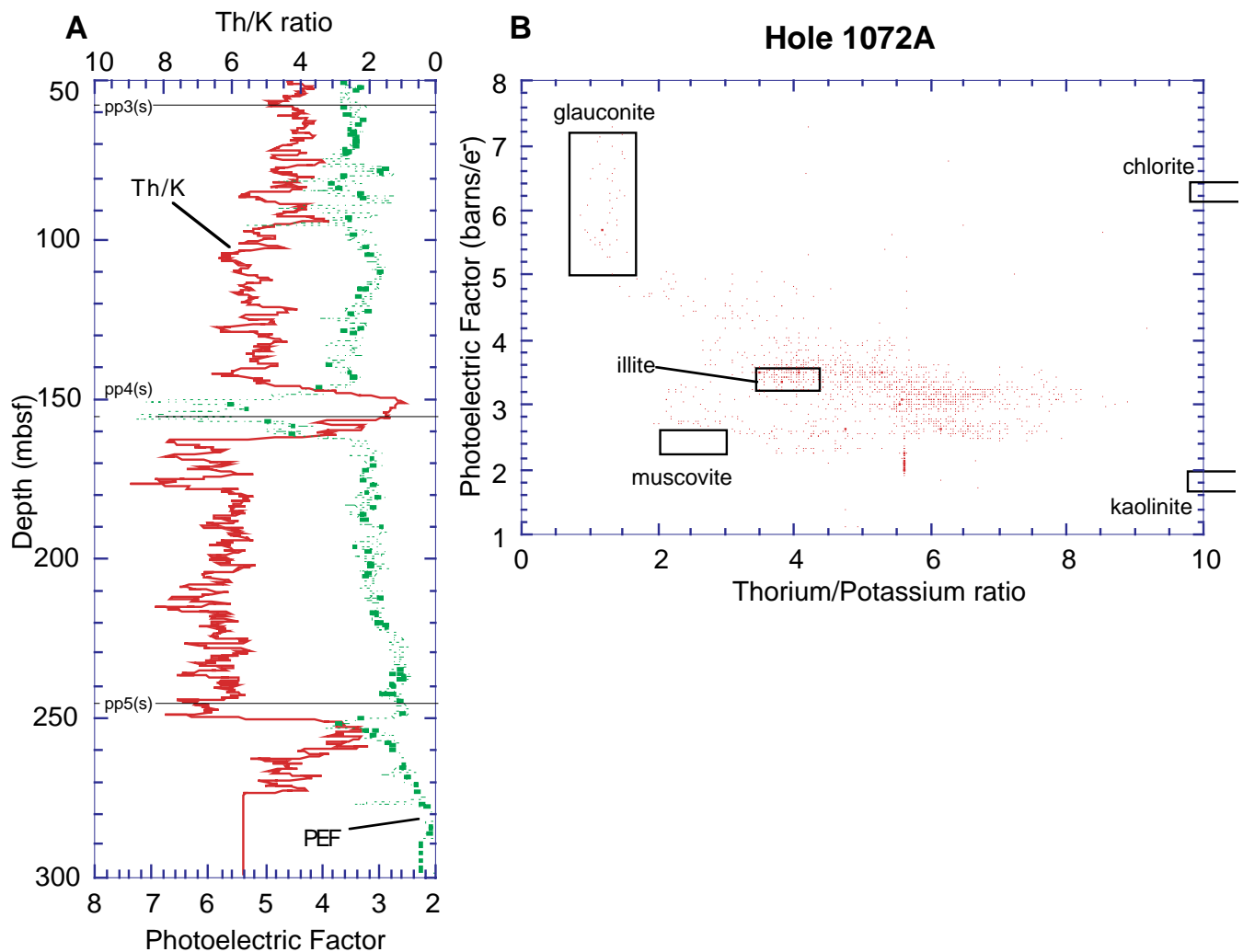


Figure 45. **A.** Th/K value calculated in Hole 1072A shows characteristic trends for distinct depth intervals. **B.** The crossplot of the Th/K value vs. the photoelectric factor (PEF) distinguishes between different types of clay minerals and mica (see text for further discussion).

preted to indicate ~5 m of local erosional relief at the sequence boundary. Surface m0.5(s) is tentatively placed at 302 mbsf in Hole 1072D, a level that is well below the lowest recovered sample (274.38 mbsf; Core 174A-1072A-50R). This is also >30 m deeper than its interpreted depth at Site 1071, but is consistent with depths predicted from seismic reflection and checkshot data at Site 1072 (278–308 and 302 mbsf, respectively). Below the interpreted level of m0.5(s), SGR data indicate at least 50 m of sandy sediment arranged into two coarsening-upward successions. Above this horizon, the gamma-ray signal becomes blockier and resistivity variations are of markedly lower frequency, consistent with aggradationally stacked, thicker bedded sands. In the absence of core information and of any borehole data from deeper levels at Site 1072, uncertainty remains in the precise placement of m0.5(s).

At Site 1072, pp5(s) is predicted at depths of 225–249 and 246 mbsf on the basis of traveltimes using Oc270 semblance velocities and checkshot data, respectively. This corresponds approximately with a stepwise upward increase in gamma-ray and resistivity values at ~252 mbsf and with a transition from poorly recovered glauconitic sand (254.2 mbsf; Core 174A-1072A-47R) to micaceous very fine-grained muddy sand (Core 174A-1072A-46R). In contrast to Site 1071, the transition to consistently finer grained sediments (clay and silt) is stratigraphically higher, at 226.2 mbsf (Core 174A-1072A-42R).

Ages determined for surfaces at Site 1072 are consistent with those obtained at Site 1071. Surface pp3(s) is <0.78 Ma on the basis of nanofossils and the inferred position of the Brunhes/Matuyama magnetopolarity boundary at 62.3 mbsf in Hole 1072A (4.7 m below the interpreted position of pp3[s]). The upper age limit for this surface is 0.25 Ma, if located at 57.79 mbsf (deeper than our preferred interpretation). Surface pp4(s) is dated as 1.4–7.4 Ma and pp5(s) as 5.9–7.4 Ma on the basis of dinocysts. Surface m0.5(s) is poorly constrained as >5.9 Ma.

Downhole logging data at Site 1072 reinforce the interpretation of pp4(s) as a sequence boundary. The surface is both sharp and characterized by local (erosional) relief. As at Site 1071, it is also associated with a marked discontinuity in facies and upward shoaling, from middle neritic (50–100 m) below to inner/upper middle neritic (0–65 m) above (benthic foraminifers). Logging and core data from Site 1072 also confirm the interpretation of pp5(s) as an interval of upward deepening.

Site 1072 corroborates the facies architecture inferred at Site 1071. Downhole logging data for the sequence between m0.5(s) and pp4(s) indicate that it is markedly asymmetrical, dominated by shallow-water transgressive sands in the lower half and deeper water silt/clay in the upper half, with evidence for renewed progradation of sand only in the upper 20 m. Seismic geometry suggests that seaward thinning of the sandy transgressive interval is a result of condensation

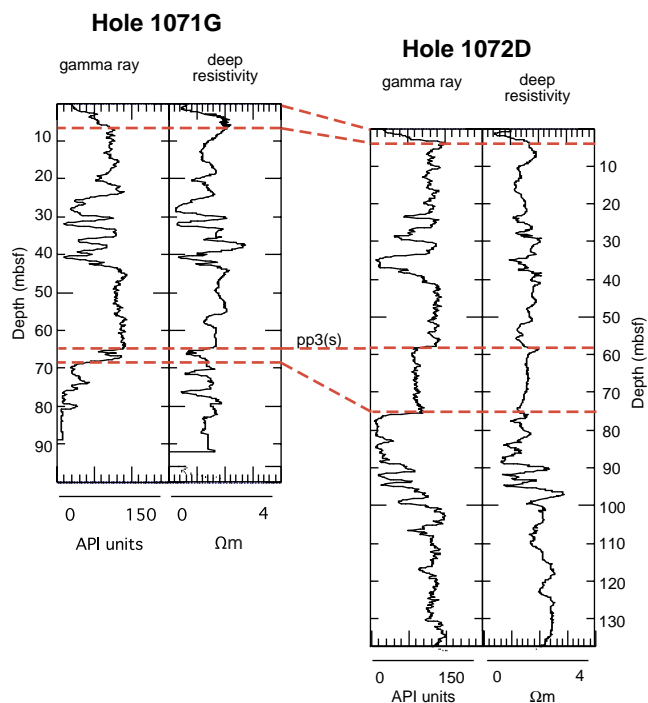


Figure 46. Correlation of the LWD gamma-ray and resistivity logs from Holes 1071G and 1072D. Note that the log displays have been shifted in depth to align pp3(s) and visually emphasize the similarity of log character above this depth.

rather than lateral facies change. Seaward thickening of the progradational upper part of the sequence, combined with the many tens of meters of sand observed beneath m0.5(s) in the vicinity of its rollover/breakpoint, is consistent with marked offlap beneath these sequence boundaries. It appears that in a landward direction, these late Miocene and younger sequences of the New Jersey margin are represented primarily or exclusively by transgressive deposits, an unusual arrangement that is consistent with very marked hiatuses at the sequence boundaries. Downhole logging data at Site 1072 confirm the presence of higher order depositional cyclicity within sequences. Examples are evident in the sequence below pp3(s) and both below and above m0.5(s). Such cyclicity is responsible for much of the reflection character of seismic profiles, but only locally can subtle geometry such as imbrication be resolved.

As at Site 1071, the interstitial water profiles at Site 1072 show the influence of sea-level fluctuations. Chloride concentrations decrease from near seawater values at the seafloor to a minimum at 60 mbsf (469 mM, a 16% decrease). This salinity minimum is less pronounced and ~30 m deeper than the corresponding minimum at Site 1071. The second, deeper salinity minimum observed at Site 1071 (~300 mbsf) was not observed at the base of the sampled interval at Site 1072 (230.5 mbsf).

REFERENCES

- Austin, J.A., Jr., Mountain, G.S., Christie-Blick, N., and Miller, K.G., 1996. Deciphering the sea-level history of the Icehouse: continuation of the New Jersey Transect. *Eos*, 77:F330.
- Berggren, W.A., Kent, D.V., Swisher, C.C., III, and Aubry, M.-P., 1995. A revised Cenozoic geochronology and chronostratigraphy. In Berggren, W.A., Kent, D.V., Aubry, M.-P., and Hardenbol, J. (Eds.), *Geochronology, Time Scales and Global Stratigraphic Correlation*. SEPM (Soc. Sediment. Geol.), 54:129–212.
- Buck, K.F., and Olson, H.C., in press. *Elphidium* faunas of the New Jersey shelf: implications for sea-level fluctuations during late Quaternary glaciation. *J. Foraminiferal Res.*
- Christie-Blick, N., Miller, K.G., Mountain, G.S., Driscoll, N.W., Reynolds, D.J., and Steckler, M.S., 1992. Sequence stratigraphy and sea-level change: examples from the Atlantic margins of the U.S. and Canada. In *The Tectonics, Sedimentation and Palaeoceanography of the North Atlantic Region*. Geol. Soc. London, Mar. Studies Group.
- Deconinck, J.F., and Vanderaverroet, P., 1996. Eocene to Pleistocene clay mineral sedimentation off New Jersey, western North Atlantic (Sites 903 and 905). In Mountain, G.S., Miller, K.G., Blum, P., Poag, C.W., and Twichell, D.C. (Eds.), *Proc. ODP, Sci. Results*, 150: College Station, TX (Ocean Drilling Program), 147–170.
- de Verteuil, L., and Norris, G., 1996. Miocene dinoflagellate stratigraphy and systematics of Maryland and Virginia. *Micropaleontology*, 42 (Suppl.).
- Ellison, R.L., and Nichols, M.N., 1976. Modern and Holocene foraminifera in the Chesapeake Bay region. In Schafer, C.T., and Pelletier, (Eds.), *First International Symposium on Benthonic Foraminifera of Continental Margins*, (Pt. A). Maritime Sediment., Spec. Publ., 1:131–151.
- Fulthorpe, C.S., and Austin, J.A., Jr., 1998. Anatomy of rapid margin progradation: three-dimensional geometries of Miocene clinoforms, New Jersey margin. *AAPG Bull.*, 82:251–273.
- Greenlee, S.M., Devlin, W.J., Miller, K.G., Mountain, G.S., and Flemings, P.B., 1992. Integrated sequence stratigraphy of Neogene deposits, New Jersey continental shelf and slope: comparison with the Exxon model. *Geol. Soc. Am. Bull.*, 104:1403–1411.
- Hesselbo, S.P., 1996. Spectral gamma-ray logs in relation to clay mineralogy and sequence stratigraphy, Cenozoic of the Atlantic margin, offshore New Jersey. In Mountain, G.S., Miller, K.G., Blum, P., Poag, C.W., and Twichell, D.C. (Eds.), *Proc. ODP, Sci. Results*, 150: College Station, TX (Ocean Drilling Program), 411–422.
- Hicks, K.S., Compton, J.S., McCracken, S., and Vecsei, A., 1996. Origin of diagenetic carbonate minerals recovered from the New Jersey continental slope. In Mountain, G.S., Miller, K.G., Blum, P., Poag, C.W., and Twichell, D.C. (Eds.), *Proc. ODP, Sci. Results*, 150: College Station, TX (Ocean Drilling Program), 311–323.
- McCracken, S.R., Compton, J., and Hicks, K., 1996. Sequence-stratigraphic significance of glaucony-rich lithofacies at Site 903. In Mountain, G.S., Miller, K.G., Blum, P., Poag, C.W., and Twichell, D.C. (Eds.), *Proc. ODP, Sci. Results*, 150: College Station, TX (Ocean Drilling Program), 171–187.
- Miller, K., Rufolo, S., Sugarman, P., Pekar, S., Browning, J., and Gwynn, D., 1997. Early to middle Miocene sequences, systems tracts, and benthic foraminiferal biofacies, New Jersey coastal plain. In Miller, K.G., and Snyder, S.W. (Eds.), *Proc. ODP, Sci. Results*, 150X: College Station, TX (Ocean Drilling Program), 169–186.
- Miller, K.G., Mountain, G.S., Blum, P., Gartner, S., Alm Per, G., Aubry, M.-P., Burckle, L.H., Guerin, G., Katz, M.E., Christensen, B.A., Compton, J., Damuth, J.E., Deconinck, J.F., de Verteuil, L., Fulthorpe, C.S., Hesselbo, S.P., Hoppie, B.W., Kotake, N., Lorenzo, J.M., McCracken, S., McHugh, C.M., Quayle, W.C., Saito, Y., Snyder, S.W., ten Kate, W.G., Ubat, M., Van Fossen, M.C., Vecsei, A., Sugarman, P.J., Mullikin, L., Pekar, S., Browning, J.V., Liu, C., Feigenson, M.D., Goss, M., Gwynn, D., Queen, D.G., Powars, D.S., Heibel, T.D., and Bukry, D., 1996. Drilling and dating New Jersey Oligocene-Miocene sequences: ice volume, global sea level, and Exxon records. *Science*, 271:1092–1095.
- Mountain, G.S., Miller, K.G., Blum, P., et al., 1994. *Proc. ODP, Init. Repts.*, 150: College Station, TX (Ocean Drilling Program).
- Mountain, G.S., Miller, K.G., Christie-Blick, N., and Austin, J.A., Jr., 1996. Ages and architecture of Neogene sequences, New Jersey shelf and slope: ODP Legs 150 and 174A. *Eos*, 77:S162.
- Mozley, P.S., and Burns, S.J., 1993. Oxygen and carbon isotopic compositions of marine carbonate concretions: an overview. *J. Sediment. Petrol.*, 63:73–83.
- Odin, G.S., and Matter, A., 1981. Die glauconarium origine. *Sedimentology*, 28:611–643.
- Poag, C.W., Knebel, H.J., and Todd, R., 1980. Distribution of modern benthonic foraminifers on the New Jersey Outer Continental Shelf. *Mar. Micropaleontol.*, 5:43–69.
- Scholle, P.A. (Ed.), 1977. Geological studies on the COST No. B-2 well, U.S. mid-Atlantic outer continental shelf area. *Geol. Surv. Circ. (U.S.)*, 750.
- Shipboard Scientific Party, 1994. Site 903. In Mountain, G.S., Miller, K.G., Blum, P., et al., *Proc. ODP, Init. Repts.*, 150: College Station, TX (Ocean Drilling Program), 129–205.
- Snyder, S.W., Waters, V.J., and Moore, T.L., 1989. Benthic foraminifera and paleoecology of Miocene Pungo River Formation sediments in Onslow Bay, North Carolina continental shelf. In Snyder, S.W. (Ed.), *Micropale-*

- ontology of Miocene Sediments in the Shallow Subsurface of Onlow Bay, North Carolina Continental Shelf*. Spec. Publ. Cushman. Found. Foraminiferal Res., 25:43–96.
- Urbat, M., 1996. Rock-magnetic properties of Pleistocene passive margin sediments: environmental change and diagenesis offshore New Jersey. In Mountain, G.S., Miller, K.G., Blum, P., Poag, C.W., and Twichell, D.C. (Eds.), *Proc. ODP, Sci. Results*, 150: College Station, TX (Ocean Drilling Program), 347–359.
- Van Wagoner, J.C., Mitchum, R.M., Campion, K.M., and Rahmanian, V.D., 1990. *Siliciclastic Sequence Stratigraphy in Well Logs, Cores, and Outcrops: Concepts for High-Resolution Correlation of Time and Facies*. AAPG Methods Explor. Ser., 7.

Ms 174AIR-104

Note: Core-description forms (“barrel sheets”) and core photographs can be found in Section 3, beginning on page 195. Thin-section descriptions, smear-slide data, and shore-based log processing data can be found on CD-ROM (back pocket of this volume). See Table of Contents for material contained on CD-ROM.